11-7-2022

Numerical Simulations and Modeling of Heat and Mass Transport in Membrane-Based Heat Exchangers

Saja Al-rifai
Florida International University, salri003@fiu.edu

FLORIDA INTERNATIONAL UNIVERSITY

Miami, Florida

NUMERICAL SIMULATIONS AND MODELING OF HEAT AND MASS TRANSPORT IN MEMBRANE-BASED HEAT EXCHANGERS

A dissertation submitted in partial fulfillment of

the requirements for the degree of

DOCTOR OF PHILOSOPHY

in

MECHANICAL ENGINEERING

by

Saja H. AL-Rifai

2022

To: Dean John L. Volakis
College of Engineering and Computing

This dissertation, written by Saja Hani Al-Rifai, and entitled Numerical Simulations and Modeling of Heat and Mass Transport in Membrane-Based Heat Exchangers, having been approved in respect to style and intellectual content, is referred to you for judgment.

We have read this dissertation and recommend that it be approved.

Ibrahim Tansel

Bilal El-Zahab

Osama Mohammed

Marc D. Polanka

Yiding Cao, Major Professor

Date of Defense: November 07, 2022

The dissertation of Saja Hani Al-Rifai is approved.

Dean John L. Volakis
College of Engineering and Computing

Andrés G. Gil
Vice President for Research and Economic Development
and Dean of the University Graduate School

Florida International University, 2022

DEDICATION

Dedication of this work is given to my parents, my husband, and my beautiful kids, Yara & Jad. Without their patience, understanding, support, and most of all love, the completion of this work would not have been possible.

ACKNOWLEDGMENT

First and foremost, praises and thanks to the God, the Almighty, for His showers of blessings throughout my research work to complete the research successfully.

I would like to express my deep and sincere gratitude to my research supervisor, Dr. Cheng-Xian Lin who sadly passed away in June 2022. Dr. Lin was kind, understanding and generous in supporting me every step of the way since the first semester in 2018. Dr. Lin not only provided academic advice but also provided me with support, encouragement, and continuous financial support in difficult times.

I hereby would also give my recognition and appreciation to Dr. Yiding Cao, who supervised my research after Dr. Lin passed away. Dr. Cao was my committee member since 2018 he provides wonderful help in my research progress. He helped me in my last semester to reach graduation.

I would like to give a special thanks to Professor Marc D. Polanka, from the Air Force Institute of Technology (AFIT), for his support in a difficult time during my PhD journey, for his advice to improve my research quality, and for the opportunity he gives me to work for three summer semesters in AFIT research.

I would like to thank all of my committee members, Professor Osama Mohammad, Professor Ibrahim Tansel and Dr. Bilal El-Zahab for their time and wonderful assistance in much useful research.

I am also thankful for the support of all the staff at the FIU graduate school and Mechanical & Materials Department in various forms of support, including graduate assistantship and fellowships.

I really appreciate the support and help of all my colleagues, especially during the hard time of COVID-19 pandemic.

To my caring, supportive, loving, Husband, Anas Bataineh: my deepest gratefulness. Your encouragement and inspiration when the times got rough is much appreciated. It was a great comfort and relief to know that you were willing to provide management of our household activities while I completed my work. My heartfelt thanks.

To my lovely kids, Yara & Jad, who were born through the hard time of this journey, who open their eyes on the lap of a student mother. You've lived the PhD journey with me. I love you so much.

I am extremely grateful to my parents for their unconditional love, prayers, caring and sacrifices for educating and preparing me for my future.

Finally, my thanks go to all the people who have supported me to complete the research work directly or indirectly.

ABSTRACT OF THE DISSERTATION

NUMERICAL SIMULATIONS AND MODELING OF HEAT AND MASS TRANSPORT IN MEMBRANE-BASED HEAT EXCHANGERS

by

Saja Hani Mohammad Al-Rifai

Florida International University, 2022

Miami, Florida

Professor Yiding Cao, Major Professor

Transport membrane condenser (TMC) technology employs nanoporous ceramic membrane as a tubular heat-exchanger element to recover water vapor mass and related latent and sensible heat from flue gases. In this study, prior numerical studies and modeling of the TMC performance are expanded and improved. The heat and mass transfer and pressure drop related to the crossflow ceramic nanoporous tubes in the TMC have been studied numerically within wide ranges of tube diameters. The number of rows, Reynolds number, turbulence intensity, membrane properties, flue gases, and cooling water inlet conditions have also been considered. Two condensation models, Fick's diffusion law and the mixed condensation model, were examined and implemented in user-defined functions (UDFs). In addition, the dominant condensation mechanism was investigated. The results showed that the wall condensation mechanism is dominant at the same membrane porosity and water vapor mass fraction.

The numerical results with condensing flue gases were compared to available correlations for single-phase Nusselt numbers and pressure drops in the literature. It was found that, except for some selected conditions, the single-phase correlations were noticeably different

from the TMC numerical results. Therefore, new empirical TMC correlations for heat transfer and pressure drops as a function of condensation rate, number of rows, and the nanoporous membrane geometrical properties were derived. The established correlations for TMC show a good agreement with numerical data for all investigated parameters. With high certainty, they can predict the convective Nusselt number, overall Nusselt number, and friction factor for the TMC.

A multiphase modeling approach using the volume of fluid (VOF), species transport, and Lee phase change models coupled with Darcy's law was proposed for modeling the heat and mass transfer inside the TMC tube bundle. The multiphase model results were closer to the experimental results than the single-phase model in terms of the outlet flue-gas temperature and condensation rate. Based on the observed and monitored flow pattern in the nanoporous ceramic membrane, the multiphase model can predict phase change and water transport on the TMC wall.

TABLE OF CONTENTS

LIST OF TABLES

TABLES PAGE

LIST OF FIGURES

FIGURES PAGE

ABBREVIATIONS AND ACRONYMS

A	Area, m^2
c_p	Heat capacity at constant pressure, J/kg.s
C_v	Correction factor
C_{mf}	Multiphase condensation rate correction factor
d_o	Tube outer diameter, m
D_h	Hydraulic diameter, m
$D_{v,m}$	Diffusion of species v in the mixture m, m^2/s
E	Total energy, J
dt	Time step, s
g	Gravitational body forces, m/s^2
G_ω	The generation of ω
G	Mass velocity $(\rho V_{in,fg})$
h_s	Convection heat transfer coefficient, $W/(m^2.K)$
I	Unit tensor
J_i	Diffusion flux of species i
k	Turbulent kinetic energy, m^2/s^2
L	Length, m
M	Molecular weight, kg/kmol
$\dot{m}$	Mass flow rate, kg/s
n	Number of tubes
N_R	Number of rows
Nu	Nusselt number

Pr	Prandtl number $\left(\frac{\mu c_p}{\lambda}\right)$
P	Pressure, Pa
p_m	Average pressure on both sides of the nanoporous layer
$\dot{q}_v$	The rate of heat source or sink, W/m^3
$Re_{D,max}$	Reynolds number at maximum velocity
r	Pore diameter, m
R	Gas constant, J/kg/mol
RH	Relative humidity
R_i	Net rate of production by chemical reaction of the species
S_i	Rate of creation source term, m
S_D	Diagonal pitch, m
S_T	Transverse pitch, m
S_l	Longitudinal pitch, m
t	Time, s
T	Temperature, K
V	Velocity, m/s
Y_k	The dissipation of k due to turbulence
Y_ω	The dissipation of ω due to turbulence
$\bar{u}$	Reynolds average velocity vector, m/s
u'	Fluctuation of velocity in time, m/s
Y_i	ith species mass fraction
Δp	Static pressure drops of the flue gas through the TMC, Pa

GREEK SYMBOLS

μ	Molecular viscosity, kg/m.s
μ_t	Turbulent viscosity, kg/m.s
ρ	Density, kg/m^3
ω	Specific dissipation rate, 1/s
$\vec{\tau}$	Reynolds stress tensor
λ	Thermal conductivity, W/m.s
$\dot{\varphi}_{cond}$	Mixed condensation rate, kg/hr
$\dot{\varphi}_{WC}$	Wall condensation rate, kg/hr
$\dot{\varphi}_{cap}$	Capillary condensation rate, kg/hr
ε	Porosity
Γ	Tortuosity
θ_b	Bird correction factor

SUBSCRIPTS

cw	Cooling water
e	Exit
eff	Effective
conv	Convective
fg	Flue gas
h	Hydraulic
i	Species
l	Liquid
max	Maximum
min	Minimum

o	Outer
out	Outlet
t	Turbulent
v	Vapor
w	Wall

1. CHAPTER I: INTRODUCTION AND BACKGROUND

1.1. Motivation

Based on the report published by the US Department of Energy, heat loss accounts for over ten quadrillion of Btu of energy each year in the US industry, representing about 30.8% of the total energy used in the US [1]. Most heat losses are in the form of low-grade heat exhaust streams, which are happening in many industrial processes. Low temperature and high-water vapor content coexisting with non-condensable gases represent low-grade heat exhaust streams. Furthermore, most industrial processes and equipment consume a large amount of water that is expelled as containment water to the environment.

For example, gas and coal power generation plants are still the dominant energy sources. A considerable amount of the energy produced becomes waste heat as it is discharged to the environment in the form of flue gas. Besides, large volumes of fresh water are consumed in the power plants, and a significant amount of this water is discharged to the environment as water vapor. It was reported that coal-fired power plants discharge flue gas with 4-13% water vapor, and gas-fired power plants discharge flue gas with 15-20% water vapor [2]. Wasting the water vapor content of the flue gas into the atmosphere with its latent heat decreases the thermal efficiency of power plant units [3]. On the other hand, recovering 40-60% of this water can considerably enhance thermal efficiency.

From another point of view, wastewater vapor and heat emissions have a destructive effect on the environment, such as a greenhouse effect, and there is an increased need to control

the amount of heat and water ejected into the environment. Accordingly, the new environmental guidelines imposed a regulation on the power plants to employ a more efficient way to recover heat and water from the flue gas, as well as a portion of the flue gas pollutants, such as SO_x, CO_2, NO_x, before discharging them to the environment.

Also, energy consumption, water shortage, and pollution are expected to increase tremendously in the upcoming years due to the continuous increase in population growth and the need to generate more power. At the same time, heat processing equipment that expels an enormous amount of heat in the form of waste energy would decrease productivity. The research to find an efficient way to recover heat and water has been a top priority in the last few years.

From another point of view, over the last few decades, the power plants suffered from corrosion problems on the surface of the boiler tail because of the interaction between the flue gas pollutants, such as the sulfate radical, and the water [4, 5]. The flue gas of the power plants contains high water-vapor content at its saturation state at a lowered temperature, which may cause the condensation of the water vapor into contaminated liquid water, resulting in corrosion of the duct wall. . Many possible explanations have been proposed to solve this problem and avoid the high-cost repairs required for the corroded tail boiler flue gas duct. Researchers have suggested elevating the exhaust flue gas temperature to prevent corrosion occurring when the flue gas water vapor is under saturation. However, this solution was not workable due to the significant reduction in the boiler efficiency with an increase in the flue-gas exiting temperature. Later, engineers started recovering the flue gas's water vapor.

Different methods were employed to capture the evaporated water from gaseous streams such as liquid/solid sorption [6], cryogenic separation [7], a condensation heat exchanger (cooling) [8], transport membrane condenser (TMC) [9-17]. Each of these technologies suffers from shortcomings and drawbacks. In the liquid/solid sorption methods, the low quality of recovered water, the adsorbent regeneration, and the high cost are the major drawbacks. Cryogenic separation is considered an economically expensive dehydration process because of the high variation in boiling temperature between the water and gases.

The condenser-based convection heat transfer is used as an alternative solution. This type of condenser suffers from corrosion problems associated with the acid pollutant in the gaseous (waste) stream. As the water vapor cools down, it mixes with other particles and deposits corrosive solids onto heat exchanger surfaces. Different designs and models of the condenser-based heat exchanger were proposed to maximize the heat transfer efficiency from the flue gas of the power plant. These models include different condenser configurations such as staggered [18], inline [19], and changing the inclination angle of the condenser [20, 21]. Other types of condenser heat exchangers, such as flat plate [22], finned tube [23], shell and tubes [24, 25], tube-to-tube heat exchangers [26], and mechanically driven heat exchangers [27], were also considered. Despite the improvement in the heat-transfer performance of the previous heat exchanger designs, the condensation heat-transfer performance was little improved. Consequently, researchers have suggested using different heat exchanger materials, such as porous material, to enhance condensation heat transfer.

In recent years, the Gas Technology Institute (GTI) [28-30] introduced an innovative technology based on the porous membrane material as a tube wall of the heat exchanger, named the Transport Membrane Condenser (TMC). They replaced the stainless-steel heat exchanger with nanoporous ceramic membrane tubes. TMC-based heat exchangers can reduce the water consumption of power plants by recovering the water vapor and its latent heat from the flue gas before discharging it to the environment. This innovative technology used a ceramic porous membrane as tube walls. Compared to the conventional heat exchanger, TMC has a higher convection Nusselt number, about 50–80%, and a higher condensation rate, about 60–80%. These results are according to the experimental results conducted by Bao et al. [16]. Also, TMC can transport the condensate to the cooling water, which solves the problem of the condensate film that harms the conventional heat exchanger.

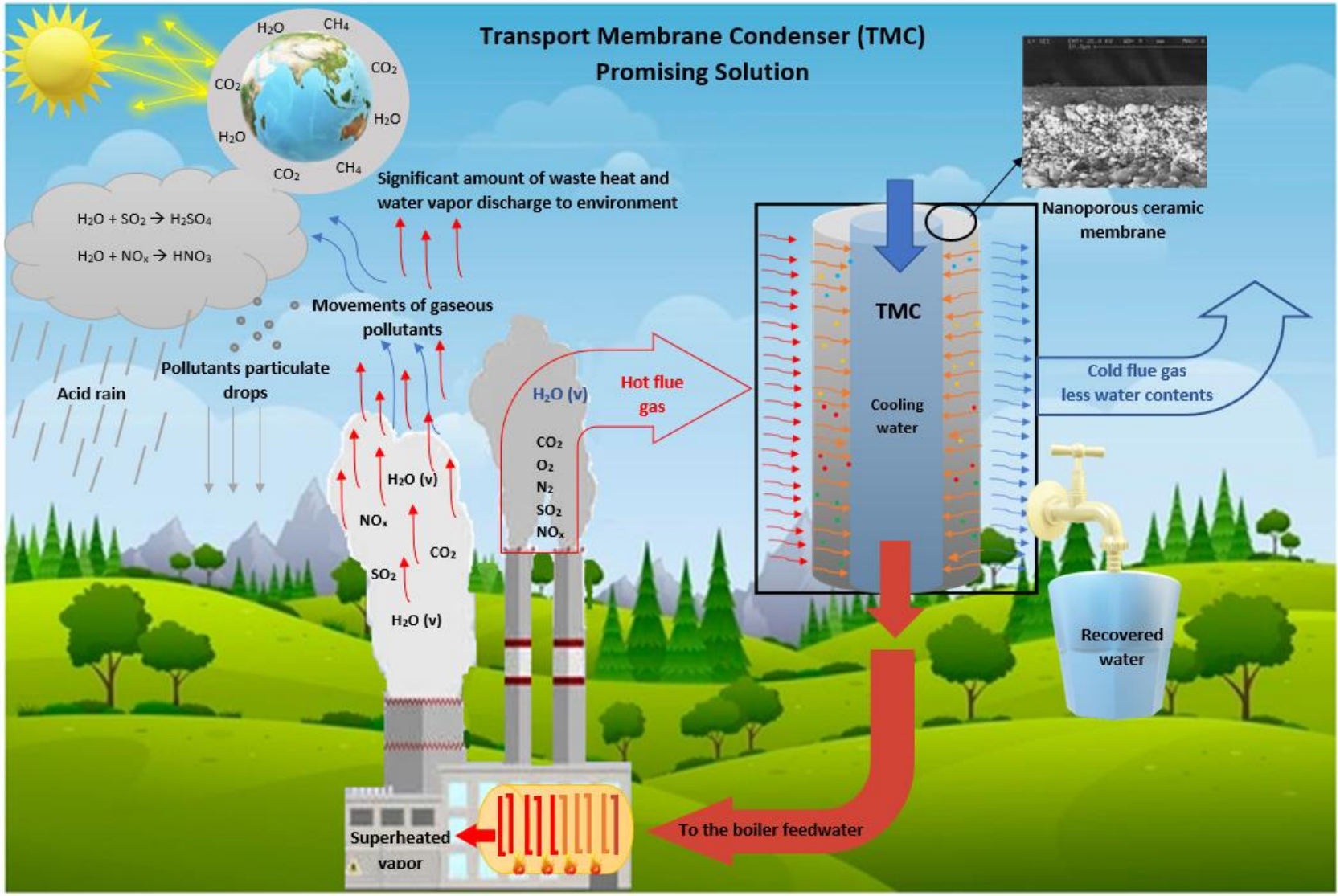

Figure 1. Visual Presentation of Transport Membrane Condenser Principal Operation.

1.2. Background In Transport Membrane Condenser

The transport membrane condenser (TMC) is a promising technology that can recover both latent and sensible heat, besides recovering water vapor in the form of usable water, which reduces energy consumption. TMC technology was first used, in 2011, in the heat and water recovery from the waste flue gas of power plants [28-30]. The technology is based on using nanoporous ceramic membrane materials as the tube wall of the heat exchanger. The membrane recovers the water vapor selectively from the flue gas. The hydrophobic characteristics of the nanoporous membrane hold the condensate water from the flue gas.

This characteristic can distinguish the water molecules from the other molecules present in the flue gas. Figure 1 is a visual representation of applying the TMC technology in recovering the water and heat from the exhaust stream of the power plant.

1.2.1. Membrane separation technology

Membrane technology is characterized by its low price and high separation ratio for both gases and liquids. Two common membranes are categorized in the industrial sector based on their applications in terms of porous and nonporous materials. The pore size of the porous membrane ranges from sub-micron to nano-micron. This type of membrane is based on the membrane surface characteristics and pore size. The separation process involves a combination of different separation mechanisms such as diffusivity, molecular sieving, and surface effects [31, 32]. The pore size may reach 50 nm for gas separation applications based on the gas molecule size. Separation of water vapor from flue gas requires a membrane with a pore size of 6 to 9 nanometers, and it has the highest separation rate under

the capillary condensation phenomena [29]. The separation of water vapor improved considerably when the condensed water completely blocked the nanopores on the outer surface porous membrane and prevented the non-condensable gases from being transported to the other side [31, 32].

The diffusivity and solubility are the dominant characteristics mechanisms in the non-porous membrane [33]. Although the separation ratio in this membrane type is generally high, the transport flux is still considered low [33-35].

The membrane separation technology includes the organic fiber membranes and the ceramic (inorganic) membrane, which selectively separates the water vapor from the flue gas and prohibits other non-condensable gases from being transported with the water vapor. Compared to the ceramic membrane, the organic fiber membrane has the disadvantage of its elevated cost and lower mechanical properties.

The ceramic inorganic membrane is the most popular membrane condenser because of its high thermal conductivity compared to the organic polymer membrane type and is also considered thermally stable with good mechanical strength and corrosion resistance. The thermal conductivity of the ceramic and polymer membrane material varies between 1.4-21.84 W/m.K and 0.1-0.5 W/m.K, respectively, as reported by [36, 37].

Nanoporous ceramic membrane

Figure 2 [29] is a schematic diagram of a nanoporous ceramic membrane of a tubular cross-section with each layer thickness/pore size being shown. The tube wall consists of a nanoporous ceramic membrane that is responsible for transporting the water vapor from the flue gas side to the waterside. The pores block the other non-condensable gases from being transported to the other side as they are filled with condensing water vapor. The recovered water is carried away with cooling water as fresh water. The cooling water becomes warmer as it flows from its inlet to the outlet as a result of absorbing latent heat due to condensation and sensible heat transfer under temperature differences. In comparison, the flue gas temperature and moisture content will reduce as it flows from the inlet to the outlet. A small vacuum is maintained on the water side of the TMC heat exchangers to prevent the backflow of water from the inside of the TMC tubes to the outside.

Based on the size of the pores, the nanoporous ceramic membrane structures are divided into three layers, a selective layer, an intermediate layer, and a substrate. The particular selective layer is at the nanoscale, and the substrate layer is at the microscale. The water vapor from the flue gas releases the latent heat due to the condensation at the surface of the selective layer. The condensate transports to the water flow through the intermediate and substrate layers. The multi-layer structure of the porous material allows the condensed water at the tube's outer layer to move toward the inner layer of the tubes and join the cooling water flow stream. The membrane condensers allow the condensed water to permeate through the membrane sideways with heat transfer.

Based on the location of the selective layer, two different kinds of membrane structures have been developed in the literature, the outer and inner side membrane structures. In the outer side coating, the selective layer is located at the outer side, while in the internal side coating, the particular layer is located at the innermost side, as shown in Figure (3), [2, 38].

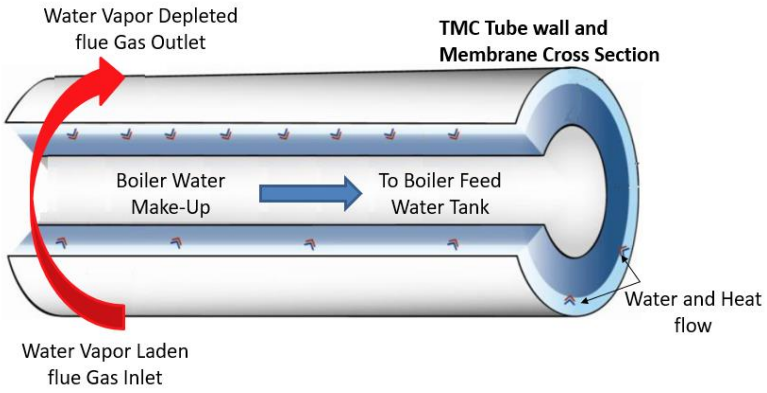

(a) Flow dynamic of condensate water through the TMC single tube.

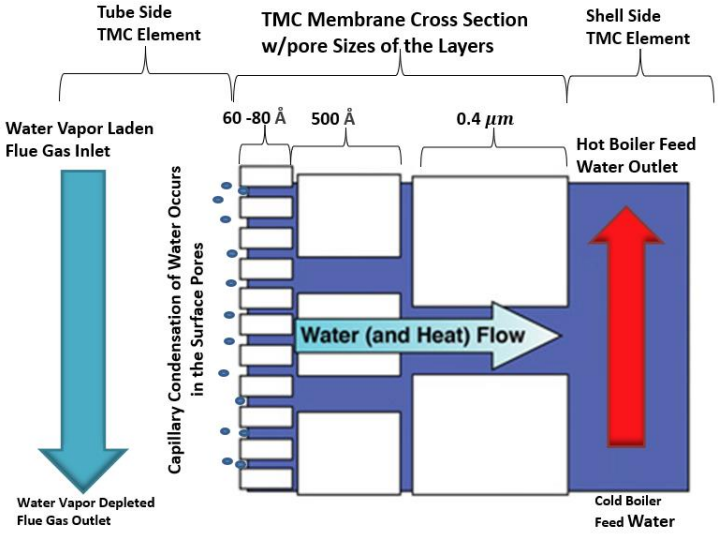

(b) schematic diagram of a nanoporous ceramic tube cross section.

Figure 2. Transport Membrane Condenser Working Mechanism [29].

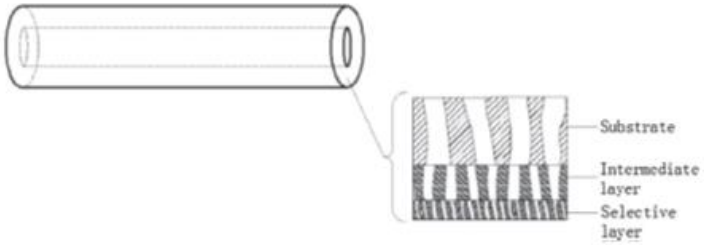

(a) Outer side coating membrane

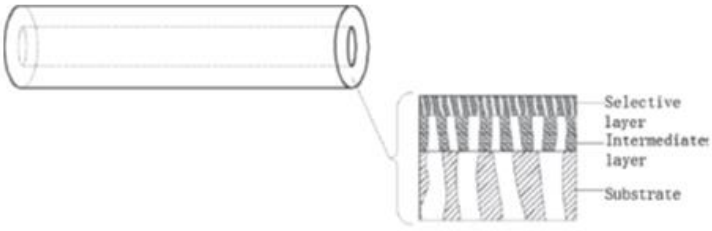

(b) Inner side coating membrane

Figure 3. Nanoporous Ceramic Membrane Structure for a Single Tube [2].

The main component of the nanoporous ceramic membrane is the α alumina nanoparticle (α-Al2O3) substrate layer. The existence of Al2O3 nanoparticles in the tube wall enhances the thermal conductivity of the membrane tube [39]. The water vapor from the flue gas condenses at the outer surface of the outer-side membrane structure, which blocked the non-condensable gases from passing through the membranes. The porous structure and multi-layer, as shown in Figure 4, help the condensed water on the tube's outer layer move toward the tube's inner layer and join the cooling water flow stream.

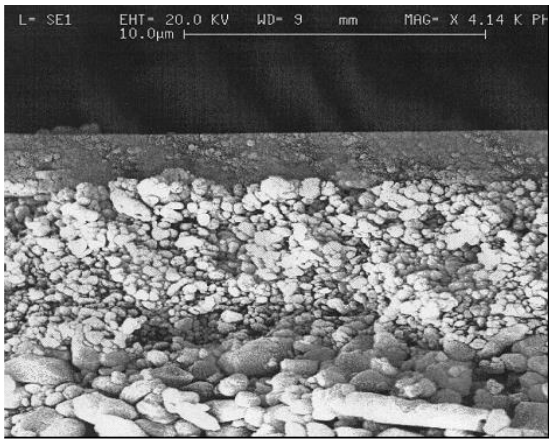

Figure 4. Photomicrograph of TMC Nanoporous Ceramic Membrane Cross-Section [40].

Hollow fiber membrane

The separation process of the hollow fiber membrane, as shown in Figure 5, is based on the membrane selectivity to different components and the potential difference on both sides of the membrane. The driving force of mass transfer is the pressure difference between the external and internal surfaces. The membrane has good selectivity, which allows only the water to pass while the other gas molecules cannot pass through it.

The hollow fiber membrane comprises three layers: the coating layer, the connecting layer, and the support layer. The coating and connecting layers include both compact structures and defective porous parts. The channel size in the supporting layer is larger than in the first two layers, so the viscous flow has a significant effect, and the viscous flow velocity and diffusion velocity exist simultaneously. The tortuous impact on the support layer

increases the pressure difference, which increases the fluid flow rate. This dominates the mass transfer and reduces the support layer selectivity [41].

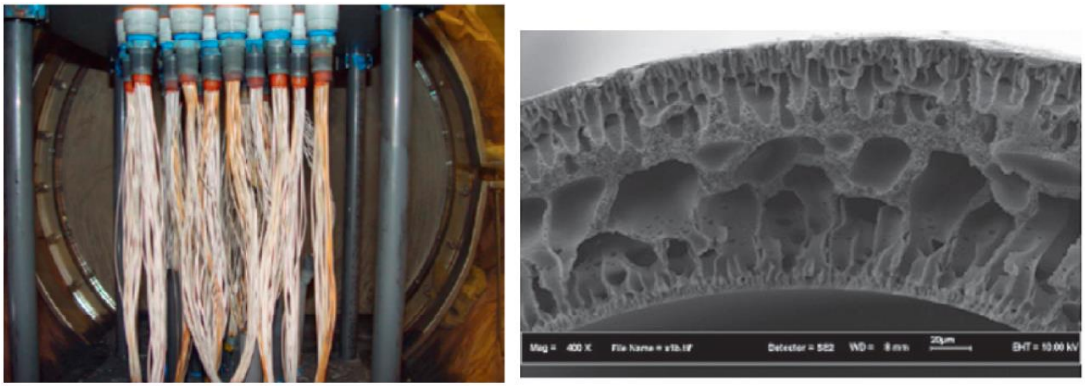

(a) Hollow fiber membrane heat exchanger. (b)SEM images.

Figure 5. Hollow Fiber Membrane [41, 42].

Zhang et al. [41] studied three different membrane materials: polysulfone, cellulose acetate, and polyimide and they found that the membrane material significantly impacting the water vapor flux. Significantly, the coating material and the polyimide material provided higher pure water percentages and lower water flux at different pressure differences compared to other material types. The membrane porosity substantially affects the water vapor transport through the membrane. As the porosity increases, the water vapor transport increases. However, increasing the porosity reduces the membrane's performance and mechanical properties, affecting the membrane service life.

1.2.2. TMC applications

The nanoporous ceramic membrane is a thermally stable membrane with good mechanical strength and corrosion resistance. Transport membrane condenser (TMC) based on using

the nanoporous ceramic membrane can retain heat and fresh water from the gaseous (waste) stream. It was proved that it can find applications in different areas such as flue gas from the power plants [28-30], the waste stream of biogas, and the plume of cooling towers [43, 44]. The membrane condenser can also be used for pre- treatment of the gaseous (waste) stream by retaining a fraction of pollutants. CO_2, with condensed water. Also, suppose the waste stream is needed to regain a specified species. In that case, the reduced amount of water content in the flue gas could increase the performance of the separation unit, such as capturing CO_2 from the flue gas or biogas for biomethane production, see Figure 6 [43, 44]. For example, membrane technology can be used for CO_2 separation from the exhaust gases of the power plant to meet the regulations and restrictions on CO_2 emissions. The membrane technology can capture 90% of CO_2, which is limited by increasing electricity costs of less than 35% [43].

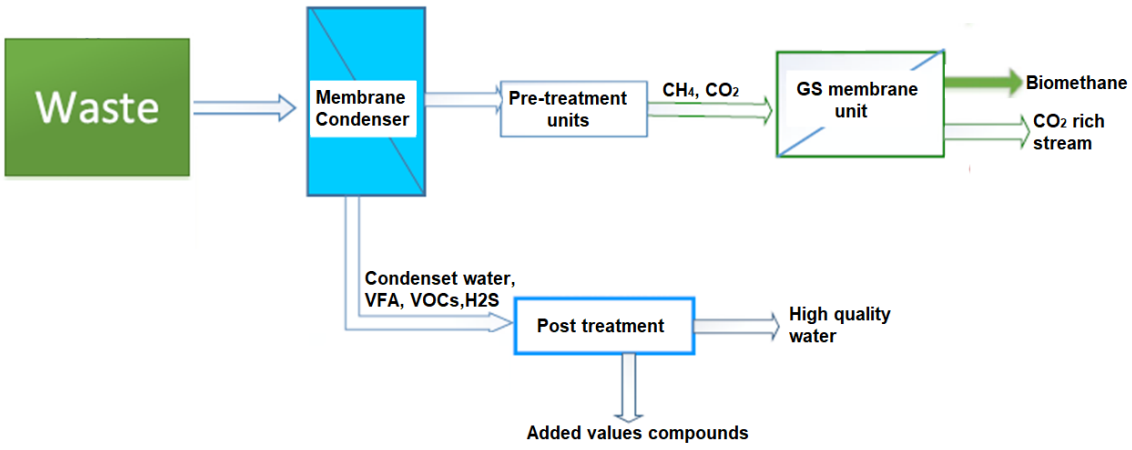

Figure 6: Application of TMC with the Biogas Treatment [43].

The nanoporous ceramic membrane also has been used experimentally to separate the CO_2 [45, 46], SO2 [47-49], and water vapor [16, 49-52] from the flue gas of the coal and gas power plants. Figure 7 represents the water flux and SO_2 flux through the Hyflux20 membrane as a water vapor flow rate function, where the results were taken from the Dehydration experiment test apparatus [47].

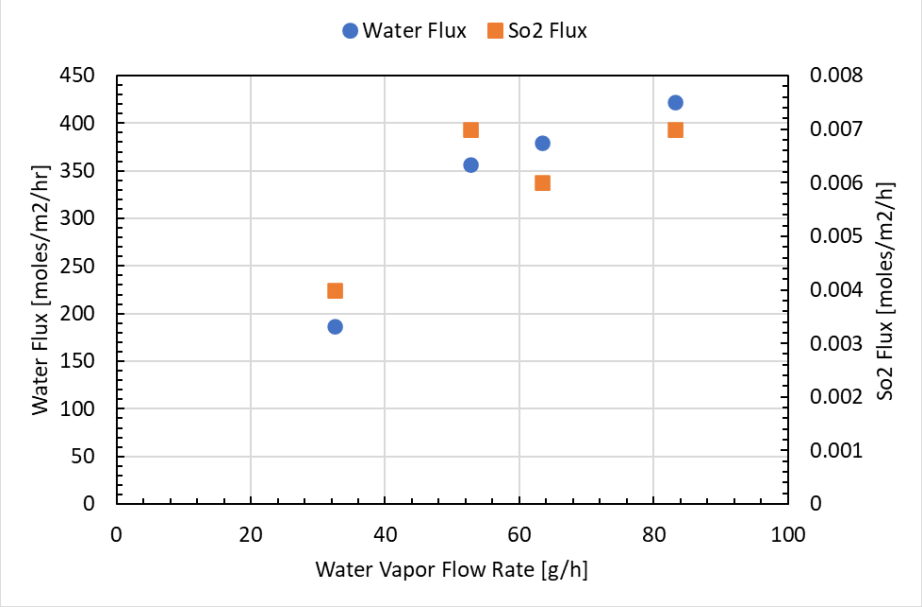

Figure 7. Variation of the Water and SO_2 Flux Through Hyflux20 Membrane as with the Water Vapor Flow Rate, α is the Selectivity [47].

1.3. Experimental Work on TMC

A considerable number of reported experimental works have been performed to extract heat and water from the flue gas using TMC based heat exchanger. In the reported experimental work [28-30], it was shown that the energy efficiency of the boiler-based power plant increased above 5% with 40% water recovered from the flue gas. They

confirmed that water transport through the nanoporous (6 nm) membrane was dominated by capillary condensation. Their results explain that water transport through the nanoporous ceramic membrane is low in the Knudsen diffusion mode. In contrast, capillary condensation could transport the water much more efficiently when the desired flue gas conditions are met.

A group of researchers, references [49-52], conducted a series of experimental work on the lab scale and pilot scale TMC with a 1μm pore-sized ceramic membrane to recover heat and water from the coal-fired power plant. They assessed nanoporous ceramic tube arrays arranged in staggered configuration with different tube spacing and nanoporous ceramic shell and tube. Their research investigated the effect of the longitudinal spacings, ranging from 3 to 8 cm, and the effect of flue gas inlet temperature as well as the inlet cooling water flux and temperature. They also analyzed the permeability of the ceramic membrane for SO_2 during the water recovery process from the flue gas. They concluded that the membrane module with 8 cm longitudinal spacings could achieve a maximum water flux of 22.23 kg/m^2h and a maximum total heat transfer coefficient of 1068.2 W/m^2K.

Chen et al. [53] studied the performance of the TMC under different operating conditions. Their results showed that the water recovery performance could be enhanced by reducing the flue gas flow rate or increasing the cooling water flow rate. Also, an increase in the flue gas inlet temperature can improve heat and mass transfer through the nanoporous membrane. However, the pressure difference between the inner and outer sides of the

membrane does not affect the efficiency of the heat and mass transfer through the membrane.

Bao et al. [16] experimentally compared the heat transfer from the flue gas between the permeable membrane tube bundles (TMC) and the impermeable stainless steel tube bundles. Their results showed sensible and latent heat transfer, and convection and condensation rates were significantly enhanced by using permeable tube bundles. Also, the overall Nusselt numbers of the permeable tube bundles were 50% higher than the impermeable tube bundle, the convection–condensation Nusselt numbers for the porous membrane tube bundle were 0.5–4 times more than the tubes with convection only, and the condensation rate was increased by 60-80% for the porous membrane tube bundle.

In the experimental work of Gao et al. [52], they found that the coal type and power plant load greatly influenced the TMC recovery efficiency. They used the experimental results to measure the linear correlation between the TMC recovery efficiency and operating parameters. The calculated correlation coefficients showed that the water recovery efficiency was affected by changes in the cooling water temperature. Changing the flue gas temperature has had no direct effect on the shift in TMC recovery efficiency. However, the efficiencies change was related to the difference in the water vapor content in the flue gas simultaneously with the change in water dew point temperature.

1.4. Numerical Modeling of TMC

Heat and water recovery using a nanoporous ceramic membrane is a complex process. Water vapor in the flue gas can permeate through the membrane to mix with the cooling

water and then flow out. The heat transfer between the flue gas and the cooling water comprises two parts: the sensible heat from convection and the latent heat of the water vapor from condensation. Numerical simulation of the heat and mass transfer through the tube bundles in TMC is considered a challenging task due to the complex geometry and phase change processes.

Several papers in the literature investigated the performance of TMC numerically using the single-phase model. Lin et al. [17] used the two-step chemical reaction model to calculate the condensation rate at the outer surface of the TMC staggered tube bundle. Xiao et al. [38] calculate the mass transfer through the ceramic membrane by using the lumped parameter model. They considered the concentration gradient effect to measure water vapor diffusion from the flue gas side.

Soleimanikutanaei et al. [10, 11] developed the mixed condensation model based on the weighted linear addition of the solid wall-based condensation model and the capillary condensation model. They assumed that the water vapor in the flue gas stream continuously condenses in membranes and completely blocks the membrane pores. In contrast, the other non-condensable gas components cannot pass. They used the species transport (single-phase model) available on Ansys/Fluent. In the mixed condensation model, they first hypothesized wall condensation. They combined the conventional condensation model on a solid wall surface with the capillary model to calculate the condensation rate.

In another work, Soleimanikutanaei et al. [12-14] evaluated the condensation of the TMC tube bundle by using Fick's diffusion law. They coupled the species transport model (single-phase model) in Ansys/Fluent with the wall-condensation-based Fick's diffusion

law written in the UDFs to model the heat and mass transfer in the TMC tube. They used the correction factor to adjust the condensation rate based on the available experimental data. Their numerical works [10-14] performed multiple numerical studies to investigate the heat and mass transfer characteristics inside the transport membrane condenser under different operating conditions and tube spacings. They found that increasing the inlet water vapor mass fraction for different dimensionless space between the tubes increase the volumetric heat transfer density and the condensation rate, which cause an increase in the overall sensible and latent heat transfer rate between the cooling water and the flue gas. On the other hand, increasing the dimensionless space between the tubes in a staggered tube bundle reduces the volumetric heat transfer density because the increase in the tube spacing increases the TMC heat exchanger volume, which makes the change in the volume dominant in comparison with the change in the heat transfer rate, resulting in reduced volumetric heat transfer density.

In another work, Soleimanikutanaei et al. [54] studied the performance of the two-stage TMC heat exchanger in terms of the effects of the longitudinal and transversal pitches of TMC tubes, and they found that the condensation rate and the flue gas have a similar behavior because of the effect of the latent heat on the total heat transfer. Also, they studied the performance of the shell and tube TMC transport membrane condenser at different operating conditions [9, 13].

Wang et al. [55] used the ceramic membrane condenser to experimentally study the heat and water transfer from gaseous streams. Their results showed that the heat and mass transfer rates through the membrane could be increased by increasing the flow rate and

temperature of the inlet gas stream as well as the water flow rate while increasing the flow rate of the gas stream has an inverse effect on heat and water recovery. However, changing the membrane pressure did not affect the heat and water recovery.

Xiao et al. [38] used a lumped-parameter model. They assumed that the water vapor in the flue gas stream continuously condenses in membranes and completely blocks the membrane pores, while the other non-condensable gas components can hardly pass. Zhang et al. [41] used Stefan Maxwell's theory to model the different flue gas components' diffusion through the coating layer, and the selectivity of the coating layer is modeled to realize component separation. They employed the diffusion coefficient of Stefan Maxwell between the different gases and between gas and porous material.

Most of the simulation studies on the heat and mass transfer of TMC tube bundle were conducted based on the assumption that all the condensate water is recovered and transported to the cooling water through the porous membrane, which means the water vapor being condensed is equal to the transported water. Recently, the experimental work of [56] on the macroporous ceramic membrane revealed that the ceramic membrane cannot completely recover all the condensates under different operating conditions. They found that part of the condensate on the outer surface of the ceramic membrane drops into the flue gas and drains out as an acidic liquid after reacting with SO_2. The existence of the acidic liquid in the tube bundle can harm the heat exchanger. Also, mixing the condensate with fine particles blocks the pores of the porous membrane and causes membrane fouling, which reduces the porous membrane's performance. Therefore, modeling the TMC tube

bundle using a multiphase can provide information that cannot be obtained by using the single-phase model. The multiphase model can calculate the possible amount of condensate water inside the flue gas domain, which is based on the flue gas temperature, vapor content and ceramic membrane tube wall temperature.

A summary of the existing works related to heat and mass transfer in TMC is provided in Table 1. It can be seen from the table that most of the studies on the TMC are focused on the effects of the operating conditions on underlying heat and mass transfer performance. However, the effects of the geometrical parameters, such as tube diameter, number of tube rows, and Reynolds numbers on the condensation rate and thermal outlet conditions, need more investigation.

1.5. TMC Based Heat Exchanger Configurations

Different arrangements/configurations of TMC-based heat exchangers have been studied in the literature, such as in-line and staggered tube bundles [9-11], and shell-and-tube bundles [12-14]. Similar technologies using hollow fiber membranes were also reported [41, 44].

In the staggered configuration of TMC, the porous tubes are collected in the form of staggered tube bundles. The water flows inside the membrane tubes, while the flue gas flows in a crossflow direction to the TMC, while. In contrast, the water vapor from the flue gas continuously condenses on the pores of the membranes, which blocks the non-condensable gases from passing through the membranes.

Table 1: TMC Literature Review Summary

Year	Porous Membrane type	TMC/Arrangement	Flue gas source/ composition	Parameter studied/Ranges	Type of Study	Ref.
2021	Ceramic membrane, 1µm	40 tubes staggered	Coal-fired power plants	S_l= 3-8 cm, $T_{fg,i}$=49–53 °C, $T_{cw,i}$ =30–36°C $\dot{m}_{cw,i}$ = 10– 22.23 kg/m^2.h	Experimental, pilot scale	[50]
2020	Ceramic membrane, 1µm	Stage 1: 238 tubes Stage 2: 40 tubes	Coal-fired power plants. H_2O (vapor), CO_2, O_2, N_2, SO_2, SO_3, Ash	$V_{fg,i}$ = 0.34 - 2.12 m/s, $V_{cw,i}$ =0.19 - 0.21 m/s S_l= 30 -200 mm	Experimental, pilot scale	[36]
2020	Ceramic membrane, 1µm	Single ceramic tube	Coal-fired power plants	$T_{fg,i}$= 40–60 °C, $\dot{m}_{fg,i}$ = 6.25 × 10^{-5} -3.125 × 10^{-4} kg/s $T_{cw,i}$=15-35°C, $\dot{m}_{cw,i}$ =8.32 × 10^{-3} - 3.327 × 10^{-2} kg/s	Experimental lab scale	[51]
2020	-	40 tubes staggered	Coal-fired, H_2O (vapor), CO_2, O_2, N_2, SO_2, SO_3, Ash	$T_{cw,i}$=24-36°C, Effect of condensation mechanism	Experimental, pilot scale/ Numerical study	[57]
2020	Ceramic membra, 0.4 nm	46 tubes staggered	Coal-fired power plants	$T_{fg,i}$= 35-55°C, $\dot{m}_{fg,i}$ = 300-3000m^3/h, $T_{cw,i}$=12-38°C Effect of condensation mechanism	Experimental, pilot scale	[58]
2020	Ceramic membrane, 1 - 3 µm	46 tubes staggered	Simulated H_2O (vapor), CO_2, O_2, N_2	$T_{fg,i}$= 40-50°C, $\dot{m}_{fg,i}$ = 1.1 × 10^6-1.5× 10^6 m^3/hr $T_{cw,i}$=20-25°C, $V_{cw,i}$ =0.8-1.8m/s, A_{sur}=400-3900 m^2	Numerical/Single phase	[59]
2019	Ceramic membrane - 30 nm	Single tube	Simulated. N_2 and H_2O (vapor)	$T_{fg,i}$= 50-70°C, $\dot{m}_{fg,i}$ = 0.5 − 2.0 kg/s $T_{cw,i}$=5-50°C, $\dot{m}_{cw,i}$=1-9kg/s, d_i=8-12mm	Experimental lab scale /Numerical/Single phase	[38]
2019	Ceramic membranes, 6-8 nm	78 tubes staggered	H_2O (vapor), CO_2, O_2, N_2	$T_{fg,i}$= 70-80 °C, $\dot{m}_{fg,i}$ =42-116 kg/hr $T_{cw,i}$=20-34 °C, $\dot{m}_{cw,i}$=62-138 kg/hr, S/D=0.3-2.2	Numerical Mixed Condensation model	[11]
2019	Ceramic membrane, 1 µm	46	Gas-fired boiler	$T_{fg,i}$= 40-60 °C, $\dot{m}_{fg,i}$ =1000-1600 m^3/hr $T_{cw,i}$=20-32 °C, $\dot{m}_{cw,i}$=600-1100 L/hr	Experimental lab scale	[52]
2018	Ceramic membranes, 6-8 nm	78 tubes staggered	H_2O (vapor), CO_2, O_2, N_2	Inlet water vapor mass fraction =0.01-0.1, S/D =0.9-1.25	Numerical/Single phase	[10]
2018	Ceramic membrane, 13 nm	Single tube	Simulated	$V_{fg,i}$= 0.65–2.87 m/s, Re= 0.74 × 10^2–1.13 × 10^3 , water content=4-12.5 g, Porosity=0.6-0.78 Thickness of condensate layer= 2 × 10^{-3}–0.6 mm	Experimental/numerical/ single phase	[60]
2018	Ceramic membrane, 20, 30, 50, 100 nm	Single tube	Simulated. N_2 and H_2O (vapor)	$T_{fg,i}$= 50-70 °C, $\dot{m}_{fg,i}$ = 4-18 L/min, RH%=20-100%, permeate vaccum = $-0.1 - -0.005Mpa$	Experimental lab scale	[61]

2017	Ceramic membranes, 20 nm	-	Air- H_2O (vapor) mixture	$T_{fg,i}$= 80-120 °C, $\dot{m}_{fg,i}$ = 2.25-6.75L/min, $T_{cw,i}$ = 25-50 °C, $\dot{m}_{cw,i}$=1-10 L/hr, humidity ratio=15-120 g/kg	Experimental/ lab scale	[62]
2017	Ceramic membranes, 20nm	-	H_2O (vapor), N_2	$T_{fg,i}$= 50-70 °C, $\dot{m}_{fg,i}$ =2–18 L/min, RH%=40-100% water content=5.62–22.24 wt.%, $T_{cw,i} = 16 - 65$°C	Experimental/lab scale	[2]
2017	-	Single tube	Simulated	$T_{fg,i}$= 50-85 °C, Mass transfer flux= 0 - 0.000325 kg/m^2.s	Numerical/Single phase	[63]
2017	Hollow fiber membrane	Polymer membranes module	H_2O (vapor), CO_2, O_2, N_2	$P_{fg,i}$=200-600 KPa, pressure difference=6-22 KPa, porosity=0.4-0.8, Embedding ratio=0.05-0.2	Numerical/ Maxwell Stefan theory	[42]
2016	Ceramic membranes, 8–10nm	multichannel ceramic membrane	Humidified air	$T_{fg,i}$= 45-85 °C, $V_{fg,i} = 0.33 - 1.32$ m/s $V_{cw,i} = 0.08 - 0.55$ m/s, transmembrane pressure difference= 0.02-0.10 Mpa	Experimental/lab scale	[64]
2015	Ceramic membranes, 6-8 nm	78 tubes staggered	Natural gas H_2O (vapor), CO_2, O_2, N_2	$T_{fg,i}$= 64.7-93.5 °C, $\dot{m}_{fg,i}$ =2.36-2.80 kg/min $T_{cw,i}$ =19.1-44.6°C, $\dot{m}_{cw,i}$=1.71- 8.35 kg/min Inlet water vapor mass fraction =5.3-11.3 wt.%	Experimental/ lab scale	[16]
2015	Ceramic membranes, 6-8 nm	Single tube	Steam	$T_{fg,i}$= 45-85 °C, $\dot{m}_{fg,i}$=1-4 L/hr, $\dot{m}_{cw,i}$=2.5-15 L/hr	Experimental/ Numerical	[55]
2013	ceramic membranes, 6-8 nm	78 tubes staggered	H_2O (vapor), CO_2, O_2, N_2	$T_{fg,i} = 60 - 88$ °C, Re= 6.4–330(water side) Re= 1.0× 10^3–7.0× 10^4 (based on hydraulic diameter)	Numerical/two-step chemical reactions/Single Phase	[8]
2021	**Ceramic membranes, 6-8 nm**	**13-78 tubes staggered**	**H_2O (vapor), CO_2, O_2, N_2**	**Extensive parametric study covered the geometrical parameters and operating conditions, and nanoporous membrane characteristics Dominant condensation mode investigation Proposed new TMC correlations: $\overline{Nu}_{cond}^{corr}$, $\overline{Nu}_{cond-conv}^{corr}$, $f^{correlated}$ Proposed new Multiphase model coupled with Darcy transport model. Investigate the actual transport of water vapor vs. the total condensation**	**Numerical**	**Current research**

1.6. Condensation phenomena in the TMC

In applying flue gas membrane condensers, the capillary condensation mode is the transport phenomenon that allows the vapor to condense inside the membrane pore structure, which completely blocks the pores and stops the transport of the non-condensable gases.

GTI's experimental study [30] found that the nanoporous membrane has poor separation characteristics and low water vapor transport flux when working under the Knudsen diffusion transport mechanism compared with the capillary transport mechanism. This occurs when the flue gas stream is cooled to an adequately low temperature that allows the relative humidity of the flue gas to increase, as seen in Figure 8. Capillary condensation increases water vapor transport flux and separation ratio by more than 5 times and 100 times, respectively, over the water vapor transport by the Knudsen diffusion mechanism.

Calculating the condensation rate numerically is one of the challenging steps in performing a numerical study in the TMC heat exchanger. Different models were proposed in the literature to calculate the condensation rate, such as the lumped parameter model [38], Stefan Maxwell theory [41], mixed condensation model [10, 11], Fick's diffusion law [14], and two-step chemical reactions on the outer surface of the TMC tubes, by Lin et al. [17]. These models proved to be efficient in calculating the transport of water through the nanoporous membrane. Fick's diffusion law is based on the condensate vapor toward a cold surface, and it was used to simulate Chapter 3. Since the transport of water through the nanoporous ceramic membrane involves two mechanisms, capillary condensation and

the wall condensation, the mixed condensation, which is based in a linear combination of both mechanisms, was used to perform all the calculations in Chapters 4 – 6, in this study.

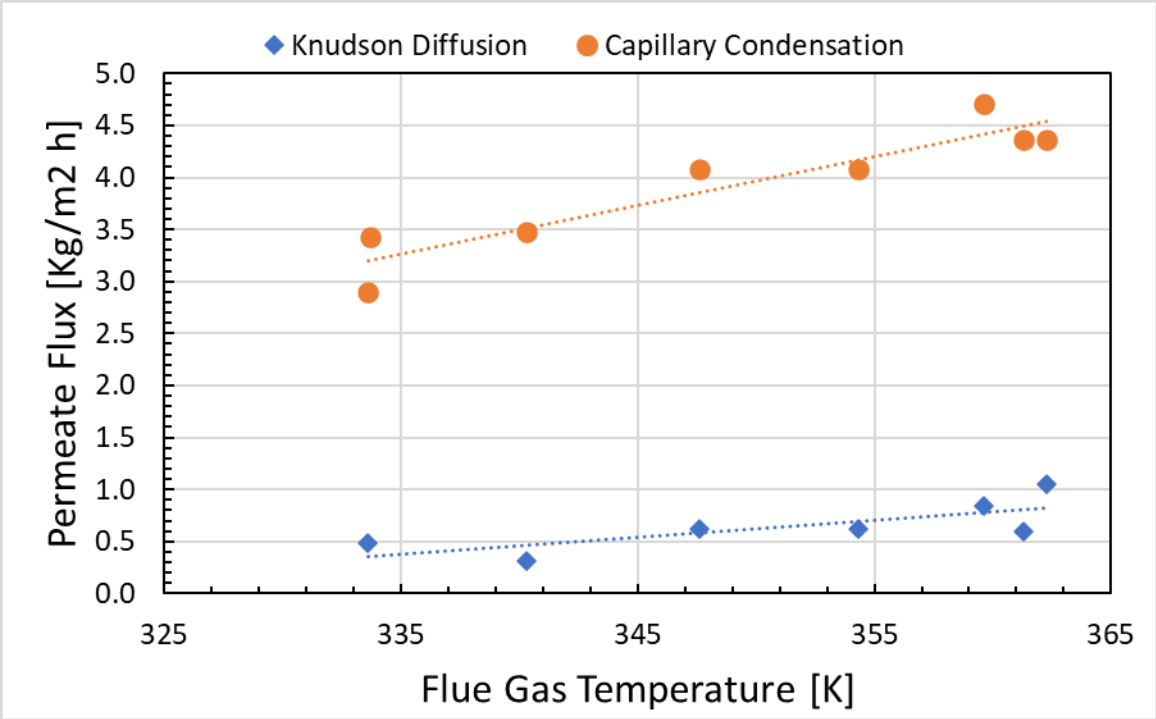

Figure 8. Experimental Transport Mode of Water Through the Ceramic Membrane [30].

1.7. Flue Gas Characteristics

Flue gases exhaust streams from electricity-generating power plant units using fossil fuels are major concentrated CO_2 sources in the US with high water vapor content. Flue gas is defined as the combustion exhaust gas produced at power plants and contains combustion products mixed with air, such as large amounts of water vapor and small amounts of non-condensable gases. Flue gas mixture usually includes carbon dioxide, oxygen, nitrogen, water vapor, particulates, heavy metals, nitrogen oxides (NOx), and sulfur dioxide (SO_2).

The outlet temperature of the typical flue gas furnace generally is around 1473 K, which decreases gradually along the heat transfer pathway. The flue gases entering the stack are around 423 K. The advanced equipment used for pollution control can effectively remove NO_x, SO_x, and particulate matter. However, CO_2, O_2, and H_2O remain with flue gas.

The flue gas temperature is classified from low range temperature to medium range temperature. Table 2 represents the flue gas composition from natural gas-fired power plants and coal-fired boilers [65].

Table 2: Typical Flue Gases for Temperature Range of 350-450 K, as Reported in [65].

Flue gas composition	Natural gas-fired	Coal-fired
CO_2	8-10 %	12-14 %
H_2O	18-20 %	8-10 %
O_2	2-3 %	3-5 %
N_2	67-72 %	72-77 %

1.8. Single Phase Heat Transfer Correlations

Single-phase (no condensation) heat transfer from the impermeable tube bundles has been studied extensively in the literature [66], and many correlations have been developed. These correlations have focused on representing the relations in terms of the heat transfer coefficient as a function of pressure drop, tube spacing and diameters, and the number of tube rows in the bundle. For example, Grimison [67] correlated the test measurements of Pierson [68] and Huge [69] for staggered and in-line tube bundle arrangements. Hausen [70] modified the Grimison model. Zukauskas [71-73] reviewed the experimental studies

using air and water as working fluids for heat transfer from tube bank in cross flow, and defined heat transfer correlations of the staggered and in-line tube bundle for Reynolds numbers in the range of 1.0 to 106 and Prandtl numbers in the range of 0.7 to 500. Wilson and Bassiouny [74] performed a numerical study for both laminar and turbulent flow across tube banks for in-line and staggered tube arrangements using the air as a working fluid (Pr = 0.7). The literature survey shows that most previous correlations were developed based on experiments using air as a working fluid. However, the air's physical properties differ from those of flue gas.

The air Prandtl number is between 0.707 - 0.698 at a temperature range of 300 - 400 K and 100 Kpa. The flue gas Prandtl number was between 0.73 - 0.76 at a Reynold number range of 300 - 9000 and a temperature of around 355 K. Also, several models have been developed to calculate the single-phase pressure drop in the heat exchanger, such as the Holman-Jakob model developed in 1938 [75], Gunter-Shaw Model developed in 1945 [76], the correction by Boucher and Lapple in 1945, and the Zukauskas pressure drop model [77]. Boucher and Lapple [77] summarized that it is unsound to represent the pressure drop of a tube bundle in a single relationship for different ranges of Reynolds number, and no correlation can be likely to represent the data of all researchers to better than ± 30%.

The hydraulic resistance is defined as the total pressure drop of flow in a cross-flow tube bundle. As is known, the total pressure drop across a bank is a function of tube bundle arrangement, flow velocity, and fluid physical properties. Zukauskas [71] found that based on their study of 49 different inline and staggered tube bundles for both air and liquids in flows, the most effective parameter of the hydraulic resistance is the transverse pitch, as it

increases with the increase of the transverse pitch. Increasing the longitudinal pitch increases the tube spacing between the rows, which allows the formation of the vortices that affect the pressure resistance. Wilson and Bassiouny [74] confirmed the positive relationship between the longitudinal pitch and the pressure drop and friction factor numerically.

1.9. Multiphase Numerical Modeling

Modeling the flue gas inside the TMC heat exchanger is complex in nature, and the existence of the water vapor phase change inside and outside the nanoporous membrane increases the flow convolution. The literature reported many works related to the multiphase flow in the porous material, but not for a TMC, and the following is a summary of the related literature.

Tahir et al. [78] modeled the multiphase flow of Nitrogen flow through an absorber tube filled with porous media. The porous media is a ceramic monolith porous substrate. They used the Eulerian multiphase flow model and the available porous model (Darcy's law) in ANSYS Fluent to model the pressure drop and velocity flow inside the porous media.

Wang et al. [79] and Brannock et al. [80] used a porous media model using Ansys/Fluent to study the effects of hollow fiber membrane bundles on the flow field of the membrane bioreactor. They coupled the porous media model with the Eulerian multiphase model to study the hydrodynamic behavior of a full-scale submerged membrane bioreactor. In their model, the air was set as a dispersed phase, while the water/sludge mixture was a

continuous phase. Their work aimed to study the effects of pressure drops across the membrane bundles.

Piller et al. [81] used the VOF multiphase model coupled with the Darcy law porous model in Ansys/Fluent to simulate the oil/water flow in the pore-space of a sandstone rock (metal foam) at different ranges of Reynolds number.

Birgi et al. [82] developed a pore-scale model to evaluate the accuracy of predicting the multiphase flow in a microporous membrane for membrane distillation applications, using CFD methods as modeling tools. They evaluated the finite element method (FEM)-based phase field (PF) method using a COMSOL package and the finite volume method (FVM)-based volume of fluid (VOF) method applied in Star-CCM. Porto et al. [83] performed a Multiphase Fluid Flow analysis in Porous-Fibrous Media using the VOF and porous media models formulated by Darcy's law in Ansys/Fluent. They obtained different results of resin volumetric fraction, streamlines, and pressure. Chen et al. [84] used the convection-diffusion to model the vapor/liquid transport in the polymer-composite-based porous material, and the model considers both high-pressure convection in the pore network and continuum diffusion in solids. They combined Darcy's law, which will be described in detail in Chapter 6, the liquid-vapor chemical equilibrium, the conservation of mass law, and the ideal gas law to couple convection and diffusion. Ni et al. [85] investigated the multiphase flow inside biomaterial porous to predict moisture transport during intensive microwave heating. They found that internal heating and vaporization significantly enhanced the transport of vapor/liquid inside the biomaterial. They transported the vapor

inside the biomaterial by using convective (Darcy)-Diffusion law and the liquid by Darcy's law.

Different methods called "one fluid" were developed to study the phase boundary in different applications, such as volume-of-fluid (VOF) [86], phase field [87], the level-set [88], and CIP [89] methods. Due to the continuous movement of the interface between two phases, the physical properties of each phase would change, making the multiphase flow simulation more complicated than the single phase [90]. The VOF method is characterized as a mass conservation property and can easily capture the interface between the phases [91]. The theoretical formulation of the VOF model is based on the assumption that each cell in the computational domain is filled by one phase or a combination of two phases. Yang et al. [92] used the VOF model to study the two-phase flow behavior during flow boiling in coiled tubes. They modeled the evaporation flow using the Lee model in the UDF. Mghari et al. [93] used the multiphase VOF model to investigate the water vapor capillary condensation in a microchannel under different Reynolds numbers and mass fluxes. They used the Lee evaporation-condensation model to model the mass transfer between the phases. Sun et al. [91] used the fluent VOF multiphase model to simulate the phase change. They proposed a new phase-change model that is more suitable under the two-phase condition of one unsaturated but the other saturated. Sandra et al. [95] used the VOF method to simulate the two-phase flow of a hydrocarbon feedstock. They modeled the mass transfer between phases using the Lee model written in the UDF and applied it to the mass conservation Equations for each phase. They assumed no momentum exchange between the two steps. They used the Piecewise Linear Interface Calculation (PLIC)

method to reconstruct the interface between both phases in each computational cell. Due to the multiphase flow dynamic behavior, they applied a transient simulation with a time step of 0.001 s and obtained a complete boiling process after 14.67 s of real-time.

1.10. Proposed Research Objective

The primary goal of the present research is to study and design a transport-membrane-condenser-based heat exchanger involving complex heat and mass transfer for waste-heat and water recovery. The completion of this objective is supported by multiple objectives including single-phase modeling of heat and mass transfer of the TMC-based heat exchanger; an extensive parametric study on the TMC geometrical parameters, membrane properties, and operating conditions; modeling the condensation from the flue gas; deriving TMC correlations; and performing related multiphase modeling. Each of these specific objectives is detailed below to set the focus of the present research:

- Examine two different condensation models available in the literature: the wall-condensation-based Fick's diffusion law, and the mixed condensation model to determine the best model that can predict the experimental condensation rate.
- Perform a parametric study using a single-phase multispecies transport model coupled with the wall-condensation-based Fick's diffusion law to study the effects of the membrane properties and geometrical parameters, such as tube diameter and thickness under different operating conditions (including inlet water temperature and flow rate as well as inlet flue gas temperature and flow rate), on the condensation rate and outlet thermal conditions.

- The heat transfer, mass transfer, and pressure drop imposed by the crossflow ceramic nanoporous tubes in Transport Membrane Condenser (TMC) will be modeled numerically using the single-phase-multispecies model coupled with a mixed condensation model. The study will cover a wide range of tube diameters, number of rows, and Reynolds number, under flue gas condensation to determine the optimum conditions of the TMC tube bundle.
- Investigate the impact of the turbulence intensity of the flue gas at various inlet conditions, such as Reynolds numbers and temperatures, on the heat and mass transfer and pressure drop characteristics.
- Investigate the dominant condensation rate in the transport membrane condenser.
- Due to a lack of heat/mass transfer and pressure drop correlations for the porous membrane tubes with condensing flue gas, the following two tasks will be undertaken:
    - The numerical results with condensing flue gas will be compared to the literature's functional correlations for single-phase Nusselt number and pressure drops. To study the similarities and variations between the TMC Nusselt number and pressure drops as well as the single-phase correlations to avoid misuse.
    - Proposed a new empirical TMC correlation for heat/mass transfer and pressure drop with respect to condensation rate, the number of rows, and the nanoporous membrane geometrical properties.
- Proposed multiphase modeling of heat and mass transfer inside the TMC-based heat exchanger coupled with condensation-evaporation Lee's model and Darcy's

law. The model will be able to calculate the actual water condensation inside the flow gas domain using the VOF multiphase model and the transported water through the membrane tube using Darcy's law.

2. CHAPTER II: CFD MODELING METHODOLOGY AND FORMULATION

In this chapter, the governing Equations, thermodynamic properties of flue gas, and condensation models will be illustrated in detail. Besides, the numerical TMC model, the reference experimental model, and the validation of the condensation models will be performed by comparison of the numerical results with the published experimental results. The flow dynamics in the TMC are simulated by solving a system of partial differential Equations (Navier-Stokes Equations) using Ansys/Fluent 2019 R1 [96]. Ansys/Fluent have been used for years successfully in modeling the heat and mass transfer and design and structural analysis in different engineering aspects [12-14, 80- 83, 97-98]

2.1. Single Phase Numerical Model

The Reynolds averaged Navier–Stokes (RANS) model is used to predict the turbulent flow. The RANS model is chosen for the quick simulation and less computational resource requirements compared to transient models such as LES and DES.

2.1.1. Basic Conservation Equations

The RANS format of the governing Equations [99] for fluid flow is used to solve the mass, momentum, and energy conservation Equations as shown below.

Mass Conservation (Continuity Equation):

$$\frac{\partial \rho}{\partial t} + \nabla.(\rho \bar{u}) = 0 \tag{1}$$

Momentum Conservation:

$$\frac{\partial}{\partial t}(\rho \bar{u}) + \nabla.(\rho \bar{u}\bar{u}) \quad = -\nabla \bar{p} + [\nabla.(\vec{\tau} - \overline{\rho u' u'})] + \rho \vec{g} \tag{2}$$

where ρ, $\vec{g}$, ∂t, $\bar{u}$ and u' are density [kg/m^3], gravitational body forces [m/s^2], time step [s], Reynold average velocity vector [m/s], and fluctuating component of velocity in time [m/s], respectively. The average stress tensor is defined as:

$$\vec{\tau} = \mu \left[(\nabla \bar{u} + \nabla \bar{u}^T) - \frac{2}{3}(\nabla.\vec{\bar{u}})I \right] \tag{3}$$

where μ is the molecular viscosity [kg/m.s], and I is the unit tensor.

The Reynolds stress tensor $-\rho\overline{u'u'}$ is based on the Boussinesq hypothesis, which assumes that the Reynolds stress is a linear function of the mean velocity gradients. The Reynolds stresses are unknown; in the turbulence viscosity model such as and $k - \varepsilon$ model, the turbulent viscosity μ_t is used to relate the Reynolds stresses with the mean velocity gradient. For incompressible flows, the Reynolds stress tensor is expressed in the form [99]:

$$-\rho\overline{u'u'} = \mu_t(\nabla \bar{u} + \nabla \bar{u}^T) - \frac{2}{3}\rho k\mathrm{I} \tag{4}$$

where k and μ_t are turbulent kinetic energy [m^2/s^2] and turbulent viscosity [kg/m.s], respectively.

Energy Conservation:

$$\frac{\partial}{\partial t}\left(\rho c_p \bar{T}\right) + \nabla.\left(\rho c_p \bar{u}\bar{T}\right) = \nabla.\left[k\nabla\bar{T} - \rho c_p \overline{u'T'}\right] + \overline{S^T} \quad (5)$$

where $\bar{T}$ and T' are respectively Reynolds average and fluctuation temperature [K], c_p is the heat capacity at constant pressure [J/kg.s], and the S^T is given as follows:

$$S^T = \dot{q}_V + \rho T \frac{Dc_p}{Dt} \quad (6)$$

where $\dot{q}_V$ is the rate of heat source or sink [W/m^3].

2.1.2. Species Transport Model

A multispecies transport model has been used to model the transport process of different species of flue gas and water in the computational domain. ANSYS/Fluent calculates the local mass fraction of each species, out of the convection-diffusion Equation solution for the i^{th} species. The multi-species transport that occurs in the flue gas mixture is governed by the following Equation:

$$\frac{\partial}{\partial t}(\rho Y_i) + \nabla.(\rho u Y_i) = -\nabla.J_i + R_i + S_i \quad (7)$$

where Y_i is the mass fraction of the i^{th} species, S_i is the rate of the creative source term, and R_i is the net rate of production by chemical reaction of the species being calculated.

Since we are dealing with the flue gas (multispecies flows), the mass diffusion coefficients are required for solving the species transport Equations. The mass diffusion coefficients are used to compute the chemical species diffusion flux in a laminar flow through Fick's diffusion law.

The mass diffusion coefficient for i^{th} species, J_i, is the diffusion flux for laminar species transport Equations using the thermal and mass diffusion coefficients, called Fick's diffusion law [100]:

$$J_i = -\rho D_{i,m} \nabla Y_i - D_{T,i} \frac{\nabla T}{T} \tag{8}$$

For the turbulent flow, Equation (8) is rewritten in the form:

$$J_i = -\left(\rho D_{i,m} + \frac{\mu_t}{Sc_t}\right) \nabla Y_i - D_{T,i} \frac{\nabla T}{T} \tag{9}$$

where $D_{i,m}$ and $D_{T,i}$ are respectively the mass and thermal diffusion coefficients for species i in the mixture m, $Sc_t = \frac{\mu_t}{\rho D_t}$ is the effective Schmidt number due to turbulence flow, μ_t is the eddy viscosity, and D_t is the effective mass diffusion coefficient due to turbulence.

2.1.3. Turbulence Model

The fluctuation of the velocity as a result of turbulence affects the transport of mass, momentum, and energy. Computationally, direct simulation of velocity fluctuations and its effect is not practical. RANS model can handle such kind of turbulence. However, the unknown terms were introduced into Navier Stokes Equations when converted to the RANS format, which required additional turbulence Equations to solve the flow Equations. Various turbulence models are available to solve the turbulent flow field. In this study, the turbulence model was selected based on the Y_{plus} of the generated mesh. The y_{plus} value is a dimensionless physical parameter that is used in describing the viscous sublayer in the

boundary layer near the wall. Since the Y_{plus} of the generated nesh value is less than 2, the shear stress transport SST $k-\omega$ has been chosen for the simulation of the tube membrane model [101-103].

The shear stress transport SST $k-\omega$ is a $k-\varepsilon$ model converted into $k-\omega$ to efficiently combine the accuracy and strong formulation of the $k-\omega$ in the near-wall region with the free-stream independence $k-\varepsilon$ of the $k-\varepsilon$ model in the far field. The SST $k-\omega$ model is derived from the standard $k-\omega$ model in the inner region of the boundary and the $k-\varepsilon$ model is applied in the outer part of the boundary layer. Both models, the standard $k-\omega$ model, and the transformed $k-\varepsilon$ model are multiplied by a blending function and added together in the near-wall region. The standard $k-\omega$ model is activated by setting the blending function as one, while in the region far away from the surface the standard $k-\varepsilon$ model is activated by setting the blending function to 0.

The turbulence kinetic energy k , and the dissipation rate ω, were obtained by solving the following transport Equations using fluent software [103]:

$$\frac{\partial}{\partial t}(\rho k)+\frac{\partial}{\partial x_i}(\rho k\bar{u}_i)=\frac{\partial}{\partial x_j}\left[\Gamma_k\frac{\partial k}{\partial x_j}\right]+\tilde{G}_k-Y_k+S_k \tag{10}$$

$$\frac{\partial}{\partial t}(\rho \omega)+\frac{\partial}{\partial x}(\rho \omega\bar{u}_i)=\frac{\partial}{\partial x_j}\left[\Gamma_\omega\frac{\partial k}{\partial x_j}\right]+G_\omega-Y_\omega+D_\omega+S_\omega \tag{11}$$

where S_ω and S_k are user-defined source terms. The effective diffusivities, Γ_k and Γ_ω, are respectively given by:

$$\Gamma_\omega=\mu+\frac{\mu_t}{\sigma_\omega} \tag{13}$$

$$\Gamma_k = \mu + \frac{\mu_t}{\sigma_k} \tag{14}$$

where μ_t is the turbulent viscosity modeled given as follows:

$$\mu_t = \frac{\rho k}{\omega} \frac{1}{max\left[\frac{1}{\alpha^*}, \frac{SF_2}{\alpha_1 \omega}\right]} \tag{15}$$

where S is the strain rate magnitude, and α^* is the damp coefficient for the turbulent viscosity which corrects a low Reynolds number.

$$\alpha^* = \alpha^*_\infty \left(\frac{\alpha^*_0 + \frac{Re_t}{R_k}}{1 + \frac{Re_t}{R_k}} \right) \tag{16}$$

where $Re_t = \frac{\rho k}{\mu \omega}$, $R_k = 6$, and $\alpha^*_0 = \frac{\beta_i}{3}$, $\beta_i = 0.072$.

$$\alpha^*_\infty = F_1 \alpha_{\infty,1} + (1 - F_1)\alpha_{\infty,2} \tag{17}$$

$$\alpha_{\infty,1} = \frac{\beta_{i,1}}{\beta^*_\infty} - \frac{k^2}{\sigma_{\omega,1}\sqrt{\beta^*_\infty}} \tag{18}$$

$$\alpha_{\infty,2} = \frac{\beta_{i,2}}{\beta^*_\infty} - \frac{k^2}{\sigma_{\omega,2}\sqrt{\beta^*_\infty}} \tag{19}$$

σ_ω and σ_k in Equation (13) and (14) are the turbulent Prandtl numbers for ω and k, respectively, and are modeled as :

$$\sigma_\omega = \frac{1}{\frac{F_1}{\sigma_{\omega,1}} + \frac{(1-F_1)}{\sigma_{\omega,2}}} \tag{20}$$

$$\sigma_k = \frac{1}{\frac{F_1}{\sigma_{k,1}} + \frac{(1-F_1)}{\sigma_{k,2}}} \tag{21}$$

F_1 and F_2 are the blending functions and are given respectively by:

$$F_1 = \tanh(\vartheta_1^4) \tag{22}$$

$$\vartheta_1 = \min\left[max\left(\frac{\sqrt{k}}{0.09\omega y}, \frac{500\mu}{\rho y^2 \omega}\right), \frac{4\rho k}{\sigma_{\omega,2} D_\omega^+ y^2}\right] \tag{23}$$

where D_ω^+ and y are the positive portion of the cross-diffusion term and the distance to the next surface, respectively.

$$D_\omega^+ = \max\left[2\rho \frac{1}{\sigma_{\omega,2}} \frac{1}{\omega} \frac{\partial k}{\partial x_j} \frac{\partial \omega}{\partial x_j}, 10^{-10}\right] \tag{24}$$

$$F_2 = \tanh(\vartheta_2^2) \tag{25}$$

$$\vartheta_2 = \max\left[2\frac{\sqrt{k}}{0.09\omega y}, \frac{500\mu}{\rho y^2 \omega}\right] \tag{26}$$

The production of turbulence kinetic energy, $\tilde{G}_k$, and production of ω, $\tilde{G}_\omega$, are respectively defined as:

$$\tilde{G}_k = min(G_k, 10\rho\beta^* k\omega) \tag{27}$$

$$G_\omega = \frac{\alpha}{v_t} \tilde{G}_k \tag{28}$$

The dissipation of turbulence kinetic energy, Y_k, and the dissipation of ω, Y_ω, are respectively defined as:

$$Y_k = \rho\beta^* k\omega \tag{29}$$

$$Y_\omega = \rho\beta_i \omega^2 \tag{30}$$

$$\beta_i = F_1\beta_{i,1}(1 - F_1)\beta_{i,2} \tag{31}$$

The cross-diffusion term D_ω is a result of blending the standard k − ε model and the standard k − ω model to generate the SST k − ω, which is defined as:

$$D_\omega = 2(1 - F_1)\rho\sigma_{\omega,2}\frac{1}{\omega}\frac{\partial k}{\partial x_j}\frac{\partial \omega}{\partial x_j} \tag{31}$$

The SST k − ω model constants, default fluent constants, used to run the simulation are $\sigma_{k,1} = 1.176$, $\sigma_{k,2} = 1.0$, $\sigma_{\omega,1} = 2.0$, $\sigma_{\omega,2} = 1.168$, $\beta_{i,1} = 0.075$, $\beta_{i,2} = 0.0828$, $\alpha_1 = 0.31$, $\alpha_\infty^* = 1.0$, $\alpha_\infty = 0.52$, $\alpha_0 = \frac{1}{9}$, $\beta_\infty^* = 0.09$.

2.2. Modeling of Condensation Inside TMC

Different models were proposed in the literature to calculate the condensation rate, such as the lumped parameter model [38], Stefan Maxwell theory [41], Mixed condensation model [10, 11], Fick's diffusion law [14], and the two-step chemical reactions on the outer surface of the TMC tubes [17]. These models proved their efficiency in calculating water transport through the nanoporous membrane [38, 41, 10,11,14]. The current research will focus on using Fick's diffusion law and Mixed condensation model, and then based on the testing and validation, the heat and mass transfer analysis will be performed.

2.2.1. Wall-based condensation (Fick's diffusion law)

A wall condensation model based on Fick's diffusion law (Mechanistic model) in the membrane tube has been used to model the membrane's heat and mass transfer processes. This model is capable of simulating the transport of the water vapor and heat from the flue-gas zone to the porous zone and from there to the cooling water zone in a TMC heat exchanger.

The wall condensation assumption was first derived and discussed by Dehbi et al. [104]. They assumed that the steam condensation rate, in the presence of non-condensable gases, toward the cold surface is governed by condensable gas diffusion rate using ANSYS CFD code FLUENT. They applied the condensation model and the sink/source terms using an appropriate User Defined Functions (UDF). They ignored the effect of the thermal resistance of the liquid film. Their model applies to a mixture with a significant mass fraction, more than 0.1, of non-condensable gases. Soleimanikutanaei et al. [12-14] applied this approach to calculate the water vapor condensation rate on the nanoporous ceramic membrane.

Dehbi et al. [104] performed a sequence of assumptions and used a subsequent formulation of the transport formula derived by Bird et al. [105] to derive the wall-based condensation, as described herein. The mass fluxes for water vapor (condensable species) and the non-condensable species at the liquid-vapor interface comprise both diffusive and convective components, as given below:

$$\dot{m_{nc}'} = \rho Y_{nc} u - \rho D \frac{\partial Y_{nc}}{\partial n} \tag{32}$$

$$\dot{m}'_c = \rho Y_c u - \rho D \frac{\partial Y_c}{\partial n} \tag{33}$$

where Y_c and Y_{nc} are the mass fraction of condensable and non-condensable species, u and ρ are the mixture velocity and density, n is the normal direction to the wall, and D is the mass diffusion coefficient.

The mixture mass flux at the liquid-vapor interface is the addition of the mass flux of different species in the mixture and equal to unity, and can be written as:

$$\dot{m}'_c + \dot{m}'_{nc} = \rho u \tag{34}$$

where $\dot{m}'_{nc} = 0$ due to the fact that the non-condensable gases cannot penetrate the permeable surface. The mass flux of the condenses at the wall can be expressed by the following Equation:

$$\dot{m}'_c = \rho u = \frac{1}{(Y_c - 1)} \rho D \frac{\partial Y_c}{\partial n} \tag{35}$$

In Ansys/Fluent, the condensation rate toward a cold wall can be applied as a sink in the continuity Equation of cells next (shadow cells) to the wall, by the given Equation:

$$\dot{m}''_c = \dot{m}'_c \frac{A_{cell}}{V_{cell}} \tag{36}$$

$$\dot{m}''_c V_{cell} = \rho Y_c u A_{cell} - \rho D \frac{\partial Y_c}{\partial n} A_{cell} \tag{37}$$

where A_{cell} and V_{cell} are the adjacent cell surface and volume.

By substituting Equation (35) into Equation (37), the final form of the source term that accounts for the condensation of the water vapor at the wall can be defined in the continuity Equation:

$$\dot{m}'' = \frac{1}{(Y_c - 1)} \rho D \frac{\partial Y_c}{\partial n} \frac{A_{cell}}{V_{cell}} \tag{38}$$

The subsequent sink term for water vapor condensation needs to be included in the water vapor species Equation, which can be written as:

$$\dot{m}_v'' = Y_c \dot{m}'' \tag{39}$$

$$\dot{m}_v'' = Y_c \frac{1}{(Y_c - 1)} \rho D \frac{\partial Y_c}{\partial n} \frac{A_{cell}}{V_{cell}} \tag{40}$$

The condensation rate on a solid wall is implemented as a sink term in the continuity Equation of the cells next to the cold wall. The source terms in the mass, species, and energy Equations are implemented to perform the heat and water transfer from the flue-gas along the porous tube wall. The sink terms respectively for the momentum Equation, S_m, the energy Equation, S_h, turbulent Equations, and S_k and S_ω for the adjacent wall cells in the flue-gas zone are calculated by the following relations:

$$S_{m-i} = U_i \frac{\dot{m}_v''}{Y_v} \tag{41}$$

$$S_E = h_v \frac{\dot{m}_v''}{Y_v} \tag{42}$$

$$S_k = k_{cell} \frac{\dot{m}_v''}{Y_v} \tag{43}$$

$$S_{\omega} = \omega_{cell} \frac{\dot{m}_v''}{Y_v} \tag{44}$$

where U_i is the mixture velocity, h_v is the enthalpy of the water vapor, k_{cell} and ω_{cell} the rate of turbulent kinetic energy and dissipation rate.

A sharp gradient in the boundary layer should be avoided, which may lead to an enhancement in heat, mass, and momentum transfer due to a strong condensation that could cause a possible suction effect or diffusion. A correction factor must be applied To avoid the suction effect according to Dhebi et al. [104]. Different correction factors were proposed in the literature, and the most common one is the Bird correction factor [105], which is given as:

$$\theta_B = \frac{\ln(1+B)}{B} \tag{45}$$

where B is the Bird suction parameter, defined as:

$$B = \frac{Y_{v,i} - Y_{v,\infty}}{1 - Y_{v,i}} \tag{46}$$

The subscripts i and ∞ denotes the interface and the bulk, respectively.

Consequently, the condensation rate toward a solid wall based on Fick's diffusion law of species, Equation (40), can be redefined as:

$$\dot{m}_{cond} = \theta_B \dot{m}_v'' = \theta_B Y_c \frac{1}{(Y_c - 1)} \rho D_{eff} \frac{\partial Y_c}{\partial n} \frac{A_{cell}}{V_{cell}} \tag{49}$$

The effective diffusion coefficient, $D_{eff} = D_{v,m} + D_t$ was used instead of the mass diffusion coefficient simultaneously with the correction factor, to avoid the no-slip condition that may occur when the correction factor is implemented in Equation (40). The effective diffusion coefficient will be active only in the boundary layer close to the condensing wall, at the wall-nearest cells.

The effective diffusion coefficient is defined as, $D_{eff} = D_{v,m} + D_t$, where $D_{v,m}$ is the diffusivity of species *v* in the mixture m, and D_t is the thermal diffusivity.

Using the User Defined Function, the source and sink terms have been implemented in the momentum, energy, and turbulence Equations. This is based on the assumption that condensation of water vapor occurs when the wall temperature is less than the saturation temperature with respect to the water vapor partial pressure at the adjacent wall. Otherwise, the water vapor mass fraction at the wall is set equal to the value in the wall-adjacent cell.

The water vapor saturation pressure, P_v, is calculated using the following Equation:

$$P_v = P_{mix} \frac{M_{mix} Y_v}{M_v} \tag{50}$$

where M_v is the water vapor molar mass, M_{mix} is the mixture molar mass, and P_{mix} is the mixture pressure.

2.2.2. Capillary Condensation

The reported experimental work [28-30] confirmed that the transport of water through the nanoporous (6 nm) membrane is dominated by capillary condensation. Their results explain that water transport through the nanoporous ceramic membrane is low in the Knudsen diffusion mode, while the capillary condensation could transport the water much more efficiently when the desired flue gas conditions were met.

The capillary condensation phenomenon occurs when the vapor pressure is lower than the saturated liquid pressure. The capillary pressure is defined as the pressure difference at the interface between two unmixable fluids, such as oil and water, and can be defined as:

$$\mathcal{P}_c = \mathcal{P}_{nonwetting} - \mathcal{P}_{wetting} \tag{51}$$

The capillary pressure can also be defined by using the Young–Laplace Equation. Which depends on the wetting angle, θ, surface tension, σ, and the effective radius, r, of the interface. At the equilibrium (no flowing phases), the cylindrical vertical capillary, $\mathcal{P}_c$ is given as:

$$\mathcal{P}_c = \frac{2\sigma cos\theta}{r} = gh(\rho_1 - \rho_2) \tag{52}$$

where h is column height, g is the gravitational acceleration, ρ_1 and ρ_2 are the densities of the two fluids.

In a porous media, capillary pressure is defined as the force required to squeeze a liquid droplet through a pore throat of the porous material. The capillary force increases with a

decreased pore diameter, and it works against the interfacial tension between the two different phases, see Figure 9.

Capillary condensation of water vapor in the porous media is difficult, due to the non-uniformity and irregularity of the pore sizes of the inorganic porous membranes. Typically, the pores have no cylindrical shapes. Uchytil et al. [106] conducted a detailed analysis of the effect of condensation in porous material due to capillary pressure, as follows.

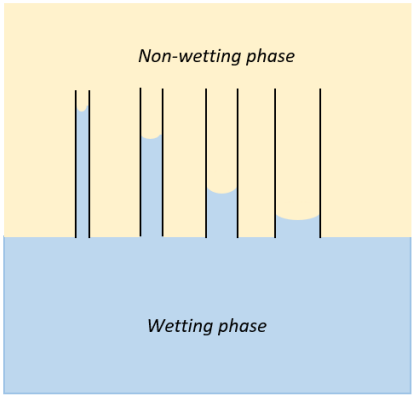

Figure 9. The Effect of Tube Diameter in Water Rises in the Capillary due to Capillary Pressure.

The effect of the pore radius and pressure on capillary condensation is described by Kelvin's Equation [107]:

$$\left(\frac{\rho RT}{M}\right)\ln\left(\frac{\mathcal{P}_c}{P_0}\right) = -\frac{2\sigma\cos\theta}{r} \tag{53}$$

where v is the interface condensation ($\mathcal{P}_c < P_0$).

The effect of non-uniformity of the geometrical configuration pores of the nanoporous material on the water transport was considered by including the tortuosity effect of the porous layer. The transport of a liquid in a porous material is modeled by Poiseuille flow:

$$\varphi = A\left(\frac{\varepsilon}{\tau}\right)\left(\frac{\rho r^2}{8\mu Mx}\right)\Delta\mathcal{P} \tag{54}$$

The tortuosity, τ, of the nanoporous ceramic membrane is governed by the following relation as a function of porosity, ε:

$$\tau = 1 - \frac{1}{2}\ln(\varepsilon) \tag{55}$$

The driving force for the liquid flow is the (capillary) pressure drop, $\Delta\mathcal{P}$, due to the liquid transport in the porous media with menisci, as derived from Young–Laplace Equation for liquid flux in pores with two menisci. Assuming the nanoporous layer is a straight nanopore, as represented in Figure 10, and the contact angles on both sides of the nanopore are the same.

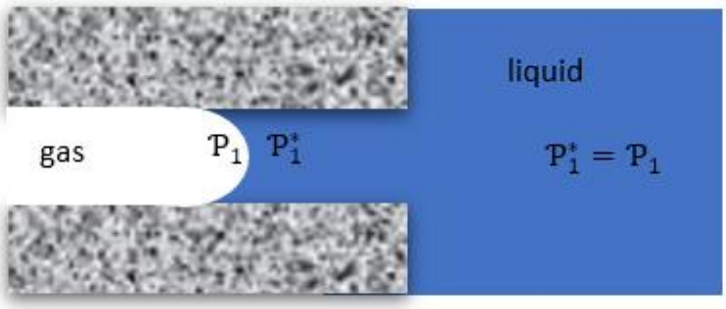

Figure 10. A One Meniscus Pressure Condition Occurs in a Vertical Pore Configuration with one Meniscus.

The capillary pressure difference for one nanopore is derived as follows:

$$\mathcal{P}_1^* = \mathcal{P}_1 - \frac{2\sigma cos\theta}{r} \tag{56}$$

$$\mathcal{P}_2^* = \mathcal{P}_2 - \frac{2\sigma cos\theta}{r} \tag{57}$$

where $\mathcal{P}_1^*$ and $\mathcal{P}_2^*$, are the pressure at each side of the liquid interface, and *r* is the radius of the cylindrical capillary. By substituting Kelvin Equation into Equations (56) and (57):

$$\mathcal{P}_1^* = \mathcal{P}_1 + \left(\frac{\rho RT}{M}\right) \ln\left(\frac{\mathcal{P}_1}{P_0}\right) \tag{58}$$

$$\mathcal{P}_2^* = \mathcal{P}_2 + \left(\frac{\rho RT}{M}\right) \ln\left(\frac{\mathcal{P}_2}{P_0}\right) \tag{59}$$

As a results, $\Delta\mathcal{P}$ will be:

$$\Delta\mathcal{P}_c = \mathcal{P}_1^* - \mathcal{P}_2^* = (\mathcal{P}_1 - \mathcal{P}_2) + \left(\frac{\rho RT}{M}\right) \ln\left(\frac{\mathcal{P}_1}{P_2}\right) \tag{60}$$

where

$$\ln\left(\frac{\mathcal{P}_1}{P_2}\right) = \ln\left(\frac{\mathcal{P}_1/\mathcal{P}_m}{P_2/\mathcal{P}_m}\right) = \ln\left(\frac{1+(\mathcal{P}_1-\mathcal{P}_m)/\mathcal{P}_m}{1+(\mathcal{P}_2-\mathcal{P}_m)/\mathcal{P}_m}\right) = \ln(1 + (\mathcal{P}_1 - \mathcal{P}_m)/\mathcal{P}_m) - \ln(1 + (\mathcal{P}_2 - \mathcal{P}_m)/\mathcal{P}_m) \tag{61}$$

Applying the truncated Taylor series for logarithm to the right side of Equation (61):

$$\ln(1 + (\mathcal{P}_1 - \mathcal{P}_m)/\mathcal{P}_m) - \ln(1 + (\mathcal{P}_2 - \mathcal{P}_m)/\mathcal{P}_m) = \left((\mathcal{P}_1 - \mathcal{P}_m)/\mathcal{P}_m\right) - \left((\mathcal{P}_2 - \mathcal{P}_m)/\mathcal{P}_m\right) = (\mathcal{P}_1 - \mathcal{P}_2)/\mathcal{P}_m \tag{62}$$

$$\Delta \mathcal{P}_c = \mathcal{P}_1^* - \mathcal{P}_2^* = (\mathcal{P}_1 - \mathcal{P}_2) + \left(\frac{\rho RT}{M}\right)\frac{(\mathcal{P}_1 - \mathcal{P}_2)}{\mathcal{P}_m} \quad (63)$$

where $\mathcal{P}_m = \frac{(\mathcal{P}_1 + \mathcal{P}_2)}{2}$ is the average pressure on both sides of the porous layer.

The transport of a liquid in a porous material, Equation (54), due to capillary condensation can be rewrite in the form:

$$\varphi_{cap} = \left(\frac{D_{cap}\varepsilon}{x}\right)\frac{(\mathcal{P}_1 - \mathcal{P}_2)}{RT} \quad (64)$$

where $D_{cap}$is the coefficient of the diffusion flux in the liquid-filled side, and is given as:

$$D_{cap} = \frac{\rho_l RT}{\tau M}\left(\frac{r^2}{8\mu_l}\right)\left[1 + \frac{\rho_l RT}{P_m}\right] \quad (65)$$

where ρ_l and μ_l are the density and viscosity of the condensed liquid, *T* is temperature, *r* is the pore size, and *R* is the gas constant, *M* is the molecular weight.

2.2.3. Mixed condensation model

The mixed condensation proposed by Soleimanikutanaei et al. [10, 11], which is based on the linear addition of the wall condensation and capillary condensation in the membrane, can be written as:

$$\dot{\varphi}_{cond} = \frac{(T_{max} - T_{wall})}{(T_{max} - T_{min})}\,\dot{\varphi}_{WC} + \dot{\varphi}_{cap} \quad (66)$$

where T_{max}, T_{min}, and T_{wall} are the maximum, minimum, and wall temperature, respectively. The $\dot{\varphi}_{WC}$ and $\dot{\varphi}_{cap}$ are condensation on the solid wall and the capillary condensation, respectively, and are given as:

$$\dot{\varphi}_{WC} = \theta_b \left(\frac{1}{\dot{Y}_v - 1}\right) \rho \, D_{v,m} \frac{\partial \dot{Y}_v}{\partial n} \frac{A_{cell-wall}}{V_{cell}} \tag{67}$$

$$\dot{\varphi}_{cap} = A \frac{\rho_l \varepsilon \, r^2 \Delta \text{ƥ}}{\Gamma M 8 \, \mu_l x} \tag{68}$$

where,

$$\Delta \text{ƥ} = (p_1 - p_2)\left(1 + \rho RT/(M p_m)\right) \tag{69}$$

The mixed model has been proved as an efficient model that can simulate the transport of the water vapor and heat from the flue-gas zone to the porous zone and from there to the cooling water zone in a TMC heat exchanger.

The condensation rate was adjusted based on the previously published experimental data from the GTI [28] and by the correction factors, C_{f1} and C_{f2}.

$$\dot{\varphi}_{cond} = \frac{(T_{max} - T_{wall})}{(T_{max} - T_{min})} C_{f1} \dot{\varphi}_{WC} + C_{f2} \dot{\varphi}_{cap} \tag{70}$$

The condensation model was applied to the shadow cells of the membrane tube via the UDFs. The condensation rate on a solid wall is implemented as a sink term in the continuity Equation of the cells next to the cold wall. The source terms in the mass, species and energy Equation were implemented to perform the heat and water transfer from the flue-gas along the porous tube wall. The species source is employed in the liquid water transport Equation

on the porous wall side, and the species sink term is employed in the water vapor transport Equation on the flue-gas zone. Also, the energy source has been applied to the flue gas and porous wall side. The effective thermal conductivity of the nanoporous membrane [17] was calculated by:

$$\lambda_{eff} = \varepsilon\lambda_{fg} + (1-\varepsilon)\lambda_{solid} \tag{71}$$

where λ_{fg} is the flue gas thermal conductivity and λ_{solid} is the solid thermal conductivity.

2.3. Numerical Data Analysis

2.3.1. Heat transfer analysis

In the present numerical study, the Reynolds number, $\mathrm{Re}_{D,max}$, was evaluated at the maximum velocity of the flue gas, $V_{max,fg}$, and it was in the range of 170 to 8900. So, the effect of the laminar and turbulent flow was considered during the simulation. The $\mathrm{Re}_{D,max}$ is given as:

$$Re_{D,max} = \frac{\rho V_{max,fg} d_o}{\mu}, \quad V_{max} = \frac{S_T}{S_T - d_{out}} V_{fg,i} \tag{72}$$

where d_o and $V_{fg,i}$ are the outer nanoporous tube diameter and inlet flue gas velocity, respectively, and S_T is transverse pitch.

The average convection Nusselt number, $\overline{Nu}_{conv}$, and overall convective Nusselt number, $Overall\ Nu_{conv}$, were evaluated from sensible heat transfer and calculated by the following relations:

$$\overline{Nu}_{conv} = \frac{h_s d_o}{\lambda_{fg}} \tag{73}$$

$$h_s = \frac{Q_s}{(\bar{T}_{fg} - T_e) n \pi d_o L} \tag{74}$$

$$Overall\ Nu_{conv} = n * \overline{Nu}_{conv} \tag{75}$$

where n is the number of tubes, L is the tube length, $\bar{T}_{fg}$ is the average flue gas temperature, T_e flue gas exit temperature, λ_{fg} is the flue gas thermal conductivity [W/m], and Q_s is the sensible heat transfer through the tube bundle [20] and is defined as:

$$Q_s = \left(\dot{m}_{fg,i} - \dot{\varphi}_{cond}\right) C_{p,fg} \left(T_{fg,i} - T_{fg,e}\right) - \dot{\varphi}_{cond} C_{p,v} \left(T_{fg,i} - T_w\right) \tag{76}$$

where $T_{fg,i}$ is the inlet flue gas temperature, and $C_{p,v}$ and $C_{p,fg}$ are the vapor and flue gas heat capacity at constant pressure [J/kg.s], respectively.

The inlet mass flow rates, $\dot{m}_{fg,i}$, of the flue gas were calculated based on the flue gas properties, velocity, and surface area of the tube inlet. The condensation-convection Nusselt number $Nu_{cond-conv}$ was calculated to evaluate the Nusselt number for sensible heat transfer and latent heat transfer, due to simultaneous condensation of water vapor, and is given as:

$$Nu_{cond-conv} = \frac{h_s^* d_o}{k_{fg}} \tag{77}$$

$$h_s^* = \frac{\left(\dot{m}_{fg} - \dot{\varphi}_{cond}\right) C_{p,\mathrm{fg}} \left(T_{fg,i} - T_{fg,\mathrm{e}}\right)}{(\bar{T}_{fg} - T_e) \pi d_o L} \tag{78}$$

$$h_{cap} = \frac{C_{f2}\dot{m}_{cap}C_{p,\mathrm{v}}\left(T_{fg,i}-T_{fg,\mathrm{e}}\right)}{\left(\bar{T}_{fg}-T_w\right)\pi d_o L} \tag{79}$$

$$h_{wall} = \frac{C_{f1}\frac{\left(T_{max}-T_{wall}\right)}{\left(T_{max}-T_{min}\right)}\dot{m}_{Wall}\,C_{p,\mathrm{v}}\left(T_{fg,i}-T_{fg,\mathrm{e}}\right)}{\left(\bar{T}_{fg}-T_w\right)\pi d_o L} \tag{80}$$

2.3.2. Hydraulic resistance analysis

The Euler number, Eu, is defined as:

$$Eu = \frac{\Delta p}{\rho V_{max,fg}^2} \tag{81}$$

where Δp is the pressure drop across the tube bundle. The friction factor is defined as [108]:

$$f = \frac{\Delta p}{n}\frac{D_h}{d_o}\frac{2}{\rho V_{max,fg}^2} \tag{82}$$

where, D_h is the hydraulic diameter and is given as:

$$D_h = \frac{4\times(Net\ Free\ Volume)}{Friction\ surface} = \frac{4S_T S_L}{\pi d_o} - d_o \tag{83}$$

where S_L and S_T are the longitudinal pitch and transverse pitch, respectively.

2.4. Description of TMC-Based Heat Exchanger Model and Related Experiment

2.4.1. TMC experimental description

The experimental setup and results performed and previously published by the GTI [28] were adopted for the current research. Figure 11 represents the experimental staggered

nanoporous ceramic membrane (TMC) tube bundle. The tubes were protected by metal plates from both sides to reinforce the strength of the module structure. The TMC tube bundle was used for the lab scale experimental setup to recover the sensible heat and water vapor as well as its latent heat from the flue gas. The TMC tube bundle consisted of 78 nanoporous ceramic tubes of 431.8 mm in length and was arranged in staggered configurations.

Figure 12 represents the schematic diagram of the lab scale experimental setup and the equipment used to run the TMC heat exchanger by the GTI laboratory [28]. The experimental test rig consisted of TMC heat exchanger, and measurement instruments/ regulators for temperature, pressure, humidity, and flow rate. They measured the condensation rate by calculating the difference between the outlet and inlet conditions of flue-gas passes across the TMC module. The TMC heat exchanger was installed horizontally, and the flue gas flowed vertically from the bottom side to the upper side through the TMC tube bundle. The physical properties of the TMC tubes are presented in Table 3 and experimental results are represented in Table 4. A more detailed description of the experimental setup can be found in [28].

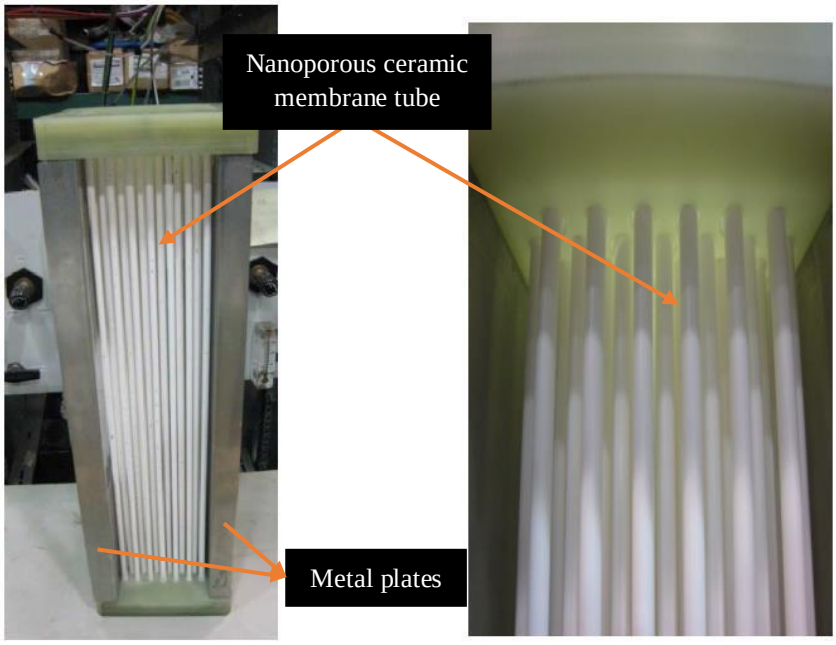

Figure 11. TMC Staggered Tube Bundle Used for GTI Experimental Setup [28].

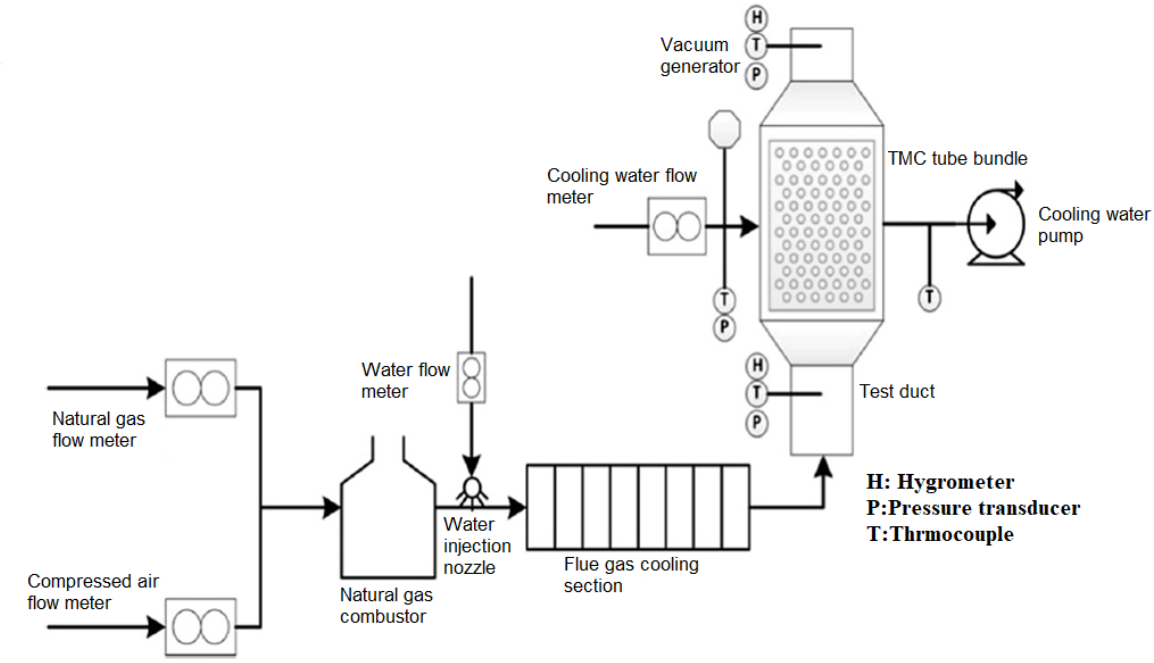

Figure 12. Schematic Diagram of TMC Experimental Setup [16].

Table 3. Physical Properties of the TMC Tubes

Tube material	Nanoporous ceramic membrane
Porosity	0.2
Density, kg/m^3	3790
Thermal conductivity of solid material, W/m.K	30
Average pore size diameter, μm	4
Heat capacity, J/K.kg	30
Tube length, mm	431.8
Inside tube diameter, mm	3.51
Outside tube diameter, mm	5.49

Table 4. Inlet and Outlet Conditions of the Experimental Results [28].

Case number	**$T_{w,in}$ [K]**	**$V_{w,in}$ [m/s]**	**$T_{fg,in}$ [K]**	**$V_{fg,in}$ [m/s]**	**$T_{w,out}$ [K]**	**$T_{fg,out}$ [K]**	**$\dot{m}_{cond}$ [kg/hr]**
1	316.4	0.028	345.0	0.511	321.8	324.5	0.72
2	305.0	0.029	354.8	0.526	324.3	327.2	1.45
3	293.9	0.017	355.2	0.526	327.2	323.2	1.46
4	315.7	0.027	355.6	0.525	328.3	329.9	1.48
5	304.8	0.028	344.8	0.512	325.2	325.9	1.66
6	305.3	0.043	355.9	0.526	318.4	322.8	1.87
7	294.4	0.028	355.3	0.526	322.4	324.5	2.23
8	305.3	0.085	355.5	0.527	316.3	324.1	2.42
9	293.3	0.041	354.9	0.527	318.4	321.4	3.06
10	293.9	0.088	354.5	0.524	308.4	318.3	3.67

where $T_{w,in}$, $V_{w,in}$, $T_{fg,in}$, $V_{fg,in}$, $T_{w,out}$, and $T_{fg,out}$ are the inlet water temperature, inlet cooling water velocity, inlet flue gas temperature, inlet flue gas temperature, outlet water

temperature, and outlet flue gas temperature, respectively. The inlet and outlet temperature were measured at the inlet and exit of the TMC module. The $\dot{m}_{cond}$ is the condensation rate which was calculated based on the water vapor mass fraction difference of the water vapor content between the flue gas inlet and outlet.

2.4.2. Numerical Model Description of the TMC-Based Heat Exchanger

Geometry

The TMC tube bundle geometry and configuration adopted in the current study are similar to the GTI [29] lab scale model. The geometry was generated using the design modeler Ansys/Fluent 2021. The TMC model is in a staggered configuration and consists of 78 nanoporous ceramic tubes arranged in 12 rows, as shown in Figure 13. To reduce the simulation time and cost, only one-half of the geometry has been simulated with the symmetry boundary shown on the right side of Figure 13. The tube wall is made of ceramic nonporous material. The geometry is divided into three main domains: the flue gas domain, the porous domain, and the water domain. This model replicates the experimental model and conditions of GTI [28].

The transport membrane condenser model comprises a number of rows, with a total number of tubes of N_R, arranged in a staggered configuration and surrounded by flue gas. The first row contains 7 tubes and the second row 6 tubes. The basic model consists of 78 nanoporous membrane tubes. However, in Chapter 4 the number of rows will be varied: the first and second rows were duplicated at each step to increase the N_R from 2 to 24, with the same dimensions and specifications. The design modeler of ANSYS software was used

to generate geometry. The corresponding characteristic dimensions represented in Table 5 were used for the numerical simulations unless it is stated otherwise.

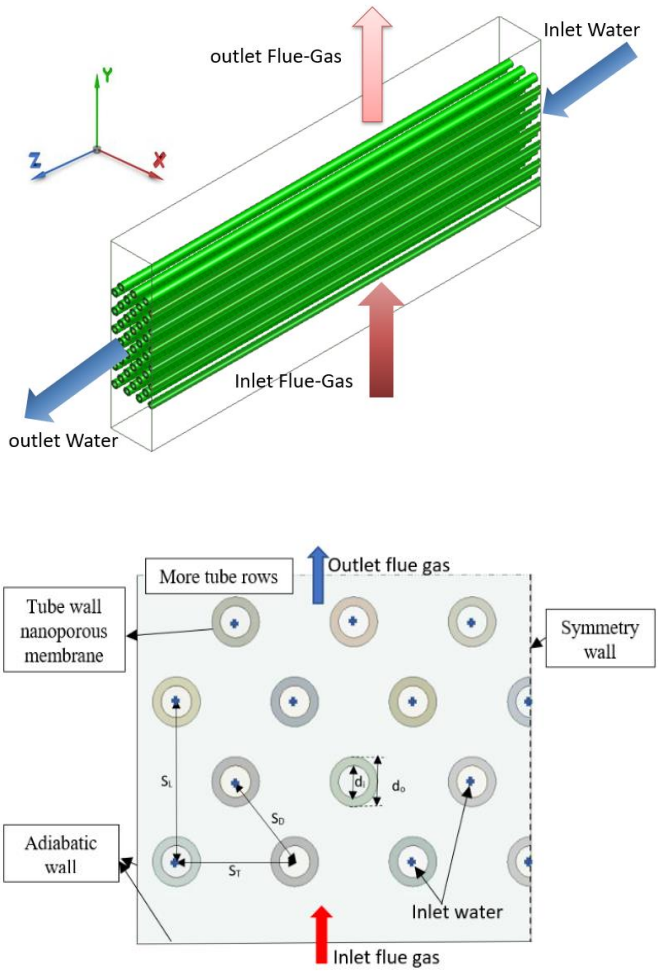

Figure 13. TMC Staggered Tube Bundle Geometry and boundary Conditions.

The flue gas flows outside the nanoporous ceramic tubes from the bottom to the top side of the TMC staggered bundle, while the cooling water flows horizontally inside the tubes. The condensation of the water vapor occurred at the outer surface of the tube and through the

pores. The non-condensable gases were prevented from transferring to the other side of the membrane once the membrane pores were filled up with condensate water. The transported water joins the cooling water with its latent heat and sensible heat.

Table 5: Dimension of the TMC Staggered Tube Bundle

Geometrical parameters	
Number of tubes	78
Outside diameter, d_o (mm)	5.49
Inside diameter, d_i (mm)	3.51
Longitudinal pitch, S_L (mm)	8.79
Transverse pitch, S_T (mm)	13.61
Tube Length, *L* (mm)	431.8

The tube wall is made of ceramic nonporous material that is responsible for transporting the water vapor from the flue gas side to the water side. The water vapor condenses at the outer surface of the tube wall and transports it to the other side through the nanoporous material. The recovered water is carried away with cooling water as fresh water. The cooling water becomes warmer as it flows from its inlet to the outlet as a result of absorbing latent heat because of condensation and sensible heat due to temperature differences. The flue gas temperature and moisture content will reduce as it flows from the inlet to the outlet. The water vapor from the flue gas releases the latent heat as a result of the condensation at the surface of the nanoporous ceramic membrane. The membrane condensers allow the condensed water to permeate through the membrane sideways along with heat transfer.

Numerical computational mesh

The mesh was prepared using the meshing tools of Ansys/workbench with hexahedral elements, Figure 14. The multi-block hybrid 3D computational mesh was used to tackle the geometry complexity and the computational efficiency and cost at the same time, with hexahedral elements. The solution sensitivity to the mesh quality was performed by increasing the mesh size from 0.7 million to 3.05 million cells.

The results of the grid independence study are presented in Figure 15 for the tube diameter of 5.486 mm, with the boundary conditions listed in Table 6. As seen, the outlet flue gas temperature and condensation rate are almost the same as the mesh size or the number of the control volumes is increased from 2.34 to 3.05 million, which indicates that a mesh size of 2.34 M is suitable for the TMC-based heat exchanger simulation. Similar mesh-type and sizing were used to generate the mesh for other tube bundles with different tube diameter geometry.

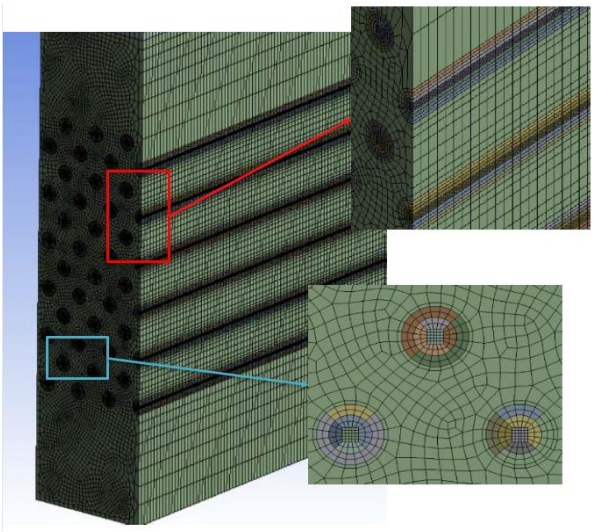

Figure 14. Computational Mesh for TMC Tube Bundle.

Table 6: Boundary Conditions Used for Mesh Independence Study.

Boundary conditions		Inlet flue gas mass fraction	
Water inlet velocity, m/s	0.027	H_2O	11.4%
Water inlet temperature, K	298	O_2	4%
Flue gas inlet velocity, m/s	0.526	CO_2	9%
Inlet flue gas temperature, K	355	N_2	75.6%

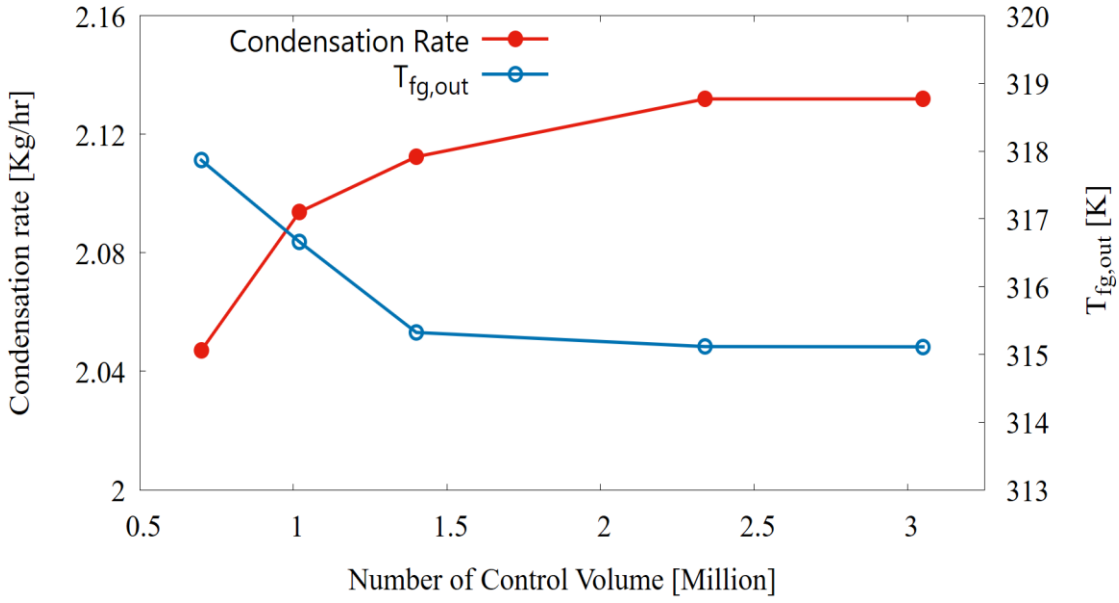

Figure 15. Grid Independence Study.

2.4.2.1. Solver settings and boundary conditions

Ansys/Fluent 2019 R1 CFD code with the Finite Volume Method (FVM) was used to model the flow inside the TMC-based heat exchanger. A double precision pressure-based solution method was considered in this study. In all the numerical simulations of single-phase numerical modeling, the Equations were solved using the following numerical schemes unless it is stated otherwise:

- The Coupled algorithm was used to couple the pressure and velocity.
- The Least Squares Cell-Based method was used for gradient spatial discretization.
- The Presto scheme was used for pressure discretization.
- The Second Order scheme is used for momentum, species transport, and energy Equations discretization.

The solution was obtained under steady-state conditions. The convergence criteria were set to 10^{-6} for all the governing Equations. The Reynolds Averaged Navier-Stokes (RANS) Equations were used to describe fluid dynamics. In addition, to monitor residual convergence in all calculations, the area-weighted average of the outlet water temperature, outlet flue gas temperature, and condensation rate were monitored during the simulation to ensure solution convergence.

The inlet conditions, for both flue gas and water, were set as velocity inlets to target the effects of the Reynolds number in the heat and mass transfer inside the TMC. The boundary conditions are represented in Figure 13.

2.5. Flue Gas Thermodynamics Properties

The mixture thermodynamics properties were calculated based on each species' mass fraction and its thermodynamics properties. The thermodynamic properties of the non-condensable species were obtained from the NIST database [109] and were implemented in the Fluent solver.

The point-piecewise linear function was used to correlate the properties at different flue gas temperatures. The experimental temperature was in the range of 293.15 to 366.4 (K)

which are the minimum cooling water inlet temperatures and maximum flue-gas inlet temperature. Figure 17 represents five points function for each property for non-condensable gases, CO_2, NO_2, and O_2. The liquid water and water vapor properties were defined using the Equations in Table 7. For the water vapor, the thermodynamic properties available in the fluent solver also meet the criteria of the current work and were used during the simulation [110].

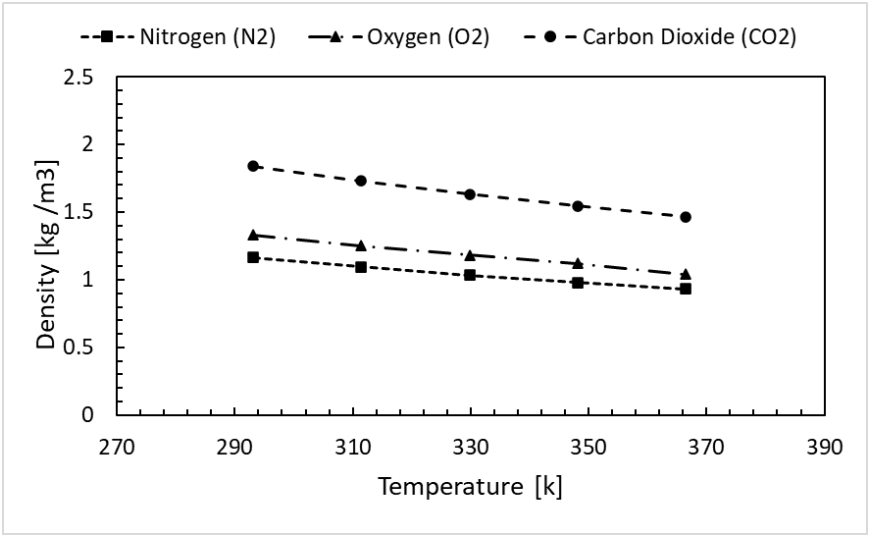

a)

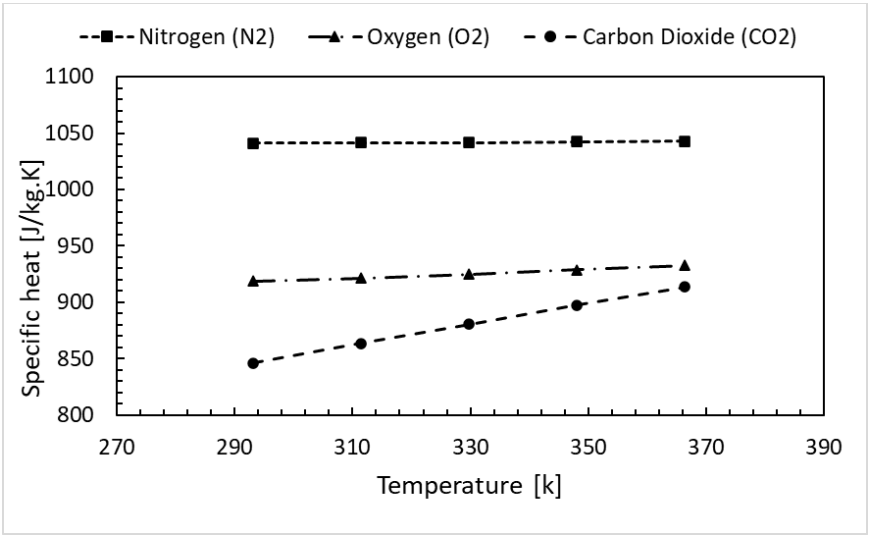

b)

Figure 16. Thermodynamic Properties of Flue Gas Non-Condensable Species N_2, O_2, and CO_2. (a) Density , (b) Specific heat, (c) Thermal Conductivity, and (d) Dynamic Viscosity.

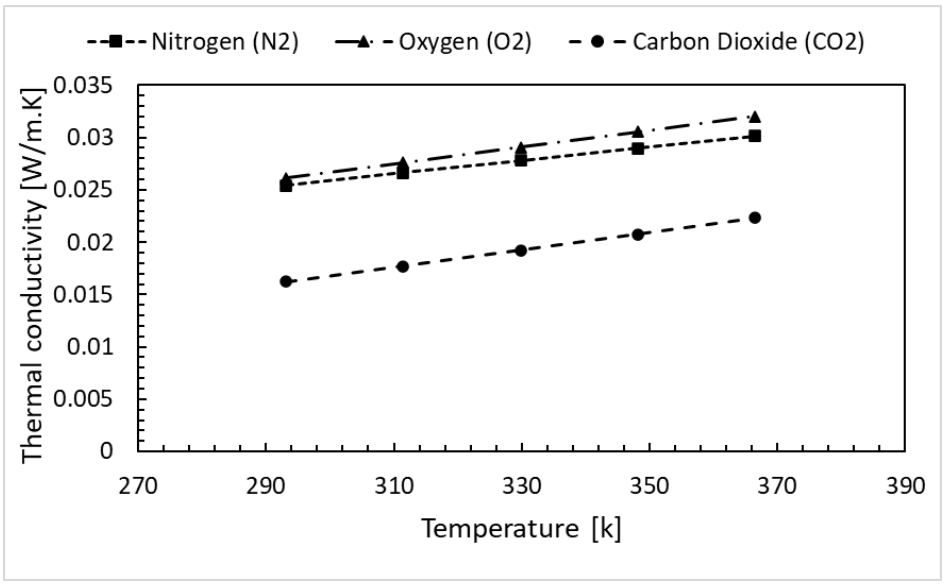

c)

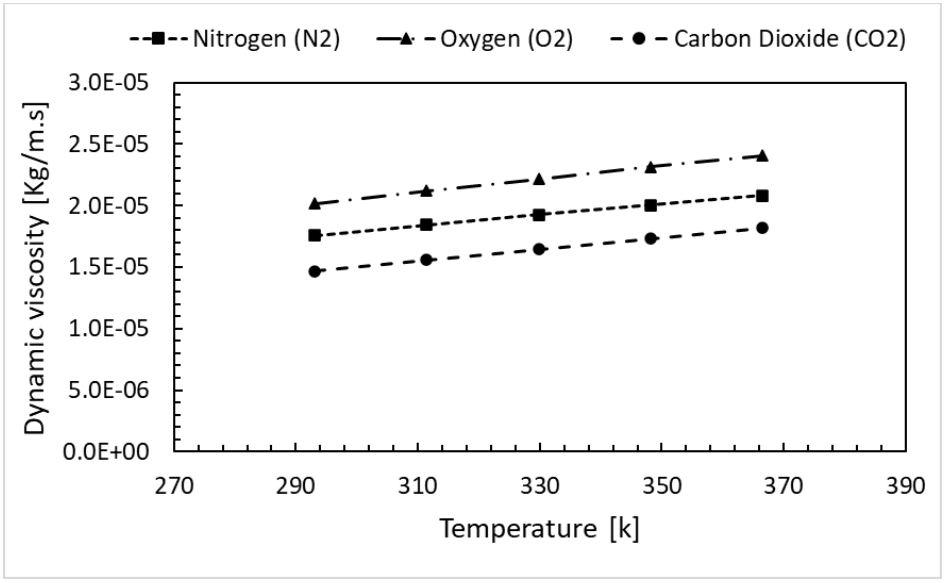

d)

Figure 16 (continued). Thermodynamic Properties of Flue Gas Non-Condensable Species N_2, O_2, and CO_2. (a) Density , (b) Specific heat, (c) Thermal Conductivity, and (d) Dynamic Viscosity.

Table 7: Thermodynamic properties of water vapor and water liquid for temperature ranges 0 °C to 288 °C [109]:

property	Water vapor	Water liquid
Specific heat [J/K. kg]	$c_p = 1.8653 + 1.0881 \times 10^{-5}T + 4.4902 \times 10^{-6}T^2 + 1.0183 \times 10^{-7}T^3$	$c_p = \exp(1.4423 - 8.4025 \times 10^{-4}\mathrm{T} + 1.41 \times 10^{-5}T^2 - 7.3846 \times 10^{-8}T^3 + 1.4856 \times 10^{-10}T^4)$
Dynamic viscosity [Kg/m.s]	$\mu = 10^{-6} \times (9.1445 + 0.029257T + 1.9067 \times 10^{-7}\ T^2)$	$\mu = \exp(-6.3933 - 0.026299\mathrm{T} + 9.7341 \times 10^{-4}T^2 - 1.3986 \times 10^{-7}T^3)$
Thermal conductivity [W/m. K]	$k = 0.017071 + 5.3167 \times 10^{-5}T + 2.322 \times 10^{-7}\ T^2 + 3.8962 \times 10^{-10}\ T^3$	$k = 0.56611 + 0.002048T - 1.0205 \times 10^{-5}\ T^2 + 1.1897 \times 10^{-8}\ T^4$
Density [Kg/m^3]		$\rho = 1002.6 - 0.2177T - 0.0020099T^2 - 1.6478 \times 10^{-6}\ T^3$

2.6. Numerical model assumptions and simplification:

The following assumptions were considered during the numerical modeling:

- Steady-state simulation.
- The condensation rate is governed by the rate of diffusion of condensable gases toward the cold surface and capillary pressure inside the pores.
- Based on Kelvin Equation, the capillary condensation in nano-pores occurs when the condensing species partial pressure is lower than its vapor pressure.
- The source terms were added to the basic Equations and species transport Equation applied to the cells adjacent to the wall (shadow) in the porous zone, and the source terms were added to consider the species transport from the flue gas to the porous media.

- Since the simulation is based on condensate the water vapor of flue gas, the species source was added to the liquid water transport Equation and the species sink term was applied to the water vapor Equation in the flue gas domain.
- Capillary condensation (Kelvin Equation) ignores the effect of statistical film thickness (condensation film).
- The model cannot capture the hysteresis caused by the condensation. Since the radius of the cylindrical capillary (r) is considered constant in Equation (53).
- The effect of the nanoporous membrane (irregular) geometrical configuration on the water transport is included by defining the tortuosity of the porous layer in the Mixed condensation model.
- The nanoporous layers are assumed to be a regular shape.
- The condensation rate was adjusted based on the previously published experimental data.

2.7. Numerical Model Validation

In order to verify the validity of the present numerical results, the values of the condensation rate, outlet flue gas, and outlet water temperature were compared with the experimental data published by [28]. The wall-based condensation model and the mixed condensation model were tested and compared. The operating conditions during the simulation were set similarly to the experimental operating conditions. The condensation model has been applied to the numerical simulation by using the user-defined function in the Fluent software. Table 4 shows the operating condition for the model validation.

Figure 17 compares the condensation rate between the numerical model and the experimental results, with generally a good agreement between the two results. The error of the predicted condensation rate is less than 13% except for one case of about 25%. The errors associated with the outlet flue gas temperature (Figure 17b) and outlet water temperature (Figure 17c) were less than 4% and 6%, respectively. As seen, the numerical model can predict the condensation rate and heat transfer inside the TMC heat exchanger with good accuracy.

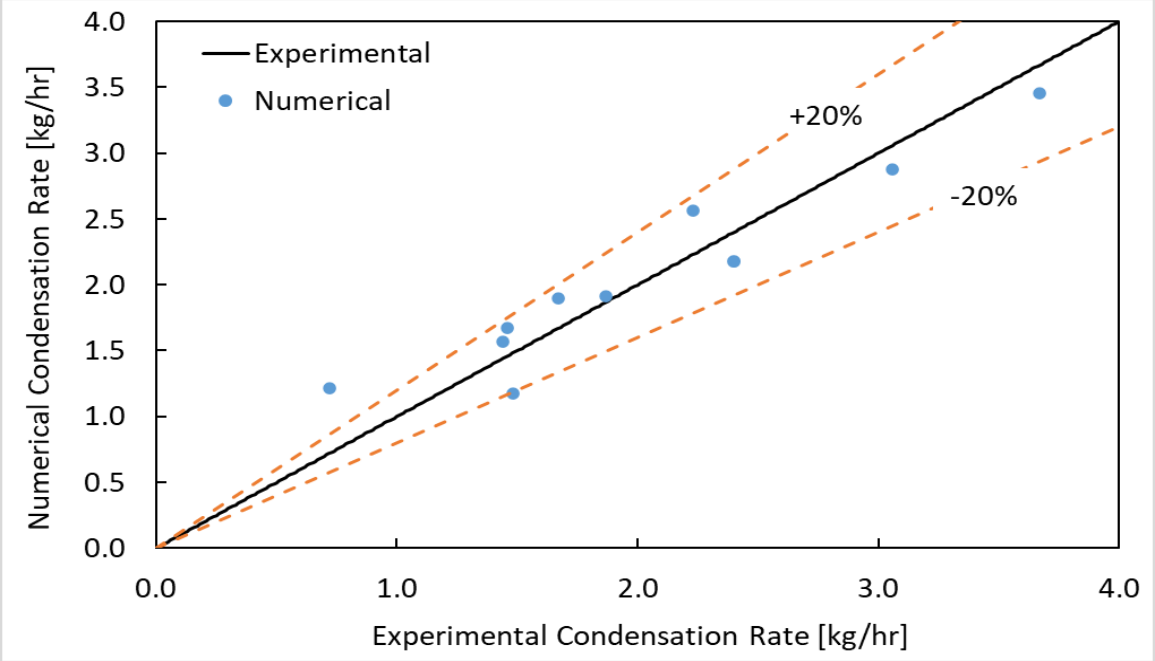

(a) Condensation rate based mixed model

Figure 17. Numerical validation of the TMC staggered tube bundle.

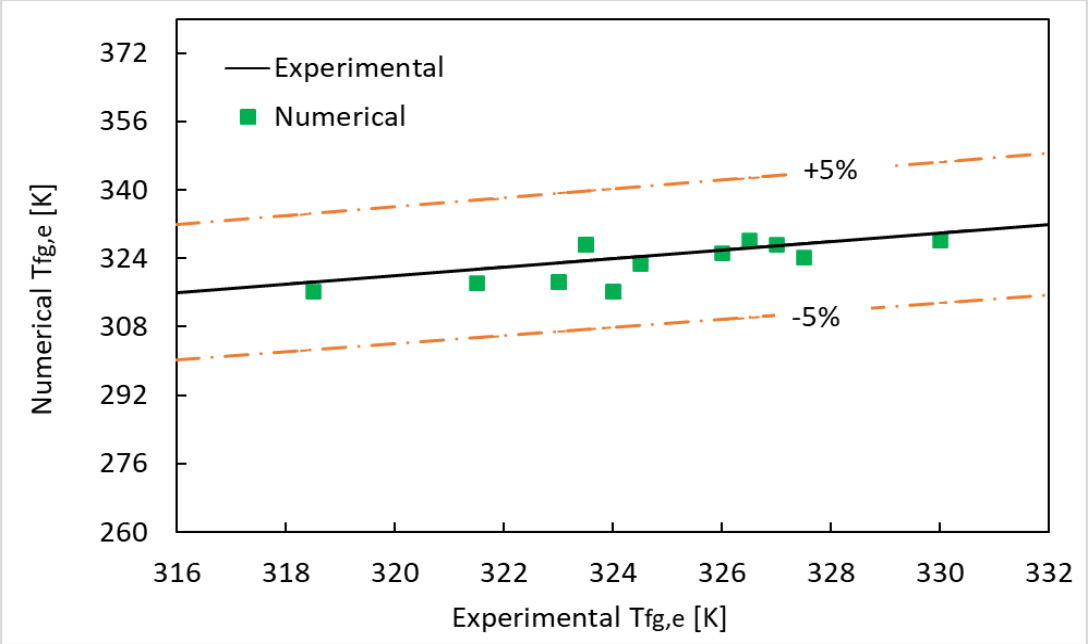

(b) Outlet flue gas temperature

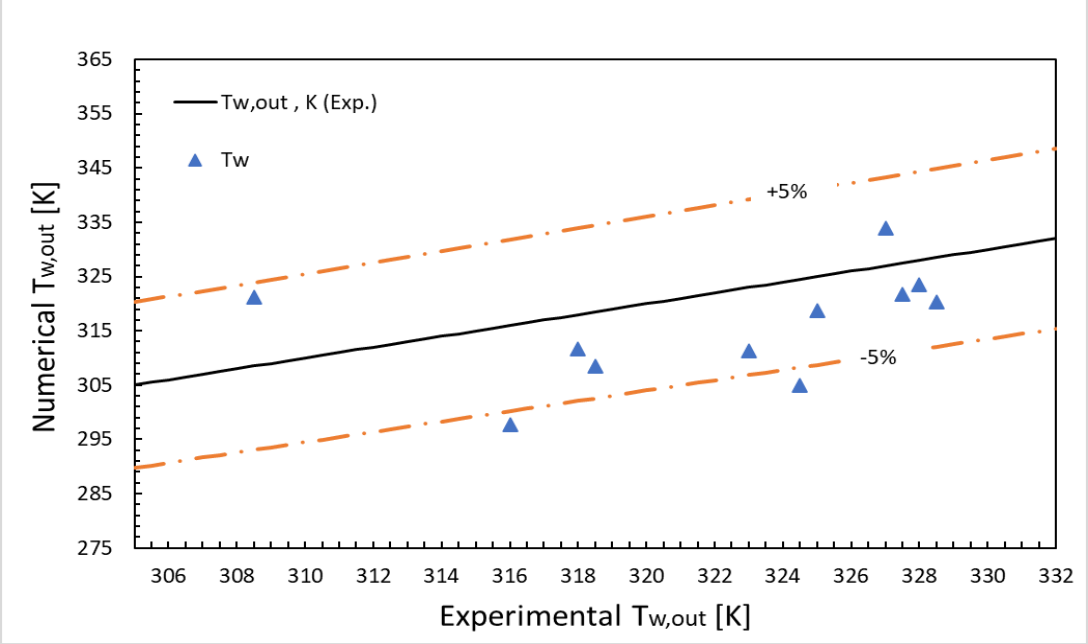

(c) Outlet water temperature

Figure 17 (continued). Numerical validation of the TMC staggered tube bundle.

3. CHAPTER III: SINGLE PHASE MODELING OF TMC USING FICK'S DIFFUSION LAW

In this Chapter, a condensation model based on Fick's diffusion law in the membrane tube [4, 8] has been used to model the membrane's heat and mass transfer processes. This model is capable to simulate the transport of the water vapor and heat from the flue-gas zone to the porous zone and from there to the cooling water zone in a TMC heat exchanger. Transport of the water vapor and other species among those three zones is modelled using appropriate User Defined Functions (UDFs) in the computational fluid dynamic code ANSYS Fluent. The effects of the membrane properties and geometrical parameters, such as tube diameter and thickness, and different operating conditions (inlet water temperature and flow rate as well as inlet flue gas temperature and flow rate) on the condensation rate and thermal outlet conditions will be investigated and discussed. Table 8 represents the boundary conditions used in the simulation.

Table 8. Boundary conditions

Working fluids Inlet Conditions		Inlet flue gas mass fraction	
Water inlet velocity, m/s	0.027	H_2O	11.4 %
Water inlet temperature, K	290-308	O_2	4 %
Flue gas inlet velocity, m/s	0.526	N_2	75.6 %
Inlet flue gas temperature, K	355	CO_2	9 %

3.1. Effect of membrane tube diameters

The effect of the inlet water temperature on the condensation rate and outlet temperature of the flue gas for different tube outer diameters (d_o), different tube internal diameters (d_i), and membrane porosity is studied numerically for a cross-flow TMC heat exchanger. To study the effect of tube diameter, the inlet temperature of the flue gas, the inlet velocity of the water, and the flue gas are fixed during the simulation. Also, the geometrical parameters, including tube length and longitudinal and transversal pitches, have been set to L= 431.8 mm, S_l = 17.57 mm, and S_t = 6.81 mm, respectively. The study of the tube diameter is divided into two cases: in the first case, d_i is fixed while d_o is varied; in the second case, d_o is fixed while d_i is varied.

Figures 18a and 18b represent the effect of the inlet water temperature on the condensation rate and outlet flue gas temperature, respectively, for different outer tube diameters. As seen in the Figures, an increase in the inlet water temperature reduces the condensation rate significantly (Figure 18a) and increases the outlet temperature of the flue gas linearly (Figure 18b), because of the reduction in the temperature difference across the TMC tube as the cooling water temperature increase, which reduce the heat transfer and condensation rate as well. The variation of the tube outlet diameter also shows an effect on the condensation rate and flue gas outlet temperature; increasing the tube outer diameter by 38% increases the condensation rate, less than 5%, and reduces the flue gas outlet temperature slightly, about 1%. The reduction in the outlet flue gas means more heat transfer occurred across the TMC exchanger.

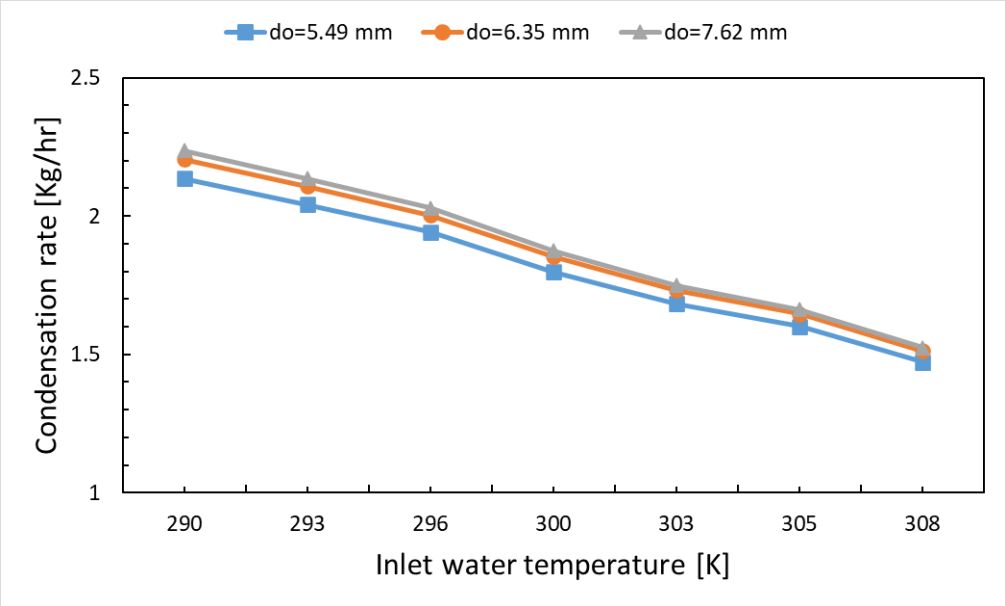

(a) Condensation Rate

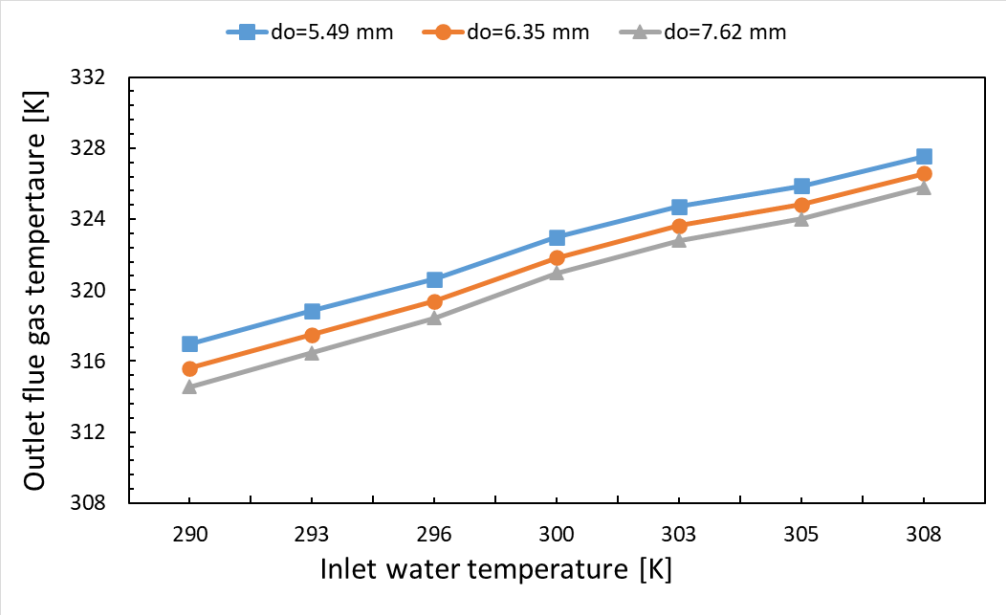

(b) Outlet Flue Gas Temperature

Figure 18. Effect of the Outlet Tube Diameter at Different Inlet Water Temperature at Different Inlet Water Temperature, Porosity= 0.20, di=3.51 mm.

The variation of the outer tube diameter changes the tube spacing in the staggered tube bundle. As a result, an increase in the outer tube diameter decreases the tube spacing and

increase the tube surface area available for condensation and heat transfer, which enhances the flue gas turbulence inside the tube bundle, resulting in an enhancement in the heat transfer and the condensation rate.

Figures 19a and 19b represent the effect of the inlet water temperature on the condensation rate and outlet flue gas temperature, respectively, for different inlet tube diameters. The variation of the inlet temperature showed more effect on the condensation rate and heat transfer as compared to the other studied parameters. As the water temperature increased from 290 to 308, about 6%, the condensation rate decreased by about 30% and 34%, and the outlet flue gas temperature increased by about 4% and 3%, for d_i=4.7 mm and d_i= 3.18 mm, respectively. This is due to the reduction in the temperature across the membrane tube wall. As shown, variation of the internal tube diameter also significantly effects on the condensation rate and flue gas outlet temperature; increasing the internal tube diameter by 38% results in an increases in the condensation rate, about 22% to 29%, and reduces the flue gas outlet temperature, over 2%. This is related to an increase in the amount of cooling water flowing inside the tube and to a reduction in the flow velocity as the inlet tube diameter increases, which decrease the flow residence time, increase the heat transfer between two sides of the membrane tube that reduce the flue gas temperature and enhance the condensation of water vapor from flue gas. It should be noted that the variation in internal tube diameter has a larger effect on the heat transfer and water vapor condensation than the outer tube diameter.

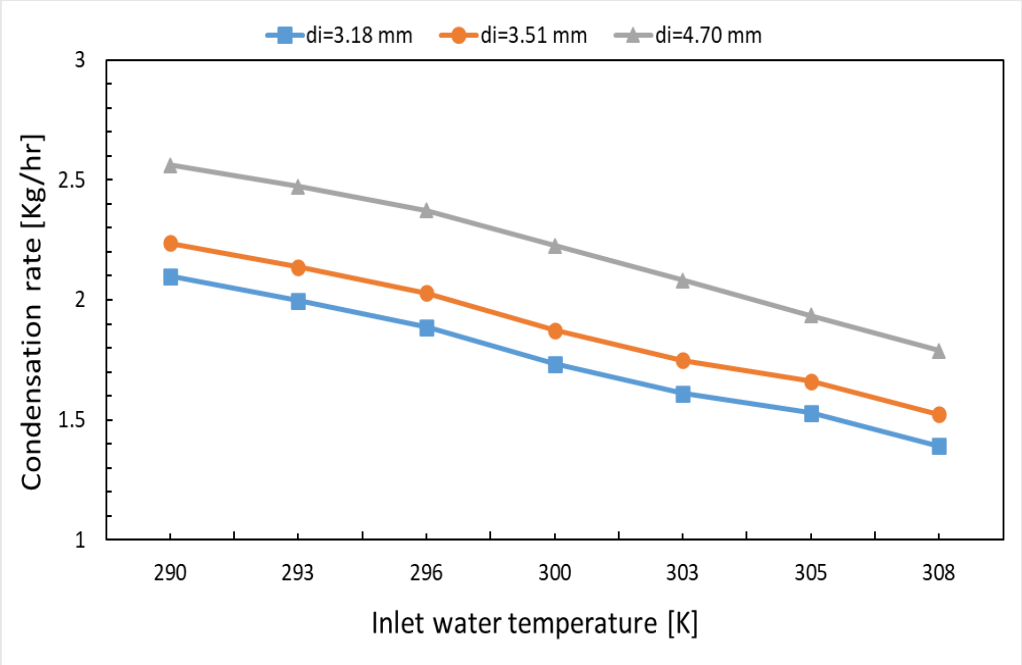

(a) Condensation Rate

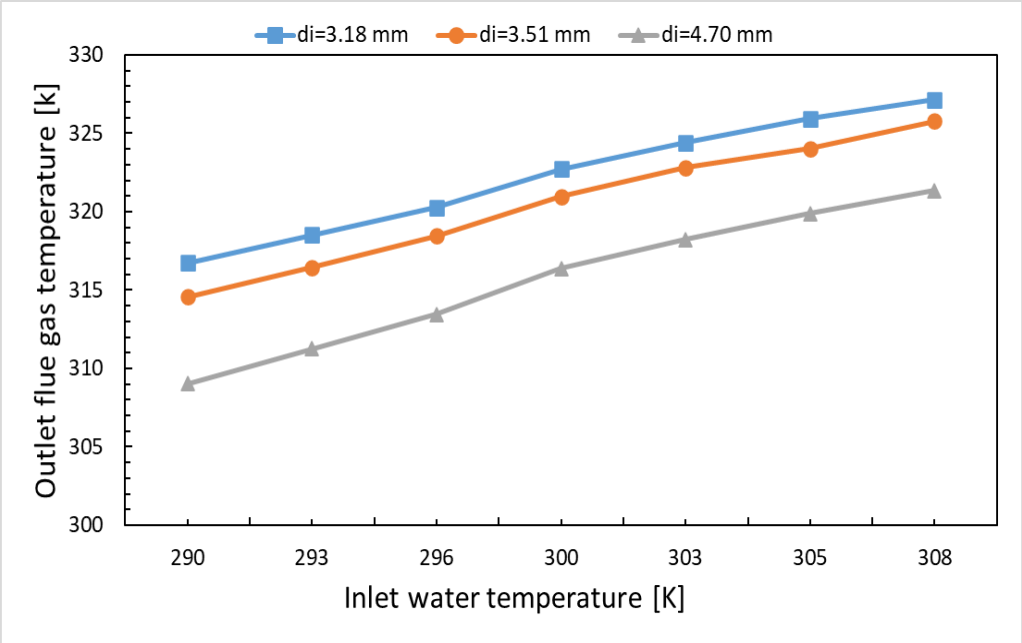

(b) Outlet Flue Gas Temperature

Figure 19. Effect of the Inlet Tube Diameter at Different Inlet Water Temperature, Porosity= 0.20, do=7.62 mm.

3.2. Effect of Membrane Porosity

Figure 20 represents the effect of membrane porosity on the condensation rate. As seen, increasing the membrane porosity from 0.2 to 0.4, which represents 100% of increase, reduces the condensation rate. The variation in the condensation rate was between 4.4% to 5.2%, for the range of the given inlet water temperature. However, 0.5 increase in the porosity at each step shows that the condensation rate becomes less sensitive to the variation in the porosity. For instance, increasing the porosity from 0.2 to 0.25 enhances the condensation rate by 1.5% for Tw= 293 K, as compared to increase the porosity from 0.35 to 0.4 that enhances the condensation rate by about 0.95%. The enhancement in the condensation rate with porosity is because of the linear relationship between the effective thermal conductivity of the porous material and its porosity, as the porosity ε increases, the effective thermal conductivity decreases. As shown by the relation for the effective thermal conductive λ_{eff} below:

$$\lambda_{eff} = \varepsilon\lambda_f + (1-\varepsilon)\lambda_s \tag{84}$$

where λ_f is the fluid thermal conductivity and λ_s is the solid thermal conductivity [17, 110].

A reduction in the effective thermal conductivity could reduce the heat transfer rate across the membrane. In addition, a higher porosity may reduce the capillary driving force potential, which may also reduce the water penetration rate through the membrane. Both factors mentioned above could contribute to the reduction in condensation rate.

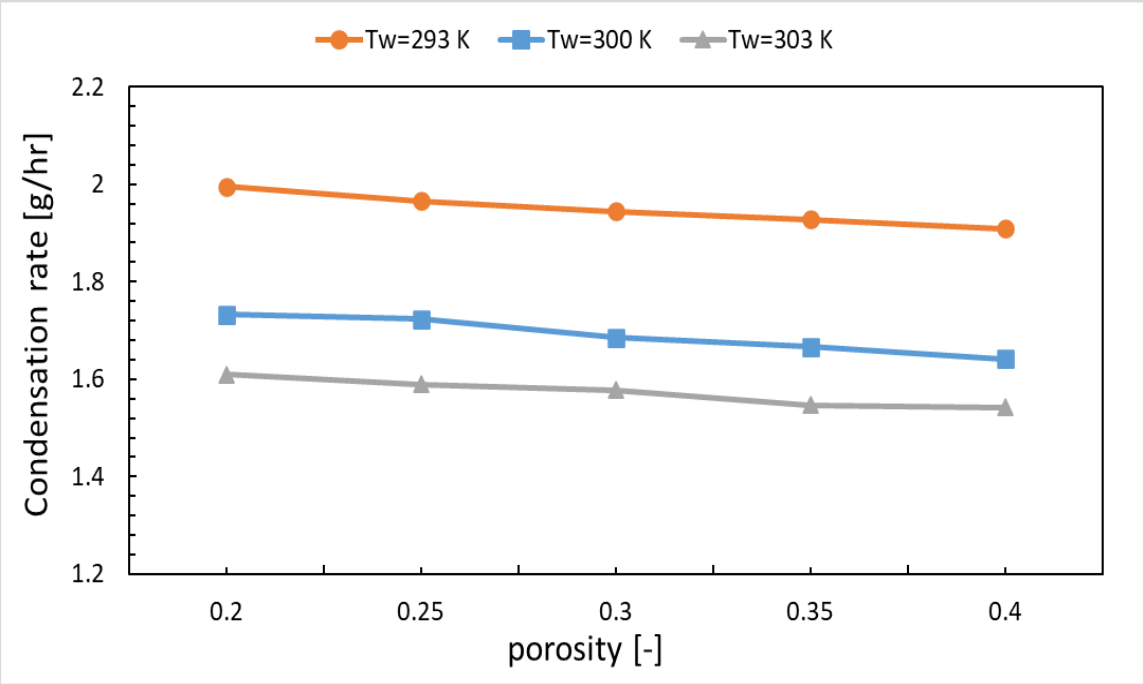

Figure 20. Variation of the condensation rate at different porosity and different water inlet temperature, at outer diameter d_o=0.3, d_i=0.125.

The effects of different parameters such as inlet water temperature, tube outer diameter (d_o), tube internal diameter (d_i), and porosity on the condensation rate and outlet temperature of the flue gas in a transport membrane condenser were studied numerically. Variation of these parameters showed a slight to significant effect on the heat transfer and condensation rate. Within the examined parameters ranges, the highest results were found at inlet water of 293 K, the porosity of 0.2, outer tube diameter of 7.62 mm and inlet tube of 4.70 mm. The results were more sensitive to the variation in the inlet water temperature than the inner and outer tube diameters. Also, the variation of the inner tube diameter has a higher effect on the results than the outer tube diameter. A 38% increase in the internal tube diameter enhances the condensation rate by about 22% to 29% and reduces the flue gas outlet temperature by over 2%. Compared to a 38% increase in the outer tube diameter,

which shows an enhancement in the condensation rate, less than 5%, and reduction about 1% in the outlet flue gas temperature. However, a slight variation in the porosity and outer tube diameter showed a slight or negligible effect on the results. The maximum variation was found as a result of increase the porosity from 0.2 to 0.25, and a further increase in the porosity shows no significant enhancement in the condensation rate such that as the porosity increase from 0.35 to 0.45 the condensation enhanced with less than 1%.

4. CHAPTER IV: SINGLE PHASE MODELING OF TMC USING MIXED CONDENSATION MODEL

In this chapter, the single-phase heat and mass transfer of the TMC with a staggered tube bundle will be investigated using the mixed condensation model. An extensive parametric study will be conducted, including the effects of the geometrical parameters, such as tube diameter and the number of tube rows, and the Reynolds number on the condensation rate and outlet thermal conditions. The mixed model has been proved as an efficient model to simulate the transport of the water vapor and heat from the flue-gas zone to the porous zone and from there to the cooling water zone in a TMC heat exchanger. The mixed condensation model involves small-scale transport phenomena and takes into account the physical properties of the porous membrane, such as the membrane pore size, porosity, and tortuosity. The validation of the mixed condensation was already represented in Chapter 2.

The inlet conditions for both flue gas and water, were set as velocity inlets to target the effects of the Reynolds number on the heat and mass transfer inside the TMC. In all calculations, the water at the inlet flows horizontally at a set velocity of 0.09 m/s from the left-hand side to the right-hand side inside the tubes with a set inlet temperature of 300 K. The temperature of the inlet flue gas was set to 355 K, while its flow velocity was variable in a vertical direction from the bottom side to the upper side of the tube bundles. The corresponding characteristic dimension and boundary conditions presented in Table 9 were used for the numerical simulations unless it is stated otherwise.

Table 9: Dimension and boundary conditions of the TMC staggered tube bundle

Geometrical parameters		**Boundary conditions**	
Number of tubes, N_R	2 – 24	Water inlet temperature, (K)	300
Outside diameter, d_o (mm)	4.572– 7.62	Water inlet velocity, (m/s)	0.09
Inside diameter, d_i (mm)	3.5052	Flue gas inlet temperature, (K)	355
Longitudinal pitch, S_L (mm)	8.788	Flue gas Reynolds number, $Re_{D,max}$	170 - 8900
Transverse pitch, S_T (mm)	13.61	Membrane tube Porosity (-)	20%
Tube Length, L (mm)	431.8	Membrane Thermal conductivity (W/m. K)	30

4.1. TMC Versus Stainless Steel-Based Heat Exchangers

Different simulations using Ansys/Fluent 2019 R1 were conducted to compare the heat transfer and pressure drop in the TMC heat exchanger with the heat transfer and pressure drop in the stainless-steel heat exchanger. The characteristics dimensions of both heat exchangers are the same. The comparisons of the results are shown in Figure 21 in terms of variation of the Nusselt number and Euler number. As seen, the performances of both heat exchangers exhibit the same trends; the Nusselt number and Euler number increases with an increase in the N_R and Reynolds number. As N_R increases from 2 rows to 24 rows, the Nusselt number increases by about 1076% and 1160%, for TMC tube bundle and stainless-steel tube bundle increases, respectively. Also, as N_R increases from 2 rows to 24 rows, the Euler number increases 1020% and 1090% for TMC tube bundle and stainless-steel tube bundle, respectively. In general, the TMC Nu_{conv} is higher than that of the stainless-steel heat exchanger, the maximum and minimum differences between TMC and stainless tube bundles were found as 4% and 22% for N_R=22 and N_R=10, respectively. the

TMC Eu is slightly lower than that of the stainless-steel heat exchanger, about 5% to 11% for the given range N_R. It should be noted that the effective thermal conductivity of the nanoporous ceramic membrane tube bundle is higher than the stainless-steel tube bundle, and the continuous removal of the condensate from the flue gas reduces the thermal resistance at the outer tube surface, which increases the overall Nu_{conv} of the TMC.

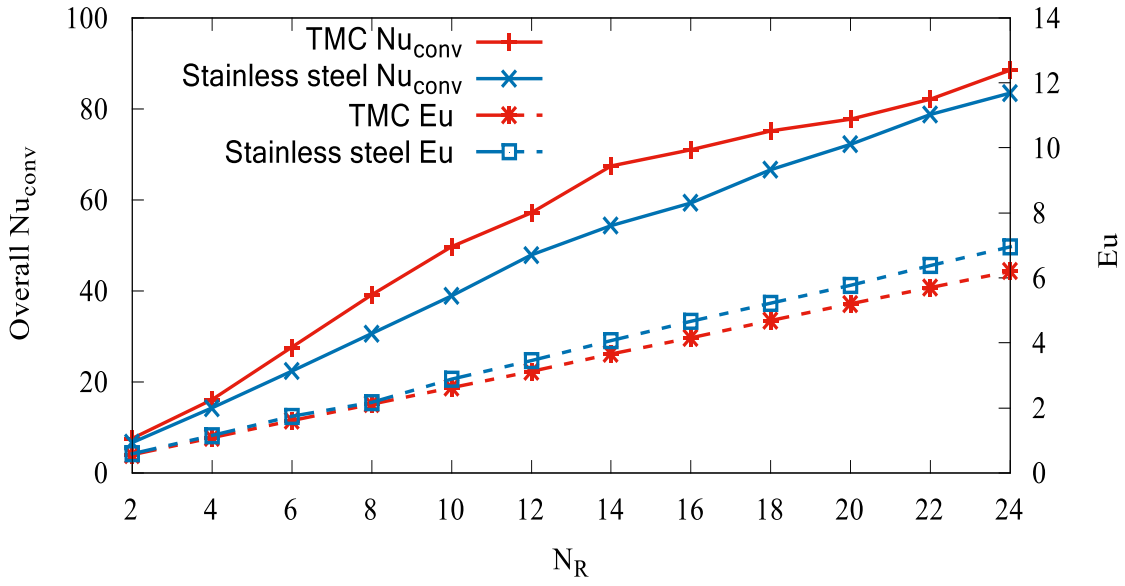

Figure 21. Effect of the Staggered Tubes N_R on the Overall Convective Nusselt Number and Euler Number for the TMC Tube Bundles Compared with Stainless-Steel Heat Exchangers at $Re_{D,max}$=320, T_{fg}=355 K, and $T_{w,in}$=300 K.

Figure 22 also represents the variation of the overall Nu_{conv} and Eu with different Reynolds numbers for both stainless steel heat exchangers and TMC-based heat exchangers. At low Reynolds number the Nusselt number for the stainless-steel bundle was higher than the TMC bundle about 20%. However, increasing the flue gas Reynolds number enhance the Nusselt number for TMC tube bundle compared to the stainless steel

one, the difference was increased from 6% to 27% for the $Re_{D,max}$=878 to 5762. The same Euler number effect trends on the Kind of tube bundle were found in previous paragraph, the TMC Euler were lower than the stainless-steel Euler number, with a minimum difference 11% at $Re_{D,max}$==320 and a maximum 92% of $Re_{D,max}$=4000. However, the variation of Reynolds number showed an inverse relation with Euler number, as Reynolds number increases the Euler number reduce. The reductions were 56% and 71% as Reynolds number increased from 173 to 5762, for TMC and stainless-steel tube bundles, respectively.

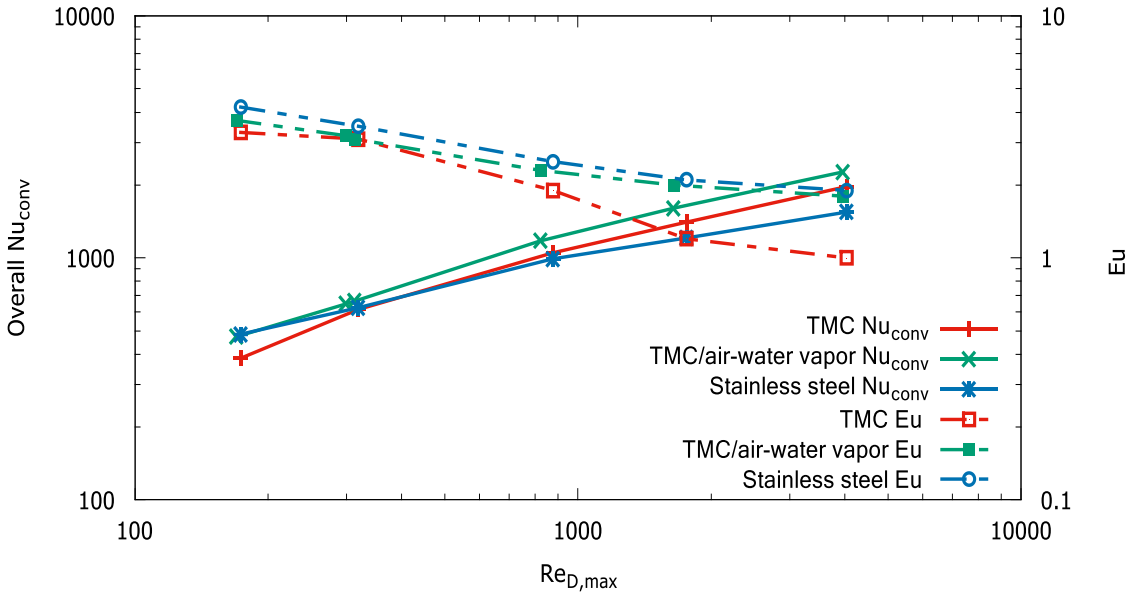

Figure 22. Effect of Reynolds Number on the Overall Convective Nusselt Number, and Euler Number for the TMC compared with Stainless-Steel Heat Exchangers for N_R=12.

The Figure also represents a comparison between a TMC with flue gas as the working fluid and a TMC with an air/water-vapor mixture as a working fluid. The difference between the

working fluids is the existence of CO_2 in the flue gas. The mass fractions of the flue gas species were obtained from the GTI experimental measurement of a power plant, which was given as CO_2 = 4.0%, H_2O = 11.4%, N_2 = 75.6%, and O_2=9.0%, while the air/water vapor mixture species mass fractions were set to H_2O = 11.4%, N_2 = 75.6%, and O_2=13%. A slight change in the overall Nu_{conv} and a significant change in the Eu were noticed as the working fluid changes from flue gas to an air/water-vapor mixture. The Nusselt number was higher, with a maximum 23% for the lowest Reynolds number, for the air mixture than the flue gas. The Euler number of the air mixture is higher than the flue gas, 13% to 86%, for the given range of Reynolds number.

4.2. Heat Transfer of a TMC Tube Bundle

The primary objective of designing the TMC-based heat exchanger is to enhance heat transfer and condensation rate, minimize the pressure drop along the heat exchanger and minimize the number of TMC tubes needed. In the following sections, the effect of the number of rows, N_R, tube diameter, and Reynolds number of the TMC tube bundle were studied numerically.

4.2.1. Effect of the Number of Rows on the Convective Nusselt Number

The TMC-based crossflow tube heat exchanger involves multiple rows of tubes. The flue gas flows perpendicularly to the outer surfaces of these tubes, which increases the turbulence as well as heat and mass transfer at the outer surface of the tube bundles. The heat transfer from the flue gas to the water in the first row of the tube bundles differs from

the tubes in the other rows. The tubes in the front row are surrounded by smooth boundary layers as compared to the tubes in other rows that are prone to turbulent flow with eddies, which enhance heat and mass transfer. In the staggered tube bundle, the flue gas departs from the first row with a substantial amount of momentum, which leads to an impact on the second row that is lying on the flue gas jets' paths. The selection of the number of tube rows is critical to the heat exchanger's efficiency.

Figure 23 represents the variation of overall Nusselt for different staggered N_R at different Reynolds numbers, which is based on the maximum fluid velocity within the tubes. The lines in the Figure represent the condensation-convection Nusselt number, which considers the sensible heat and the latent heat due to the condensation of water vapor. The shapes represent the convective Nusselt number based on the sensible heat only. It is clear that N_R has a significant effect on heat transfer. As N_R increases, so does the Nusselt number. As N_R increases from 2 to 4, the Nusselt number was doubled for the underlined Reynolds numbers. However, at a low Reynolds number, the effect of an increase in N_R is less than that at a high Reynolds number. For example, an increase in N_R from 12 to 24 increases the Nusselt number by about 54% and 57% for $Re_{D,max}$= 320 and 878, respectively and about 128% and 125% for $Re_{D,max}$=1756 and 4073, respectively. From one point of view, this can be related to the high residence time of the flow in the domain at a low Reynolds number, where most of the heat and mass transfer occurs at the first few rows of the tube bundle. From another point of view, this can be related to the high turbulent flow around the upstream tubes for a high Reynolds number, the velocity contour map shown in Figure 25.

Furthermore, the heat transfer increases with increasing N_R because of the increase in the surface area available for heat transfer as well as an increase in the flue gas turbulence, as a result of narrowing flow passages as the tube number is increased. A staggered tube bundle promotes a stronger turbulence intensity, leading to an increase in the heat transfer of the inner rows, as compared to the first two rows. A further discussion on the flue gas turbulence intensity will be detailed in Section 4.6. It should be noticed that the latent heat due to condensation of the water vapor enhances the heat transfer significantly and increases the Nusselt number by up to 23% for $Re_{D,max}$ = 320 and N_R = 24. Based on this generated data a Nusselt number correlation as a function of Reynolds number, N_R, flue gas properties and staggered geometrical parameters will be represented and discussed in Chapter 5.

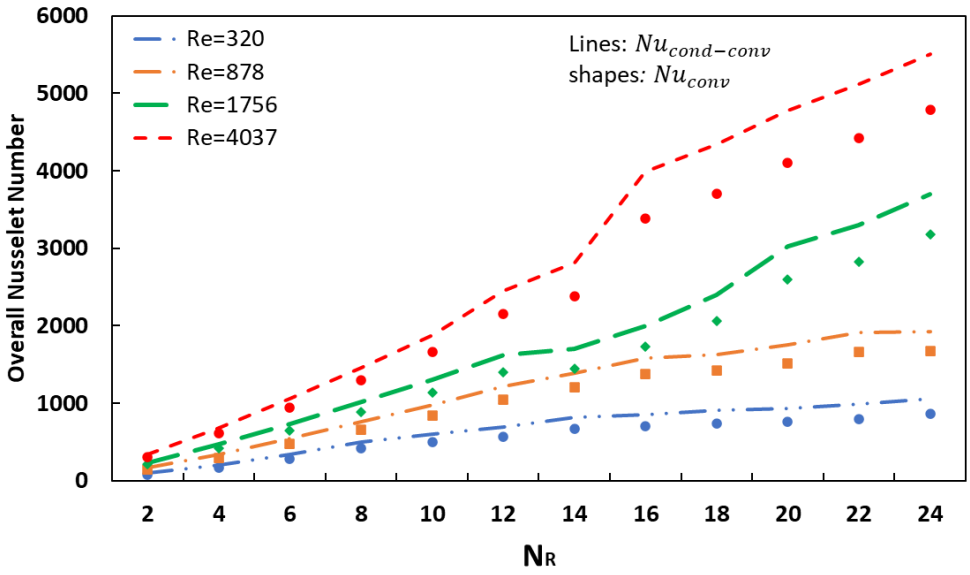

Figure 23. Variation of the overall Nusselt number with the different TMC tube N_R at different Reynolds Number.

4.2.2. Effect of Tube Diameter on the Convective Nusselt Number

The heat transfer from the flue gas on the TMC tube bundle was also studied numerically for different tube outer diameters (d_o). Figure 24 represents the overall Nusselt number for 12 rows of staggered tube bundles of different tube diameters. The results showed that an increase in the tube diameter increases the Nusselt number. The smaller diameters of d_o= 5.49 mm and 4.57 mm have lower heat transfer and Nusselt numbers than the other two larger tube diameters, due to the significant reduction in the surface of the nanoporous membrane tube and increased tube spacing, which reduces the heat transfer. At $Re_{D,max}$=320, the average Nusselt number was increased by 12.4% and 15.1% respectively at each step of increasing the tube diameter from 5.49 mm to 7.62 mm. The maximum Nusselt number was found at d_o=7.62 mm. A slight variation was noticed as the tube diameter increases from 4.57 mm to 5.49 mm.

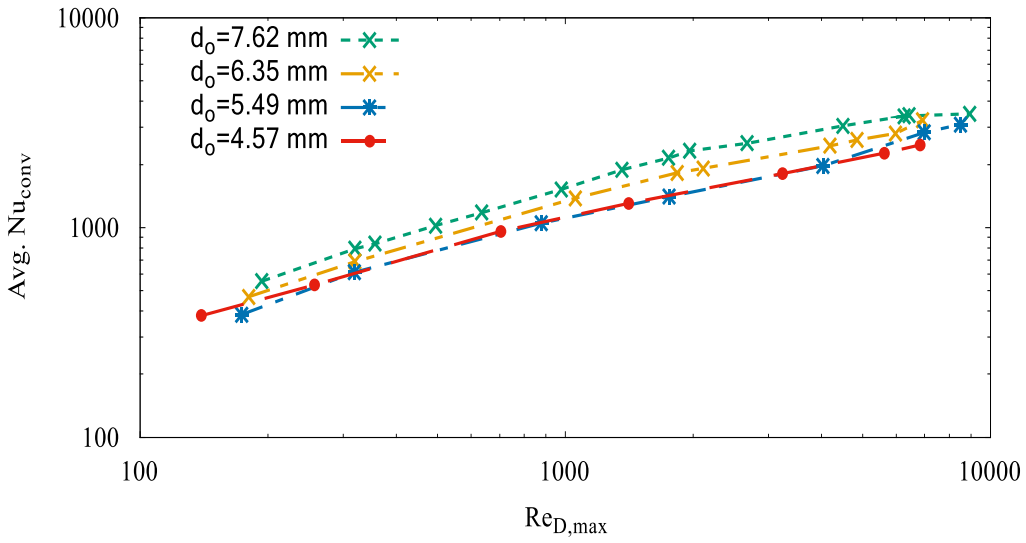

Figure 24. Variation of the overall Nusselt number with the different TMC tube diameter at Different Reynolds Number, N_R=12 rows.

Figure 25 shows the typical temperature and velocity contours for different tube diameters at $Re_{D,max}$=320. As the tube diameter decreases, the flue gas temperature remains high as the flow moves toward the outlet of the tube bundle. This is because of the reduction in the tube surface area, which increases the tube spacing and reduces the heat transfer from the flue gas side to the waterside. The Figure also shows that an increase in tube diameter minimizes the number of tubes and the number of tube rows needed for the tube bundle. The red arrow in the Figure indicates where the flue gas temperature became stable with no further reduction. For tube diameters 4.57 mm, 5.49 mm, and 6.35 mm, the flue gas temperature became stable after the flow passed rows 10, 9, and 7, respectively. However, for tube diameter 7.62 mm, the same temperature range is achieved after the flow passes the row number 4. The flow temperature kept in further reduction until the flow passes the entire tube bundle.

The variation in the temperature reduction through the four domains was associated with the variation in the flow velocity inside the domains, as seen in Figure 24 b). Reducing the tube diameter decreases the flow velocity which results in the reduction of flow turbulence, which reduces the heat transfer rate. The black arrows indicate where the velocity becomes stable within the given domains. It should be mentioned that the Reynolds numbers were calculated at the maximum velocity of the flow. The maximum velocity is a function of tube diameter and spacing. The maximum velocity at the inlet, 1.51 m/s, was observed for the tube bundle with d_o=5.49 mm. Based on this generated data a Nusselt number correlations as a function of Reynolds number, N_R, flue gas properties and staggered geometrical parameters will be represented and discussed in Chapter 5.

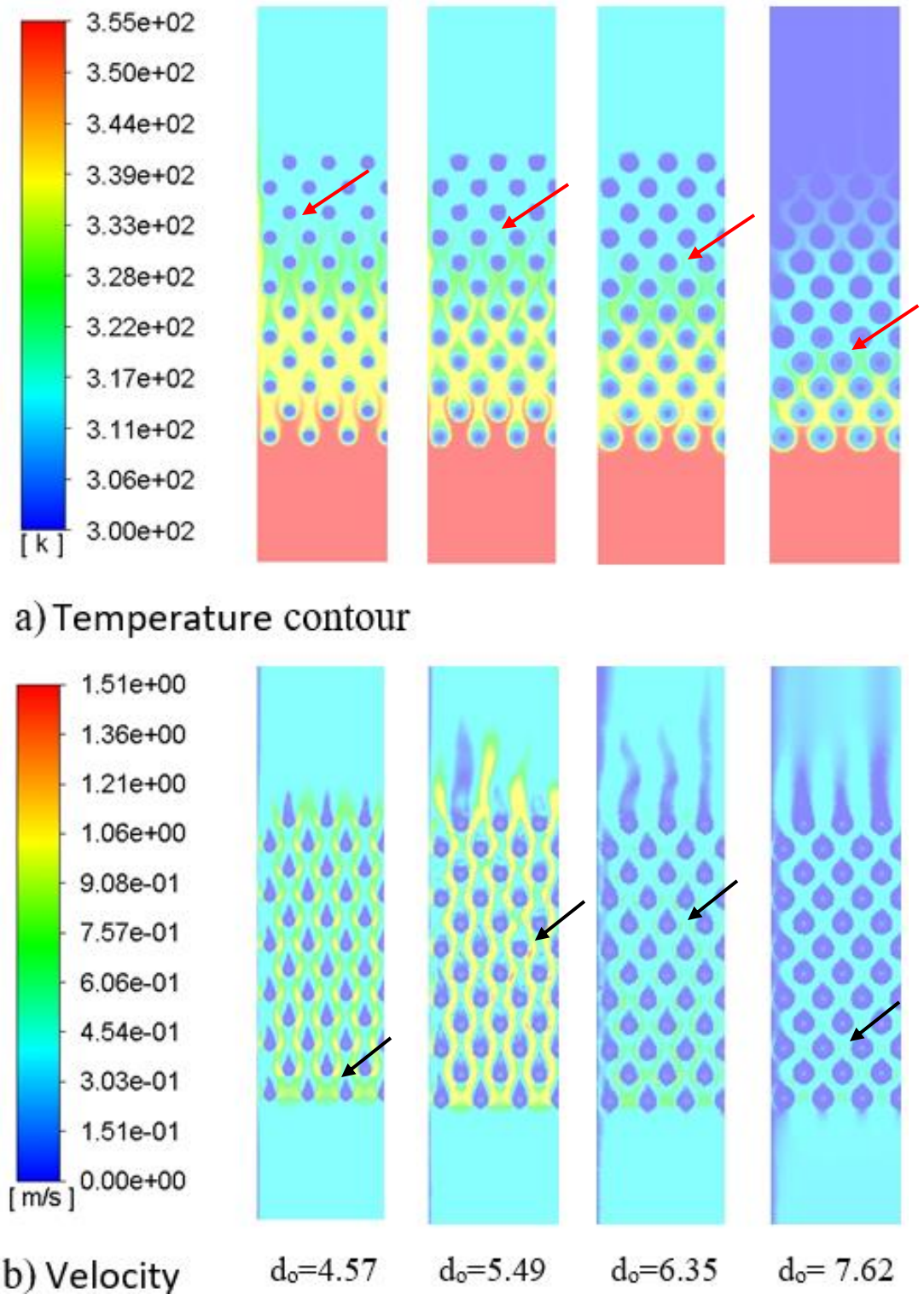

Figure 25: Effect of tube diameter: a) Temperature contour, and b) Velocity distributions at $Re_{D,max}$=320. The contour plots are for a plane of 216 mm from the water inlet. Dimension in mm.

4.3. Condensation Rate

Figure 26 (a) represents the condensation rate with the variation of the number of TMC rows. The results showed that an increase in the N_R on the TMC staggered tube bundle and the Reynolds number increases the condensation rate and reduces the water recovery efficiency through the tube bundle. This is because an increase in the Reynolds number is associated with an increase in the mass flow rate of the flue gas, which increases the condensation rate. Also, increasing the number of TMC rows increases the condensation surface area and the water flow rate in each TMC tube bundle, therefore the outlet temperature and average surface temperature of the TMC tubes decrease, which increases the condensation rate. However, at a high Reynolds number of 4037, no enhancement in the condensation rate and water recovery efficiency were noticed as the N_R increase above 16. This is due to the significant reduction in the flue gas temperature and water vapor content as the flue gas flow from the inlet to the outlet in case of N_R above 16.

Figure 26 (b) shows that the water recovery efficiency decreases as the Reynolds number increases. Higher water recovery efficiency can be achieved at a lower Reynolds number, which is associated with a lower mass flow rate of the flowing gas. In this case, the flue gas has a higher residence time at a lower mass flow rate in the TMC tube bundle. This literature reference also confirmed this result [17, 53, 61].

a)

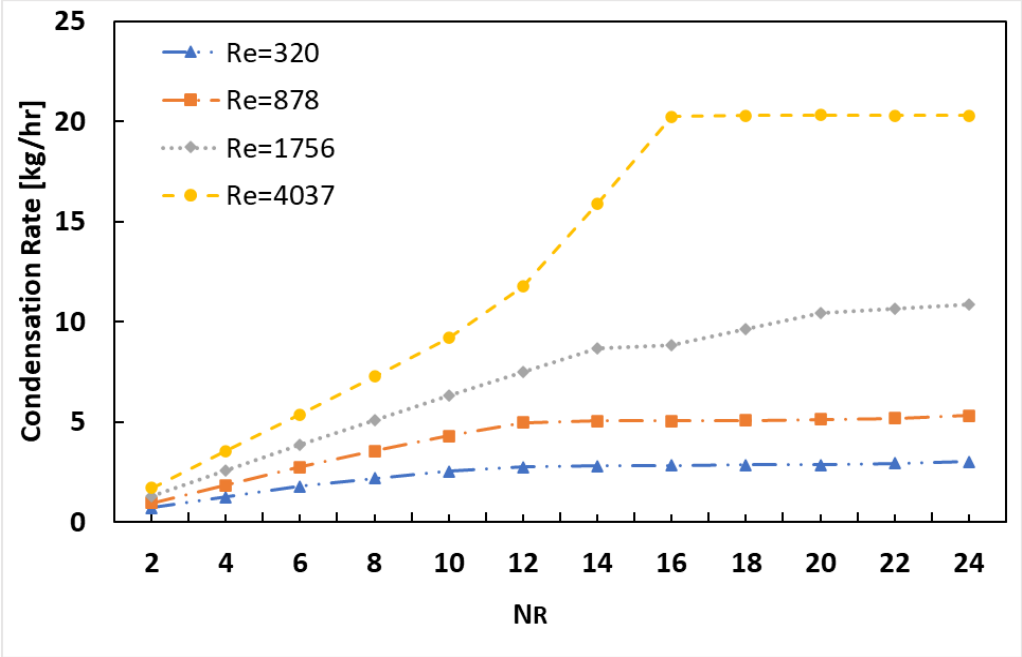

b)

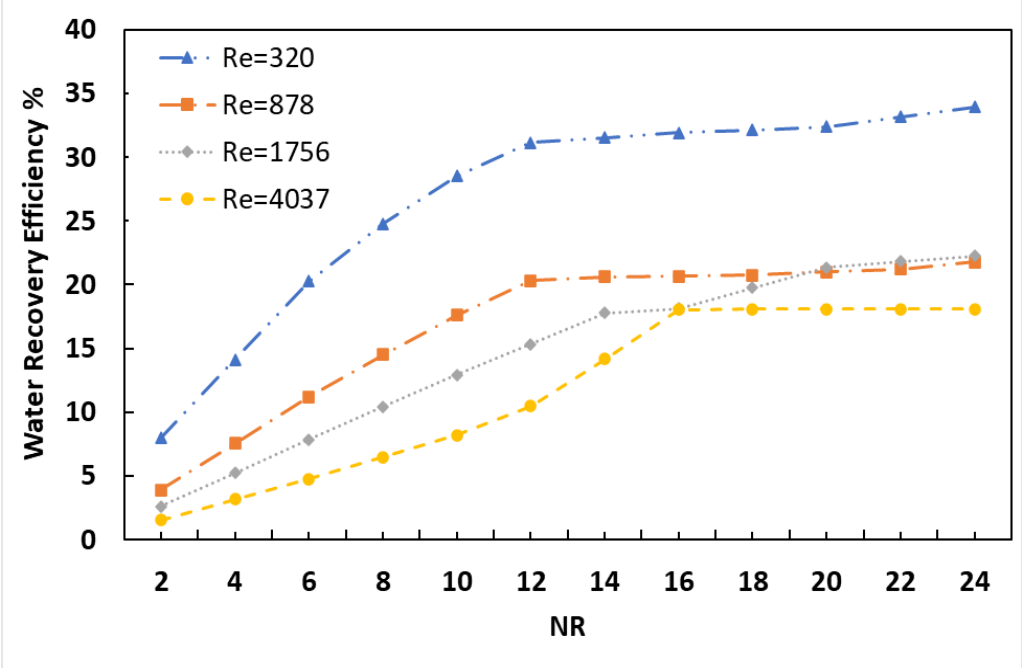

Figure 26. The Variation of a) condensation rate and water recovery efficiency, b) Water Recovery Efficiency with the Different tube N_R for Different Reynolds Number, d_o= 5.49 mm.

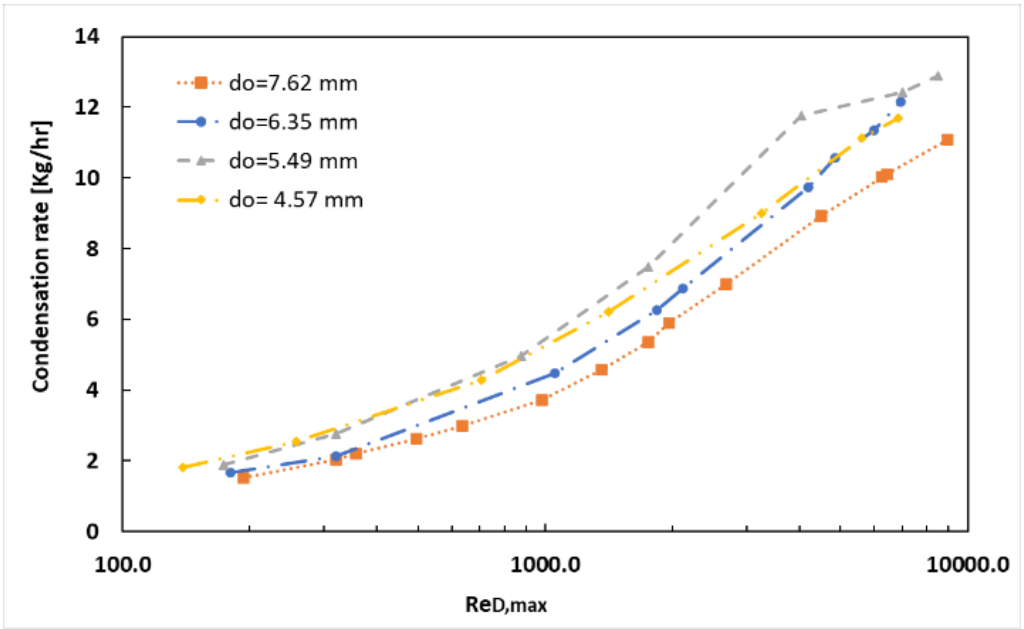

(a)

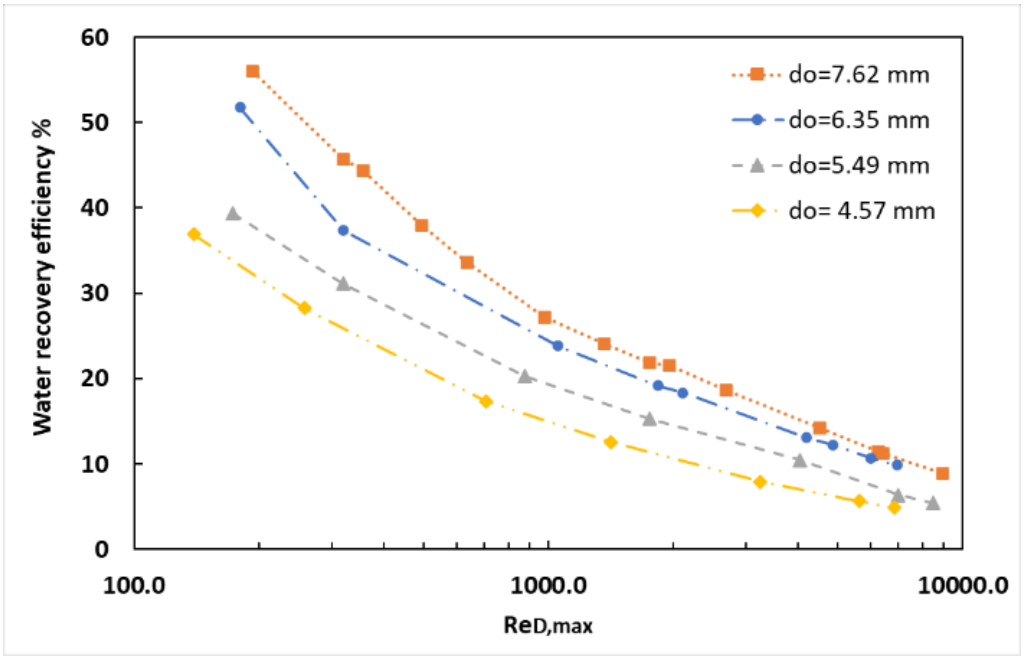

(b)

Figure 27. (Variation of a) Condensation rate, and b) Water Recovery Efficiency with the Different TMC Tube Diameter/Spacing at Different Reynolds Number.

Figure 27 (a) and (b) represent the variations of the condensation rate and water recovery efficiency, respectively, with the variation of tube outer diameter at different Reynolds

numbers. The results were evaluated for tube bundles of N_R = 12. As seen, the maximum condensation rate and lowest water recovery efficiency were obtained for d_o= 5.49 mm. Increasing the tube diameter to 7.62 mm reduces the condensation rate but significantly enhances the water recovery efficiency. Different parameters affect the condensation rate in investigating the tube bundles with different outer tube diameters. Reducing the tube diameter increases the flow velocity and turbulence and shear, which enhances the heat transfer and the condensation rate. However, an increase in the flow velocity reduces the residence time, which reduces the water recovery efficiency. The effect of the condensation rate as a result of the variation of Reynolds number on the Convection condensation Nusselt number will be provided in Chapter 5. The condensation rate added as a dimensionless design parameter that includes the effect of the nanoporous ceramic membrane tube dimension and properties and the flue gas moisture content conditions.

4.4. Pressure Drops (Hydraulic Resistance)

Previous research and experimental results indicated that the pressure drops across the tube bundle are relative to the flow velocity, physical properties, N_R, and tube arrangement. The total pressure drop inside the tube bundle is described by the hydraulic resistance and is considered one of the most important attributes that impact the design of the heat exchanger. The hydraulic resistance inside the tube bundle is usually represented by the Euler number and friction factor, as given in Equations (81) and (82). In the following sections, the flue gas pressure drop inside the TMC tube bundles was calculated for

different tube rows, N_R, tube diameter, and different Reynolds numbers. A comparison with existence single phase correlation will be represented in chapter 5.

4.4.1. Effect of the TMC number of rows on the pressure drops

Figure 28 represents the pressure drop inside the TMC tube bundle represented by Euler number. The numerical results of the TMC tube bundle showed that the number of rows has a significant effect on the pressure drop. An increase in the number of rows increases the Euler number linearly. With increasing N_R, the entrance and exit flow conditions to the tube bundle affect the total loss of kinetic energy. The variation of Reynolds number also represents a significant effect on the pressure drop. At low Reynolds, the pressure drops were less sensitive to the variation of the number of rows than the high Reynolds. Increasing the Reynolds number increases the pressure drops sensitivity to the variation of the N_R. Further discussion and comparison on this relation to the pressure drop based on the previous single phase metal heat exchanger will be provided in chapter 5.

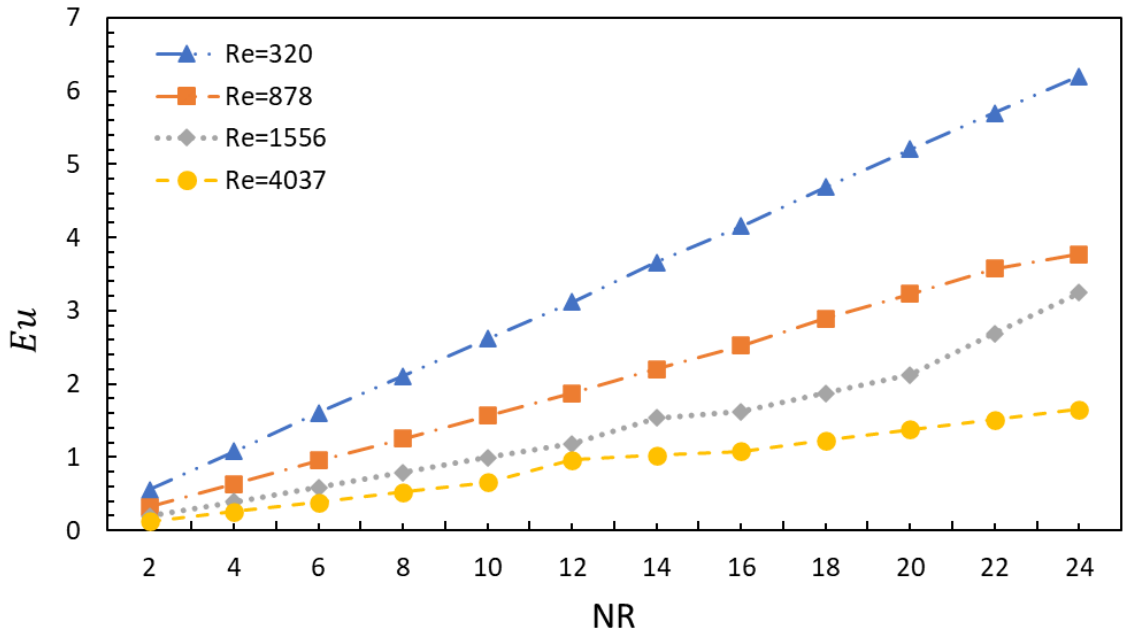

Figure 28. Variation of the Euler Number, *Eu* , With TMC number of Rows N_R for Different for Reynolds Numbers.

4.4.2. Effect of the tube diameter on the pressure drops

The effect of the tube diameter on the pressure drops was also investigated numerically. Figure 29 represents the variation of the friction factor at different Reynolds numbers for different TMC tube diameters. As seen, a decrease in the tube diameter increases the friction factor, while an increase in the Reynolds number reduces the friction factor. Decrease the tube diameter increases the tube spacing, and a larger space between the tubes or rows allows the formation of vortices which affects the tube bundle resistance and increases the friction factor. The total pressure reduction for the given range of Reynolds number were 54%, 170%, 47%, and 44% for the tube diameters 7.62 mm 6.35 mm, 5.49

mm, and 4.57 mm, respectively. Further discussion and comparison on this relation to the previous single phase metal heat exchanger will be provided in chapter 5.

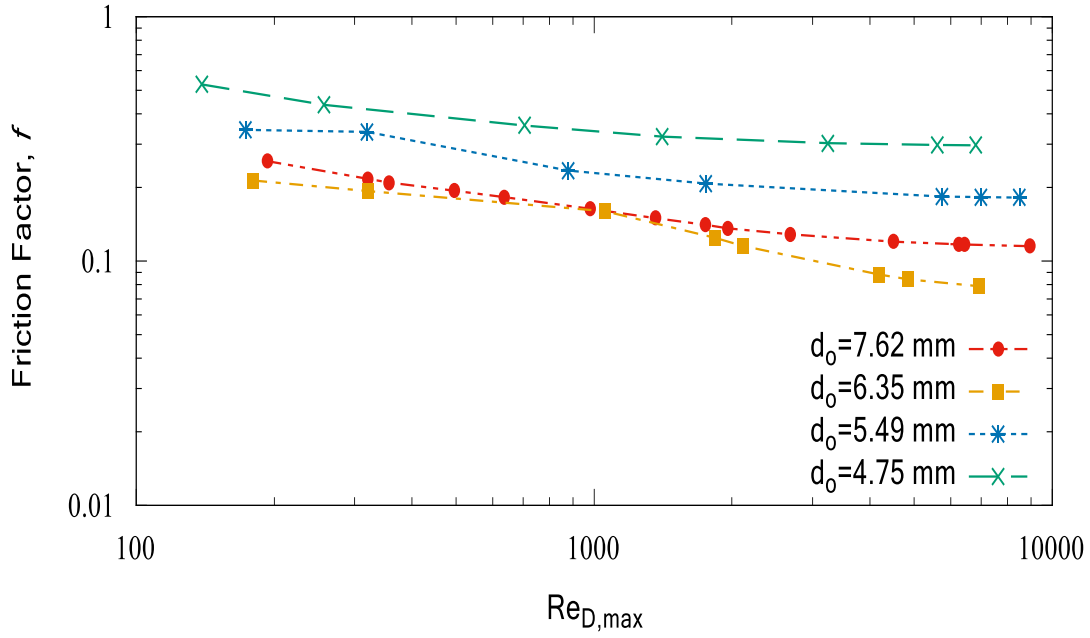

Figure 29. Variation of the Friction Factor, f , with Reynolds Number for Different TMC Tube Diameters/Spacing.

4.5. Flue Gas Turbulence Intensity

Another objective of this Chapter was to investigate the effects of the flue gas turbulence intensity on the condensation rate, heat transfer, and pressure drop for staggered-tube crossflow TMC heat exchangers numerically. The mixed condensation model coupled with the species transport model was used to calculate the condensation rate.

The mass and heat recovery in the TMC-based heat exchanger is influenced by not only different geometrical parameters but also the flow velocity behaviors. The flue gas flows outside the staggered tubes perpendicularly to their orientations, which enhances the flow

turbulence. An increase in the flow turbulence intensity will increase the heat and mass transfer through the TMC tube bundles. The turbulence intensity is a significant parameter determining the velocity profile and turbulence variation inside the heat exchanger. The turbulence intensity, TI , is the ratio of the root-mean-square of the velocity fluctuations, u'_{rms}, to the average flow velocity u_{avg}, [111].

$$TI = \frac{u'_{rms}}{u_{avg}} \tag{84}$$

where, $$u'_{rms} = \sqrt{\frac{1}{3}\left(u_x'^2 + u_y'^2 + u_z'^2\right)} = \sqrt{\frac{2}{3}k} \tag{85}$$

and, k is the turbulent kinetic energy (TKE), as given by the following relation:

$$k = \frac{1}{2}\left(u_x'^2 + u_y'^2 + u_z'^2\right) \tag{86}$$

The velocity component is the difference between the instantaneous and mean velocity $u' = u - \bar{u}$.

The effect of the flue gas turbulence intensity on the heat and mass transfer in the TMC-based heat exchanger was studied numerically at different Reynolds numbers. The Reynolds number was calculated using the maximum fluid velocity within the tube bundle, Equation (72). The turbulence intensity varied from 5% to 25% at the inlet conditions of the flue gas, while the tube bundle geometry was fixed during the variation of the turbulence intensity. The staggered configurations of the tube bundle are found to enhance the turbulent flow as represented by turbulent kinetic energy (TKE). The contour plots of

the TKE for different tube diameters and turbulence intensities, 5% and 25%, are represented in Figure 30.

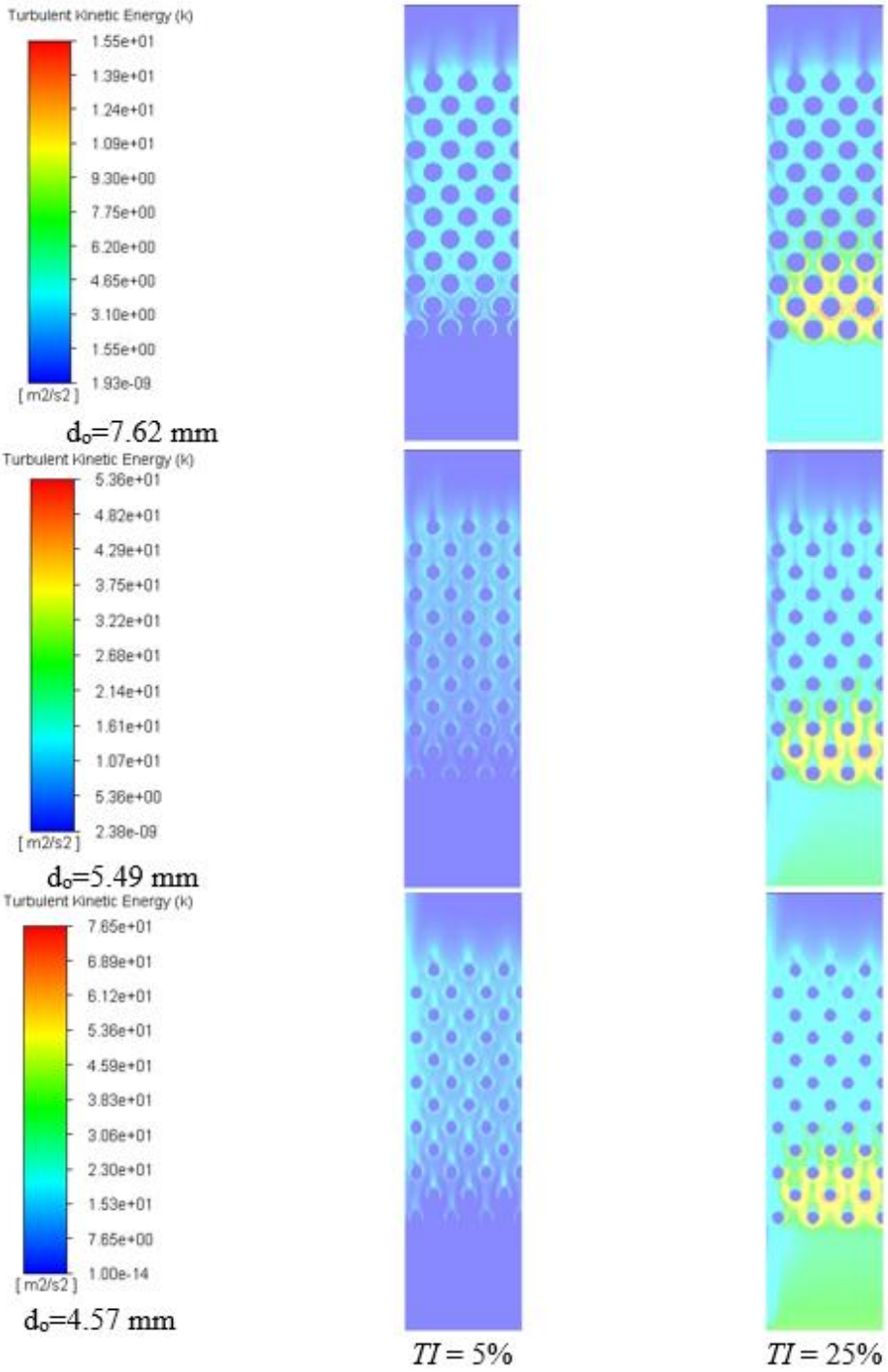

Figure 30. Contour Plot of the Turbulent Kinetic Energy (TKE) at different Flue Gas Inlet Turbulence Intensity for Different Tube Diameter, $Re_{d,max}$=10000.

The TKE value is a describe to the turbulence strength of the flow, it is used for a measurement of the flow intensity. It is clear that for different tube diameters, increasing the turbulence intensity of the flue gas from 5% to 25% enhances the turbulent kinetic energy significantly. Also, increasing the tube diameter reduces the turbulent kinetic energy of the tube bundle. This can be explained by the increase in the mean velocity, as the tube diameter increases the tube spacing reduces, which increases the mean velocity compared to the fluctuation velocity in the field.

The highest value of the TKE was observed around the tubes of the first four rows of the tube bundles. Also, the TKE start decreases as the flow passes the third row of the tube bundle. This is related to the significant reduction in the flue gas temperature, as the nanoporous ceramic membrane recovered a large portion of both sensible and latent heat. Furthermore, the staggered configuration of the tube bundle adjusts the local flow turbulence after the flow passes a specific number of rows, which depends on the tube diameter and spacing. This can be confirmed by looking carefully to the contours for the two , it can be noticed that for *TI*=5% and *TI*=25%, the flow stabilized and the staggered tube configuration adjust the level of turbulence after passing the 6^{th} row for the given of tube diameters. However, at the first few rows of the tube bundle, a significant variation in the TKE was noticed resulting from the increase in the turbulence intensity of flue gas from 5% to 25%. It should be mentioned that rows most of the heat transfer and condensation rate take place the first few rows the flow passes.

4.5.1. The effect of Reynolds number and turbulence intensity on Nusselt number

The effect of the Reynolds number on the average convective Nusselt for different turbulence intensities, 5%, 10%, 15%, 20%, and 25%, can be visualized in Figure 31. At the low Reynolds number, where the flow is characterized as a laminar flow, the average convective Nusselt number increase in percentage with respect to Reynolds number is steady and minimal. While at a high Reynolds number, the percentage of increase is high.

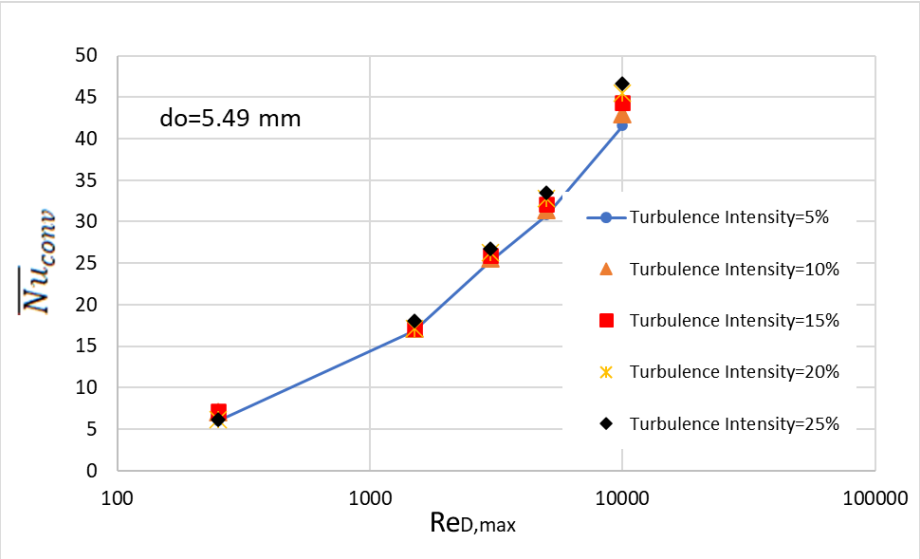

Figure 31. Variation of the Average Convective Nusselt with Reynolds Number for Different Turbulence Intensities.

From Figure 30 we can also notice a slight variation in the Nusselt number for Reynolds number up to 3000 as a result of the increase of turbulence intensity from 5% to 25%, a detailed analysis in this matter will be provided in the next section. However, the increase in the Reynolds increases the enhancement in the heat transfer and the Nusselt number. The variation of the Nusselt number with respect to the variation of *TI* will be represented in the following section.

4.5.2. Effect of the turbulence intensity on the average convective Nusselt number

Similar results were obtained for the effect of the turbulence intensity on the average convective Nusselt number. The results are represented in Figure 32. The average convective Nusselt number was calculated from the sensible heat transfer. Increased Reynolds number enhances the heat transfer and Nusselt number significantly. The maximum variations in the Nusselt number were observed at do= 4.57 mm with an increase of 7.13%, 11.32%, and 15.24%, for $Re_{D,max}$ = 3000, 5000, and 10000, respectively, as the turbulence intensity increase from 5% to 25%. The enhancement of the Nusselt number is due to the enhancement in the heat transfer, which is related to the rise in the level of flow turbulence. Increases in the turbulence intensity cause significant mixing of the boundary layer, enhancing the momentum and heat transfer between the fluid species and from there to the tube wall. This had confirmed in the contour plot of TKE, Figure 30. It was noted that the high value of TKE for higher turbulence intensity is surrounded by the tube wall in the first few rows, where the most of most of the heat transfer occurs through the tube bundle.

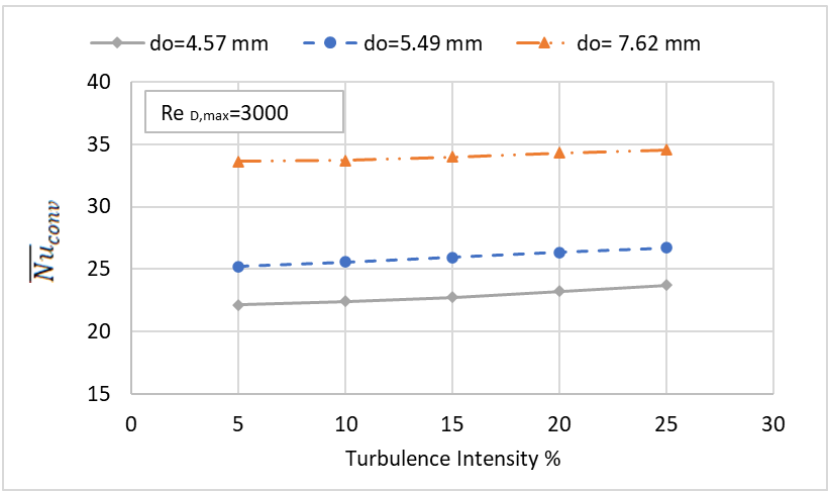

(a)

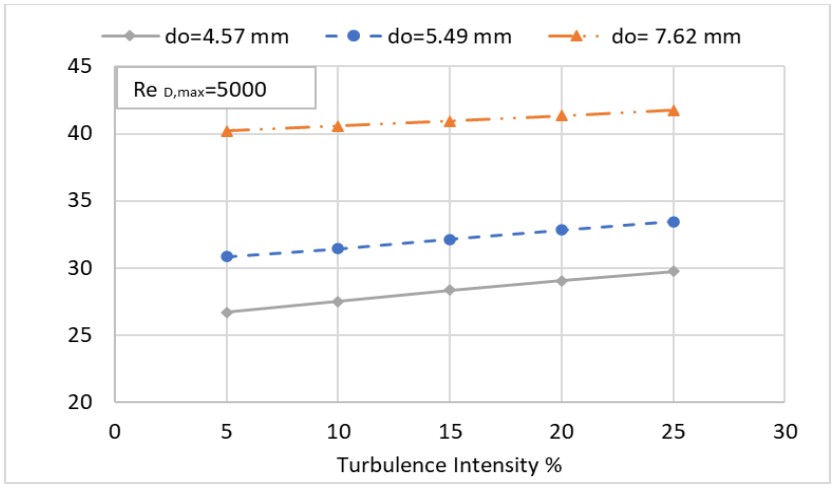

(b)

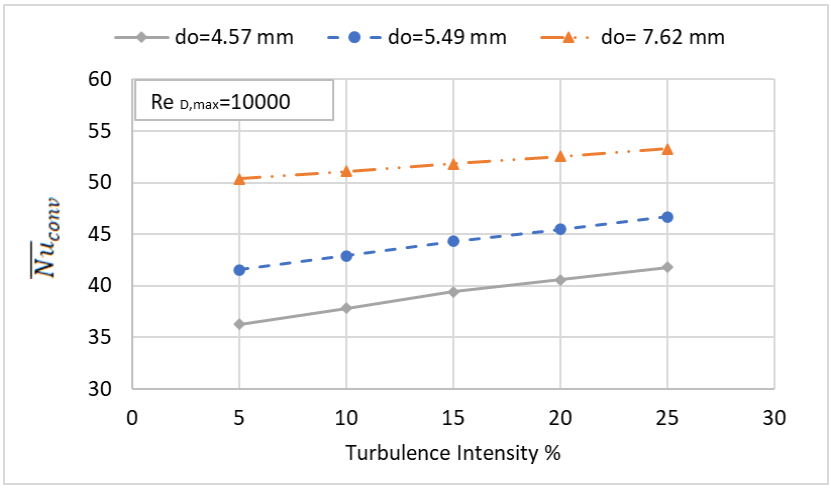

(c)

Figure 32. Variation of the Average Convective Nusselt Number with Different Turbulence Intensity at Different Reynolds Numbers: (a) $Re_{D,max}$=3000, (b) $Re_{D,max}$=5000, and (c) $Re_{D,max}$=10000.

4.5.3. Effect of turbulence intensity on the condensation rate

Figure 33 represents the variation of the condensation rate with turbulence intensity. As seen, the condensation rate increases with an increase in the turbulence intensity. The variation of the tube diameters was sensitive to the variation of turbulence intensity. As the turbulence intensity increases from 5% to 25% the minimum in the condensation rate were 3.9% for do =7.62 mm, at $Re_{D,max}$=3000, and maximum increase was 12.2% for d_o = 4.57 mm at $Re_{D,max}$=5000, respectively. Also, the variation of maximum condensation rate with respect to the turbulence intensity was obtained at the TMC tube bundle with d_o = 5.49 mm. At d_o= 5.49 mm, the condensation rate increases 8.3%, 9.7% and 5.8% for $Re_{D,max}$ = 3000, 5000, and 10000, respectively, as the turbulence intensity increase from 5% to 25%. The lowest variation was obtained from TMC tube with do = 7.62 mm with an increase of 3.9%, 5.1% and 5.41% for $Re_{D,max}$ = 3000 , 5000, and 10000, respectively, as the turbulence intensity increases from 5% to 25%.

The optimum condensation rate was found at a tube diameter of d_o = 5.49 mm. This finding is associated to a combination of factors, the tube spacing and the membrane tube surface area available for the heat transfer, pressure drop and condensation rate.

It should be mentioned that the effect of the flue gas turbulence intensity increases with an increase in the Reynold numbers. The Reynolds number was evaluated at the maximum velocity of the tube bundle. The condensation rate, pressure drop, and the Nusselt number also increase as the Reynolds number increases for the three tube diameters investigated.

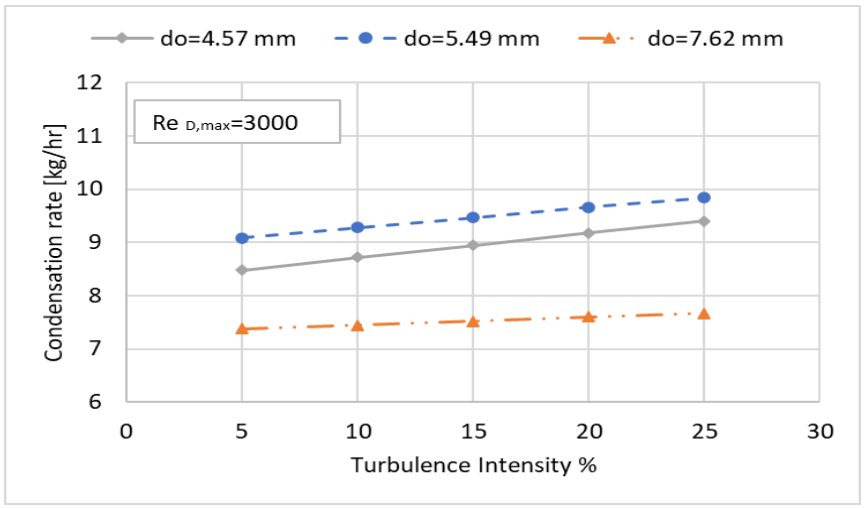

(a)

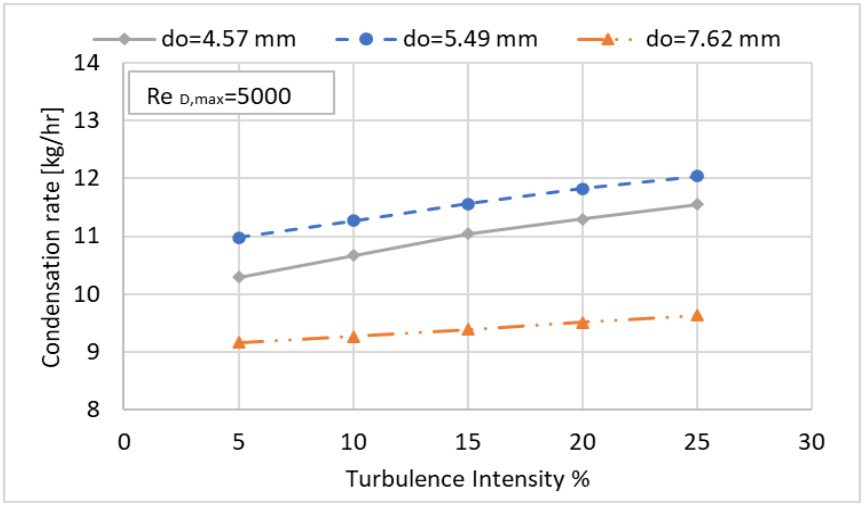

(b)

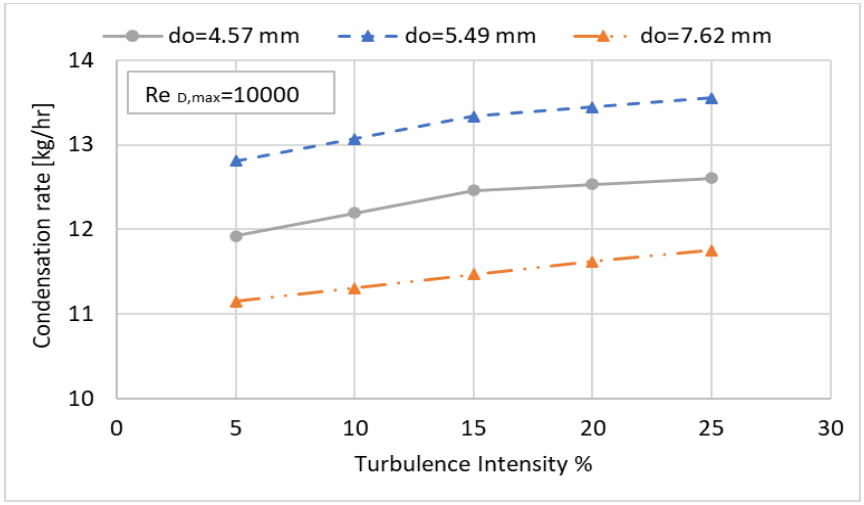

(c)

Figure 33: Variation of the Condensation Rate with Different Turbulence Intensity at Different Reynolds Numbers: (a) $Re_{D,max}$=3000, (b) $Re_{D,max}$=5000, and (c) $Re_{D,max}$=10000.

4.5.4. Effect of turbulence intensity on the pressure drop

Figure 34 represents the pressure drop variation with turbulence intensity for tube diameters and different Reynolds numbers. As seen, an increase in Reynolds number and tube diameters increases the pressure drop significantly. However, an increase in turbulence intensity increases the pressure drop slightly. The maximum pressure drops were observed for the TMC tube bundles of d_o = 4.57 mm. However, the maximum variation in the pressure drop with respect to turbulence intensity was observed for the TMC tube bundle of d_o = 5.49 mm. The percentage of increases were 6.7%, 8.2%, and 9.9% for $Re_{D,max}$ = 3000 , 5000, and 10000, respectively, as the turbulence intensity increase from 5% to 25%. The lowest variation in the pressure drop was obtained from the TMC tube bundle of do = 7.62 mm with an increase of 2.2%, 3.0%, and 4.1% for $Re_{D,max}$ = 3000, 5000, and 10000, respectively, as the turbulence intensity increase from 5% to 25%. The tube diameter affects the free space between the tubes, as the tube diameter decreases the free space increase, which allows the flow vortices to form and that would increase tube bundle resistance and so the pressure drop.

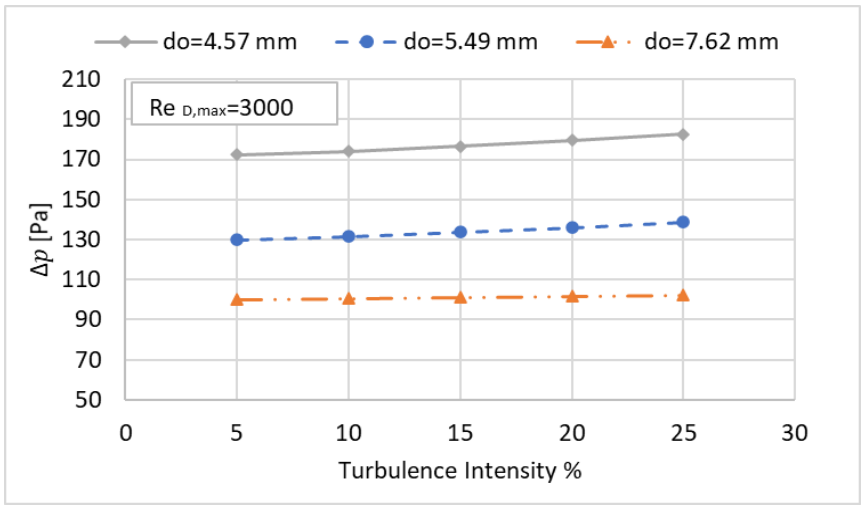

(a)

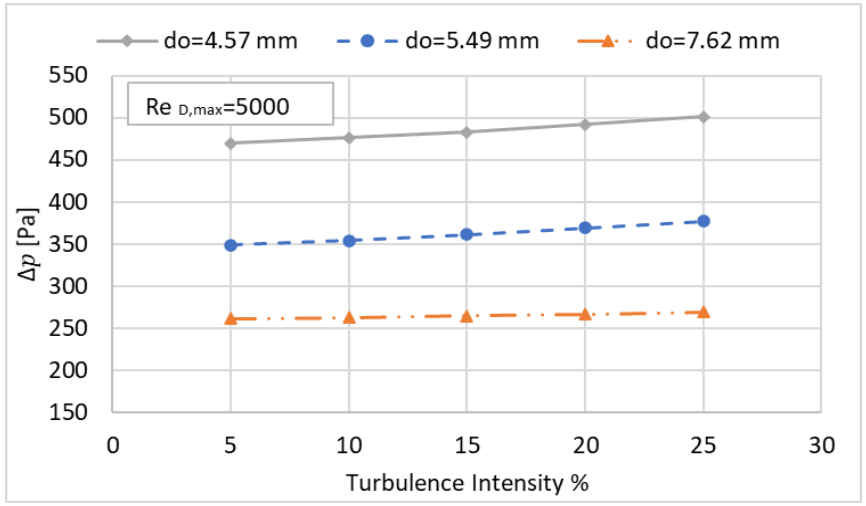

(b)

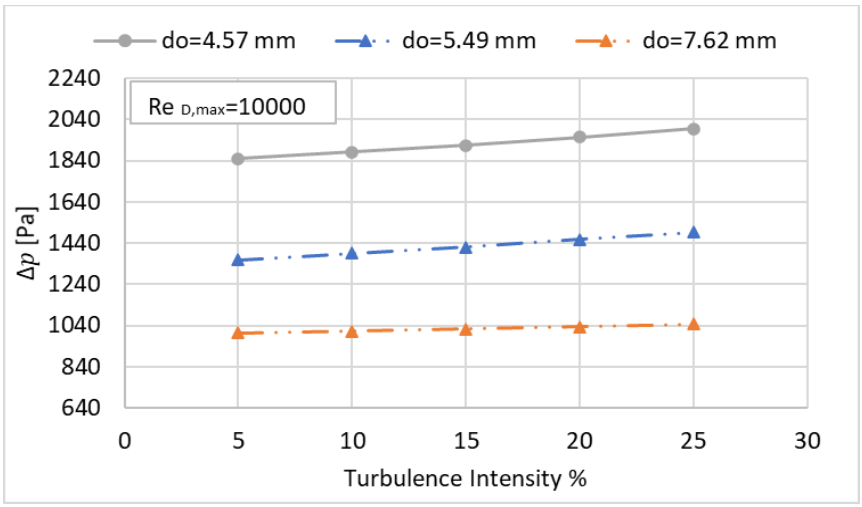

(c)

Figure 34. The Variation of the Pressure Drops with Different Turbulence Intensity at Different Reynolds Numbers.

The effects of flue gas turbulence intensity on condensation rate, convective heat transfer, and pressure drop of the TMC heat exchanger in cross flow were numerically investigated with a validated CFD model. The results showed a significant enhancement in the TKE, condensation rate, pressure drop, and heat transfer at a given Reynolds number with the increased turbulence intensity. An increase in the turbulence intensity could lead to an enhancement in the condensation rate and Nusselt number which could lead to an overall enhancement of the TMC tube bundle performance. The maximum variation in the condensation rate was 12.15%, at $Re_{D,max}$=5000, for tube bundle with do= 4.57 mm, when the turbulence intensity increases from 5% to 25%. However, the optimum condensation was obtained for tube bundle with do= 5.49 mm. The maximum increase in the Nusselt number was 15.24% at $Re_{D,max}$=10000, for tube bundle with do= 4.57. The variation of the outer tube diameter affects the mass and heat transfer from TMC tube bundle significantly. Increasing the tube diameter increases the heat transfer from the tube bundle, this is because of the increase in the heat transfer surface area. Increase the Reynolds number also increase the condensation rate, pressure drop, and Nusselt number; the pressure drops also affected by the variation of the turbulence intensity, in most of the cases was a slight effect, The maximum increase in the pressure drop was 9.91% at $Re_{D,max}$=5000, for tube bundle with d_o= 5.49.

4.6. Dominant Condensation Mode in TMC

The heat and mass transfer in the TMC tube bundle has been studied experimentally and numerically, and several models have been proposed to calculate the condensation rate. Researchers have reported that the transport of the flue gas through the membrane

condenser involves two mechanisms: wall condensation and capillary condensation. However, the dominant condensation mechanism is still under debate and needs more investigation.

In this section, the dominant condensation mechanism involved in the transport membrane condenser is investigated numerically. Simulations of heat and mass transfer in a cross-flow transport membrane condenser tube bundle were used to examine the role played by membrane porosity and flue-gas water vapor mass fraction for the dominant condensation mechanism. A single-phase multi-species model coupled with a mixed condensation model was used to investigate the dominant condensation mechanism at different membrane porosity and water vapor mass fraction. The Numerical simulation was executed using Ansys/Fluent 2021 R1 software. The mixed condensation model, which is based on wall condensation and capillary condensation, was written in the user-defined functions (UDF). The flue-gas turbulence was modeled using the shear stress transport SST k-ω turbulence model. The nanoporous membrane pores are loaded with condensate of water vapor which is transported to the other side of the membrane. This mechanism reduces the flue gas temperature, increases the cooling water temperature, and recovers water and its latent heat from the flue gas.

In this work, the condensation of the water vapor at the membrane's outer surface is modeled in conjunction with simultaneously occurring capillary condensation. Different parameters would affect the condensation rate from both mechanisms. In the current work, the effect of the two major parameters: the membrane porosity and the water-vapor mass fraction will be represented and discussed.

4.6.1. Effect of membrane porosity on the dominant condensation mode

The effect of the membrane porosity on the condensation rate and condensation mechanism have been studied numerically using the mixed condensation model. The membrane porosity varied from 0.15 to 0.5. Figure 35 represents the effect of porosity on the condensation rate as well as the condensation percentage gained from both mechanisms. The results showed that an increase in the membrane porosity, from 0.15 to 0.5, increases the condensation rate by about 18%. Also, the percentage of capillary condensation mechanism out of the total condensation rate increases as the porosity increases, while the wall condensation percentage decreases. Also, at low membrane porosity, the model can detect less capillary condensation compared to wall condensation. This is related to the limited capacity of the membrane pores, which reduces the ability to condensate water vapor inside the pores by the capillary condensation mechanism.

As the pores are filled with condensate water, the water will start to condense at the membrane's outer surface due to the temperature difference between the flue gas and the surface of the nanoporous membrane tube. It should also be noted that wall condensation is based on the diffusion of condensable gases (i.e., water vapor) toward the cold surface (nanoporous ceramic tubes).

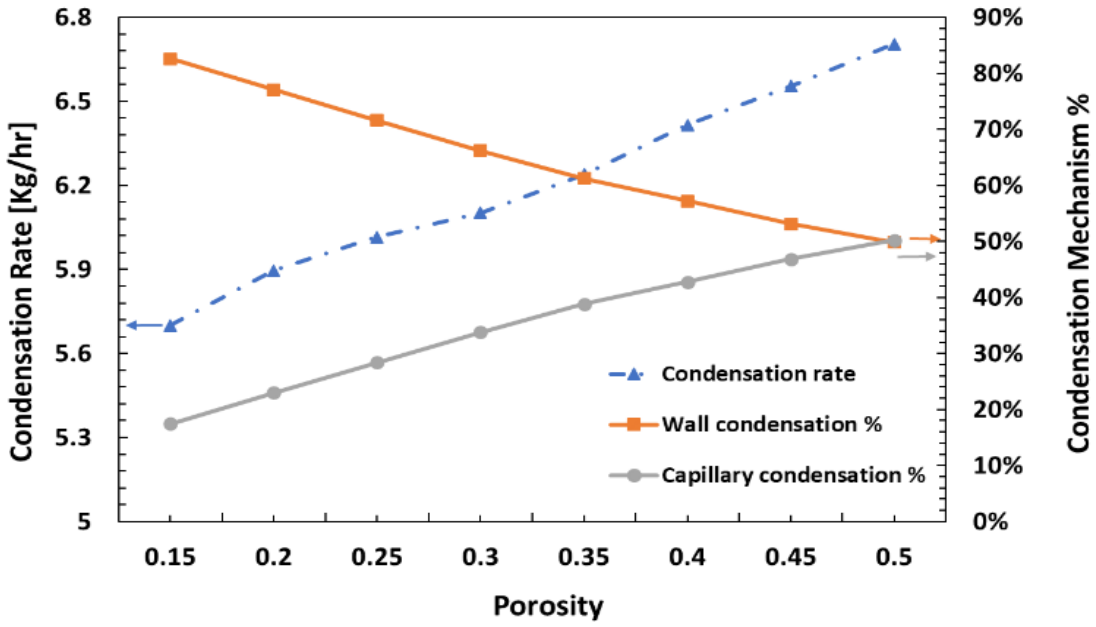

Figure 35. Effect of Membrane Porosity in the Condensation Rate and Condensation Percentage from each Condensation Mechanism, Water Vapor Mass Fraction [wt.] = 11.4%.

The Nusselt number from the latent heat is also calculated for both condensation mechanisms. The results are represented in Figure 36. According to the calculated results, the latent Nusselt number due to the wall condensation rate is higher than the one due to capillary condensation. These are related to the amount of latent heat released due to water vapor condensation from each mechanism. Also, the Figure represents the effect of the porosity on the convection Nusselt number. It can be seen that an increase in the membrane porosity reduces the convection Nusselt number and the amount of the recovered sensible heat. This reduction is related to the linear relation between the effective thermal conductivity of the membrane and the membrane porosity, see Equation (71). As the membrane porosity increases the effective thermal conductivity decreases, which reduces the heat transfer from the flue gas side to the cooling water.

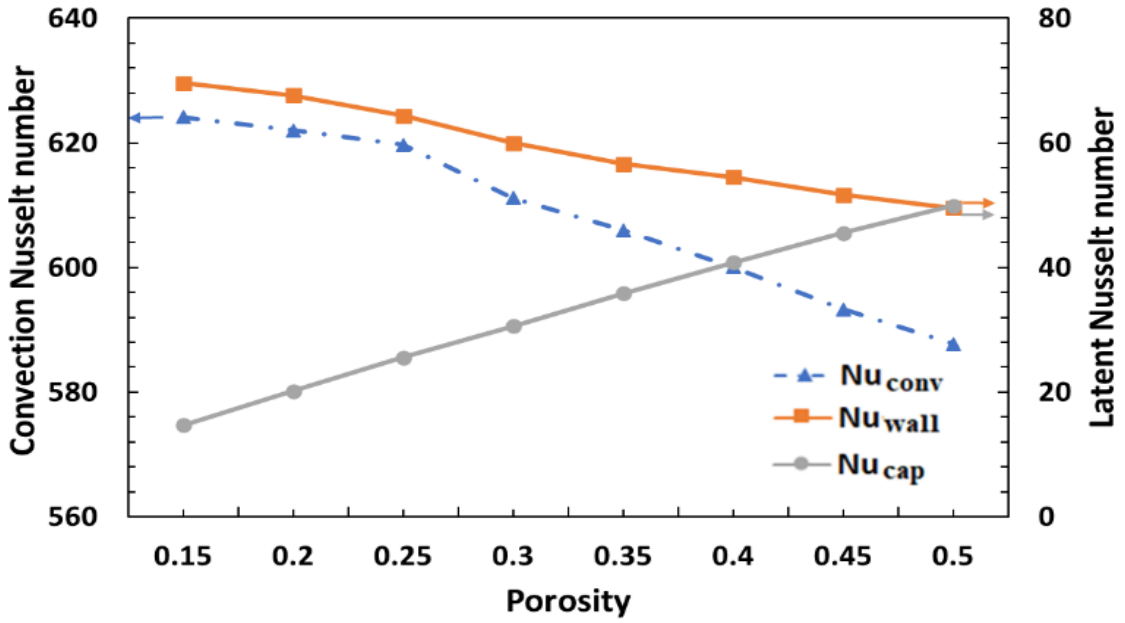

Figure 36. Effect of Membrane Porosity in the Convection and Latent Nusselt Number. Water Vapor Mass Fraction [wt.] =11.4%.

4.6.2. Effect of water vapor content on the dominant condensation mode

The effect of the flue-gas water-vapor mass fraction on the dominant condensation mechanism was also studied numerically. The water-vapor mass fraction varied from 8% to 21%, representing a typical water-vapor mass fraction in the flue gas from power plants. Figure 37 represents the variation of the condensation rate with water vapor mass fraction. According to the represented results, wall condensation is the dominant condensation mechanism. As the mass fraction of water vapor increases, the condensation rate increases significantly. The percentage of the condensation rate due to the wall condensation mechanism increases from 69% to 87% of the total condensation rate when the mass fraction increases from 8% to 21%. It should be noted that the wall condensation

mechanism is a function of the condensable species mass fraction. The numerical results detected no direct effect of the water-vapor mass fraction on the capillary mechanism, and this is confirmed by Equation (12). The amount of condensation rate gained by the capillary condensation mechanism is the same. However, the reduction in the percentage is due to the increase in the wall condensation percentage.

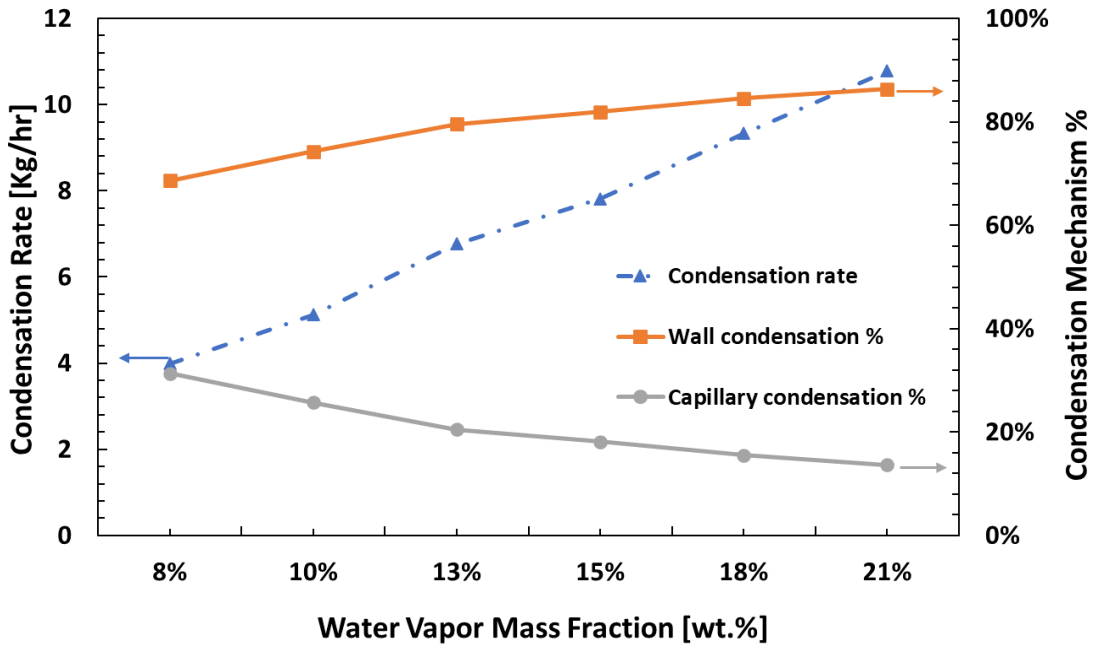

Figure 37 Effect of the Water Vapor Mass Fraction in the Condensation Rate and Condensation Percentage from each Condensation Mechanism. $\varepsilon = 0.2$.

The difference between the two-condensation mechanism is also represented by the latent Nusselt number in Figure 38. Given the represented results, the highest latent Nusselt number was obtained from the wall condensation mechanism. As the water vapor mass fraction increases, the latent Nusselt number from the wall condensation mechanism increases significantly because of the increased condensation rate due to wall condensation.

The Figure also represents the variation of the convection Nusselt number with the water vapor mass fraction. An increase in the water vapor mass fraction decreases the convection Nusselt number significantly.

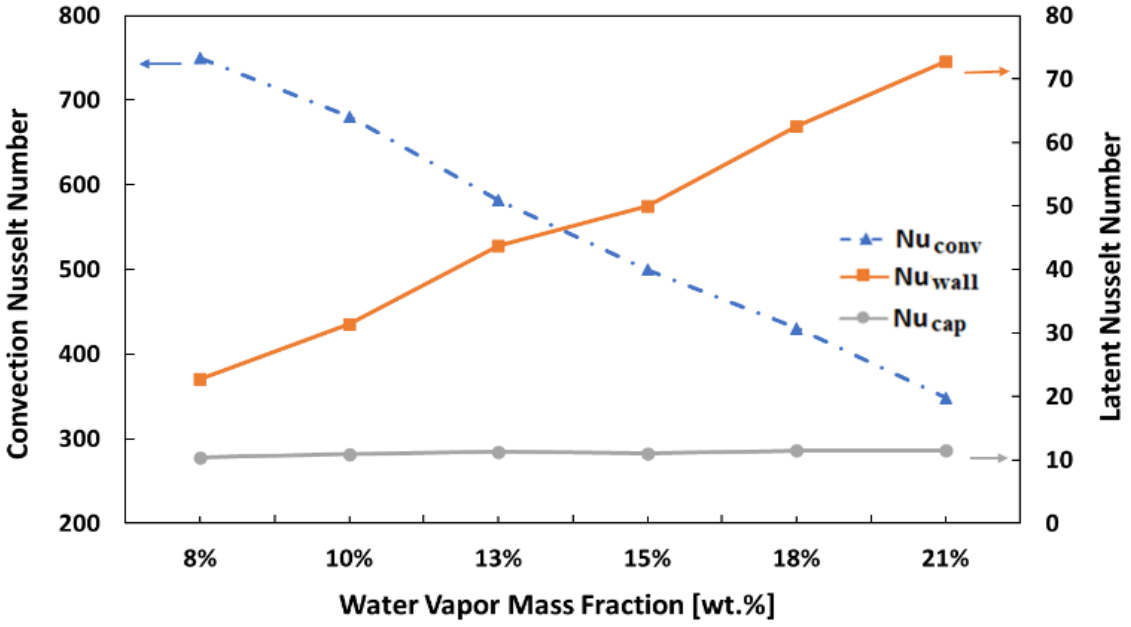

Figure 38: Effect of Water Vapor Mass Fraction in the Convection and Latent Nusselt Number. $\varepsilon = 0.2$.

5. CHAPTER V: CORRELATIONS FOR TMC STAGGERED-TUBE BUNDLES

The existing staggered tube bundle correlations consider only a single-phase flow (no condensation), while the TMC phase change occurs at the outlet surface of the membrane tubes, which affects the heat transfer coefficient and pressure drop across the tube bundles. There is a need to propose a new correlation based on the working conditions and principles that are required for the TMC-based heat exchanger. The goals of this Chapter are to study the similarities and variations between the TMC Nusselt number and pressure drops as well as the single-phase correlations to avoid misuse and develop numerically the correlations of the heat and mass transfer and pressure drop imposed by the membrane tubes in the TMC heat exchanger at different N_R, tube diameters, and Reynolds numbers.

5.1. Heat Transfer Correlation of a Staggered Tube Bundle

The numerical results from the previous Chapters were compared with different single-phase correlations developed previously in the literature, which are listed in Table 10. The staggered tube arrangement of the TMC tube bundle increases the turbulence kinetic energy between the bundle rows, which enhances the heat transfer from the flowing flue gas to the tubes and accordingly increases the Nusselt number concerning the Reynolds number. Reynolds number has a significant impact on the heat transfer from the tube bank. In most of the previously developed single-phase correlations, the power index of the Reynolds number varies from 0.4 to 0.6.

Table 10. Average Nusselt number correlations developed in the literature, at a Different Range of Reynolds Numbers.

Reynolds number	Average Nusselt number Correlation	Reference
$10^3 < \mathrm{Re}_{D,max} < 2 \times 10^5$	$Nu_f = 0.40\ C_1\ Re_{D,max}^{0.60} Pr_f^{0.36} (\frac{Pr_f}{Pr_w})^{0.25}$	Zukauskas, 1972 [71]
$10^0 < \mathrm{Re}_{D,max} < 5 \times 10^2$	$Nu_f = 1.04\ C_1\ Re_{D,max}^{0.40} Pr_f^{0.36} (\frac{Pr_f}{Pr_w})^{0.25}$	Zukauskas, 1978 [72]
$5 \times 10^2 < \mathrm{Re}_{D,max} < 2 \times 10^5$	$Nu_f = 0.71\ C_1 Re_{D,max}^{0.40} Pr_f^{0.36} (\frac{Pr_f}{Pr_w})^{0.25}$	
$10^0 < \mathrm{Re}_{D,max} < 10^3$	$Nu_f = 1.309\ C_1 Re_{D,max}^{0.36} Pr_f^{0.34} (\frac{Pr_f}{Pr_w})^{0.26}$	Zukauskas and Ulinskas (1988) [73]
$10^3 < \mathrm{Re}_{D,max} < 2 \times 10^5$	$Nu_f = 0.273\ C_1 Re_{D,max}^{0.635} Pr_f^{0.34} (\frac{Pr_f}{Pr_w})^{0.26}$	
$10^0 < \mathrm{Re}_{D,max} < 2 \times 10^5$	$Nu_f = 0.37\ Re_{D,max}^{0.59} Pr_f^{0.36} (\frac{Pr_f}{Pr_w})^{0.25}$	Lin et al. 2013 [17]
$5 \times 10^2 < \mathrm{Re}_{D,max} < 4 \times 10^{54}$	$Nu_f = 0.35\ C_1 F_a Re_{D,max}^{0.57} Pr_f^{1/3}$ $F_a = 1 + 0.1 * \left({S_l}/{d_o}\right) * (0.35/({S_T}/{d_o})$	Modified Grimson model [70]

C_1 is based on the correction factor for the number of rows [71].

Figure 39 shows a comparison between the average convective Nusselt number from the TMC mixed model and different single-phase correlations. The average convective Nusselt number is evaluated from sensible heat transfer only. It can be seen that the correlation of Zukauskas 1972 was very close to the numerical convection Nusselt number of the flue gas. Good agreement is observed with Zukauskas 1972 [71] at N_R= 6, 12, and 16 with a maximum error of 17% and 28%, 63%, and 65% respectively, at $Re_{D,max}$=320. For this correlation, the error% increases with an increase in the number of rows. For the modified Grimson model [70] the TMC results deviate significantly with minimum error 10 and maximum error reaches to from 45% to 126% for different Reynolds and N_R. It should be noted that Lin et al. 2013 is a correlation developed for the heat and mass transfer from the

flue gas using the TMC and it relates the convective Nusselt number only with the flue gas Reynold number and Prandtl [17]. They used the two-step chemical reaction model on the outer surface of the tubes to calculate the condensation rate. The TMC mixed model is in good agreement with Lin et al. 2013 [17] correlation at N_R= 6 and 12. However, there is a maximum divergence, about 45%, for N_R= 16 and 20 at $Re_{D,max}$=173.

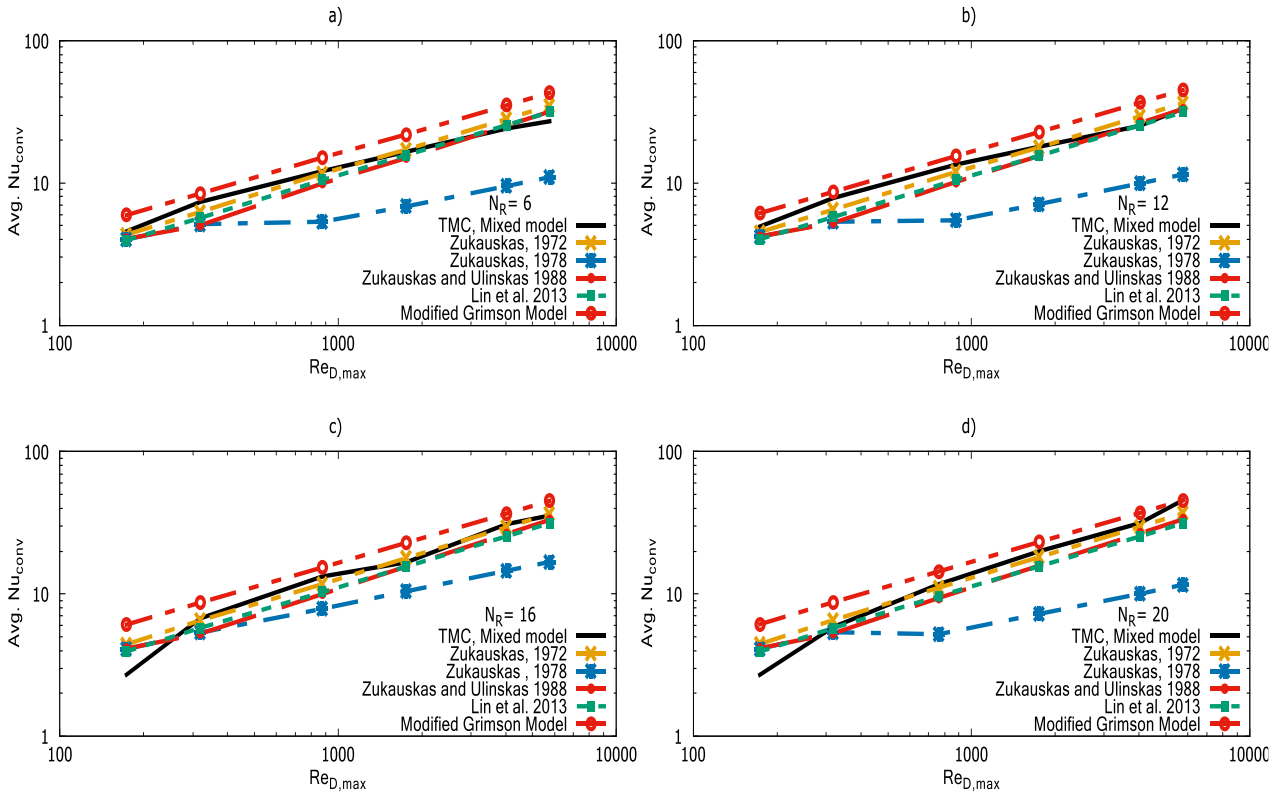

Figure 39: Variation of the Average Convective Nusselt Number of Staggered TMC Compared to the Previously Developed Single-Phase Correlation for Different Number of Rows: a) N_R=6 rows, b) N_R=12 rows, c) N_R=16 rows, and d) N_R=20 rows. For the tube bundle of d_o= 5.49 mm.

Figure 40 represents the effect of tube diameter on the average convective Nusselt number. The results compared the average convective Nusselt number from the TMC mixed model

and different correlations. At d_o=4.57, 5.49, 6.35, and 7.62 mm, the modified Grimson model [70] predicts the heat transfer from the TMC tube bundle with a maximum error of 21%, 20.5%, 21%, and 29% respectively. The comparison with Zukauskas and Ulinskas (1988) [73] showed a significant deviation from TMC results, the error percentage varied between 38% and reached up to 200%. The comparison with of Lin et al. 2013 [17] correlation showed variation in the results for different tube diameters, the closer results were obtained for d_o=5.49, this is probably related to the similarity between this tube bundle and the bundle used by Lin et al. 2013 [17] to build their correlation. However, at d_o =7.62 the results showed significant deviation with an error range 24% to 41% for the given Reynolds number. However, this correlation has no considerations for tube diameter or tube spacing.

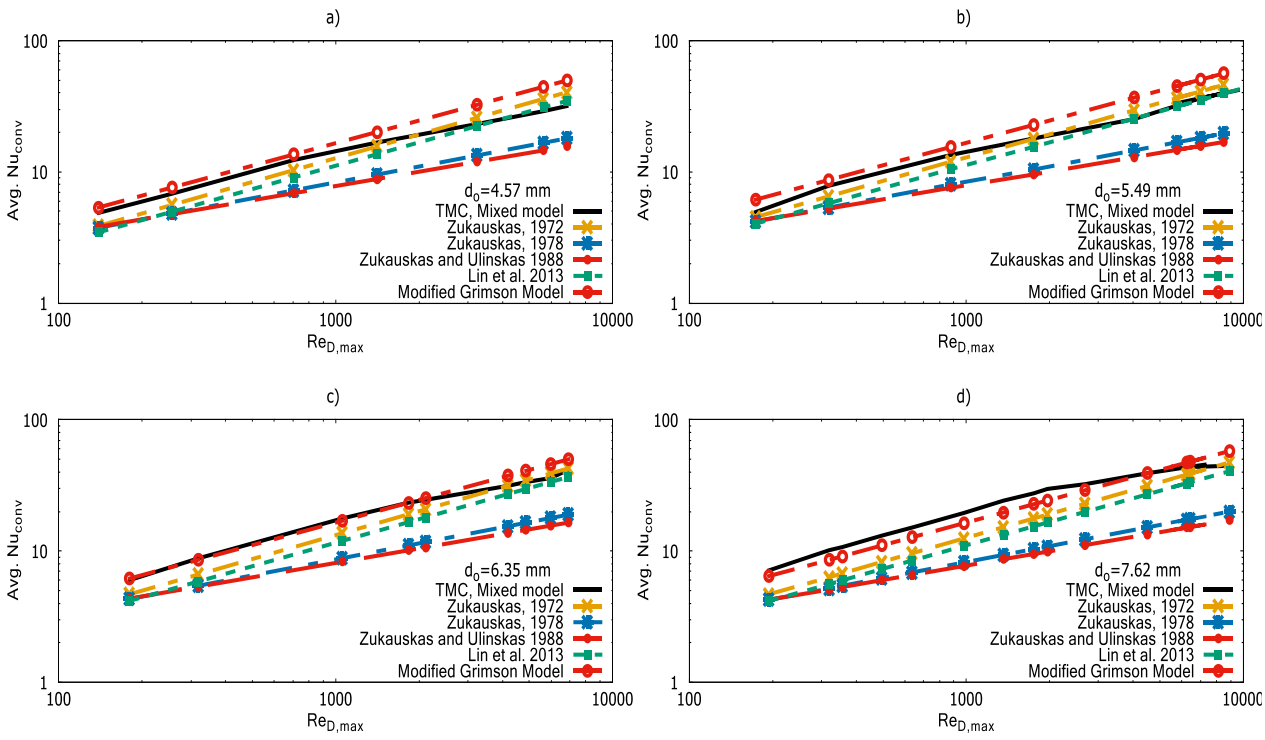

Figure 40: Variation of the Average Nusselt Number of Staggered TMC Compared to the Previously Developed Single-Phase Correlation for Different Tube Diameter: a) d_o= 4.57 mm, b) d_o= 5.49 mm, c) d_o= 6.35 mm, and d) d_o= 7.62 mm. For N_R=12 rows.

5.1.1. Proposed correlations of TMC Nusselt number

It was found that, except for selected conditions, The existing single-phase correlations showed a significant deviation from the TMC results obtained numerically. The comparison results showed that no one single phase correlation published in the literature can predict the heat transfer from TMC for the defined range of parameters. At a certain point of the design parameters, some correlations predict the results well, however the same correlations showed a significant deviation from the TMC results once the design

parameters have changed. Furthermore, the single phase considered no phase change (condensation) occurs membrane properties.

The following correlation of the convection Nusselt number for the TMC is derived based on numerical results, represented in Chapter 4, within examined parameter ranges:

$$\overline{Nu}_{conv}^{corr} = A_1\, N_R^{a1}\left(A_2 + \left(\frac{S_T}{S_T - d_o}\right)^{a2}\right) Re_{D,max}^{a3} Pr_f^{a4} \tag{87}$$

The coefficient A and exponents $a1$, $a2$, $a3$, and $a4$ are represented in Table 11.

As the latent heat due to condensation released in the TMC domain and transfer through membrane to the cooling water, the following TMC average convection-condensation Nusselt number correlation $\overline{Nu}_{cond-conv}$ is proposed:

$$\overline{Nu}_{cond-conv}^{corr} = B_1\, N_R^{b1} (\mathcal{X})^{b2} \left(B_2 + \left(\frac{S_T}{S_T - d_o}\right)^{b3}\right) Re_{D,max}^{b4} Pr_f^{b5} \tag{88}$$

where $\mathcal{X}$ is the dimensionless water vapor condensation effect at the outer surface of the nanoporous tube on the total heat transfer and is given by:

$$\mathcal{X} = \frac{\dot{m}_v\, \varepsilon\, L}{\rho \Gamma\, A_{sur} V_{fg,in}} \tag{89}$$

Where Γ is the membrane tortuosity.

$$\dot{m}_v = (water\ vapor\ wt.\%) * \dot{m}_{fg} \tag{90}$$

$$A_{sur} = 2\pi \left(\frac{d_o}{2}\right) L \tag{91}$$

The $\overline{Nu}_{cond-conv}^{corr}$ correlation considered Nusselt number from the sensible heat and latent heat and also considered the effect of the condensation and membrane properties, N_R, tube diameter, and sensible heat and latent heat. The coefficient B_1 and B_2 and the exponents $b1$, $b2$, $b3$, $b4$, and $b5$ are represented in Table 12.

For both proposed correlations, Equations 87 and 88, the coefficients, and exponents were determined based on reducing the square standard deviation, SSD, between the correlated data and the simulated (CFD) data using the power law with Microsoft Excel. It should be mentioned that the power law builds the exponents and/or coefficients based on how the given parameters affect the numerical results and keep the expected/correlated results very close to the simulated results. Those correlations are derived accurately based on the geometrical parameters and operating conditions used in the simulation, which were previously defined in the dissertation, within a limited number of exponents and coefficients, defined in Tables 9 and 10. The Nusselt numbers are correlated to the Reynolds number, Prandtl number, and tube spacing by a power law. The exponent of the Reynolds number varied between 0.482 -0.597 for Eq. 23 and 0.302-0.55 for Eq. 24 based on the Reynolds number range and the dimensionless tube spacings. The condensation effect was introduced for the first time in $\overline{Nu}_{cond-conv}$ correlation. This correlation related the Nusselt number to the dimensionless water vapor condensation coefficient, $\mathcal{X}$, which was derived as accurately as possible based on the tube surface area, flue gas conditions, and water vapor content.

Table 11. Coefficient and Exponents of the TMC Convection Nusselt Number Correlation, $\overline{Nu}_{conv}^{corr}$.

Reynolds number	S_t/d_o	A_1	A_2	a1		a2	a3	a4
$Re_{D,max} \leq 1 \times 10^3$	>2.0	0.26	0.05	$N_R < 16$	0.025	0.15	0.565	0.3
				$N_R \geq 16$	0.021			
	<2.0	0.305	0.02	0.015		0.10	0.597	0.3
$1 \times 10^3 < Re_{D,max} 9 \times 10^3$	>2.0	0.230	0.01	0.133		1.06	0.482	0.3
	<2.0	0.157	0.72	0.494		1.86	0.482	0.3

Table 12. Coefficient and Exponents of the TMC Average Convection-Condensation Nusselt Number Correlation, $\overline{Nu}_{cond-conv}^{corr}$.

Reynolds number	S_t/d_o		B_1	B_2	b1	b2	b3	b4	b5
$Re_{D,max} \leq 1 \times 10^3$	>2.0	$N_R < 16$	0.23	0.0086	0.2	0.114	1.12	0.55	0.3
		$N_R \geq 16$	0.58		0.01	0.267			
	<2.0	-	0.33	0.0087	0.2	0.027	0.556	0.507	0.3
$1 \times 10^3 < Re_{D,max} \leq 9 \times 10^3$	>2.0	-	0.355	0.013	0.16 5	0.053	1.166	0.456	0.3
	<2.0	-	0.804	0.013	0.2	0.034	1.42	0.302	0.3

The proposed TMC correlations show good agreement with numerical Nusselt numbers. Figure 41 and Figure 42 represent the predicted (correlated) values versus the simulated data. The results in these figures considered the results of N_R ranges, Reynolds number ranges, and tube diameter ranges represented in Figures 39 and 40. It can be seen that the relative differences of predicted (correlated) Nusselt numbers against the TMC simulated average convective Nusselt numbers are below 15% similar to the average condensation-convection Nusselt number. Therefore, the underlying flue gas heat transfer inside the

TMC is well predicted with the new correlations, Eq. 87-88, compared to the single-phase flow correlations developed previously in the literature. The correlations predict 95.3% and 96% of the simulated data, respectively, for average convective Nusselt numbers and average condensation-convection Nusselt numbers of the simulated data within ±10%.

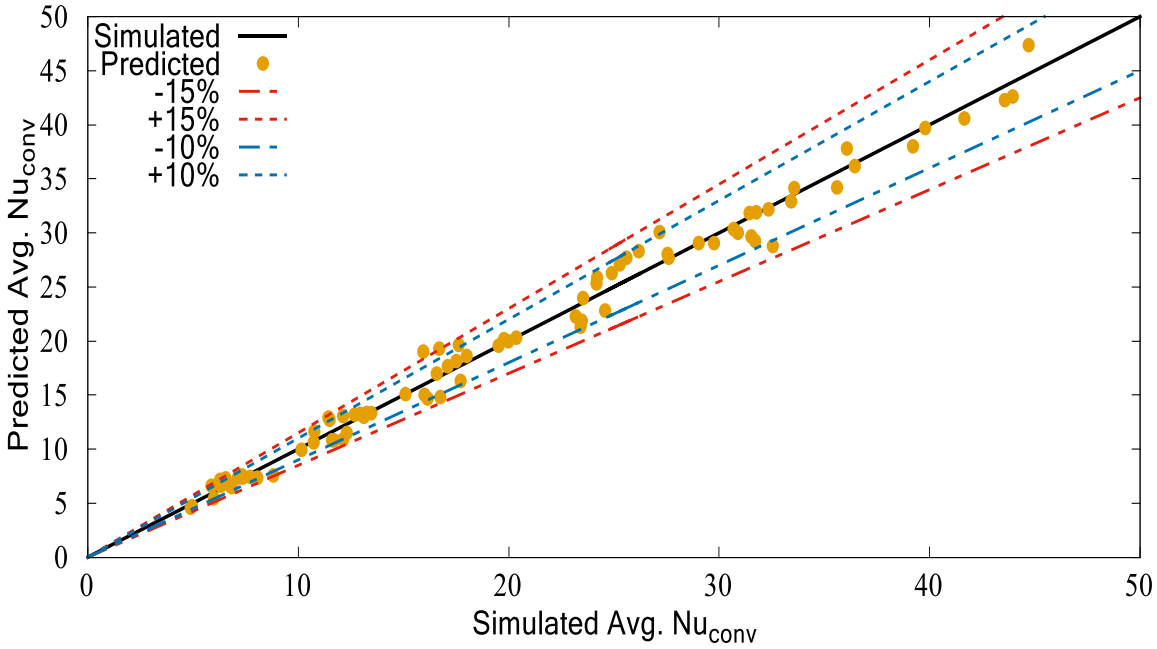

Figure 41: Predicted (c Correlated) Values Versus Simulated Data (CFD Results) for the Average Convective Nusselt Number, $\overline{Nu}_{conv}$.

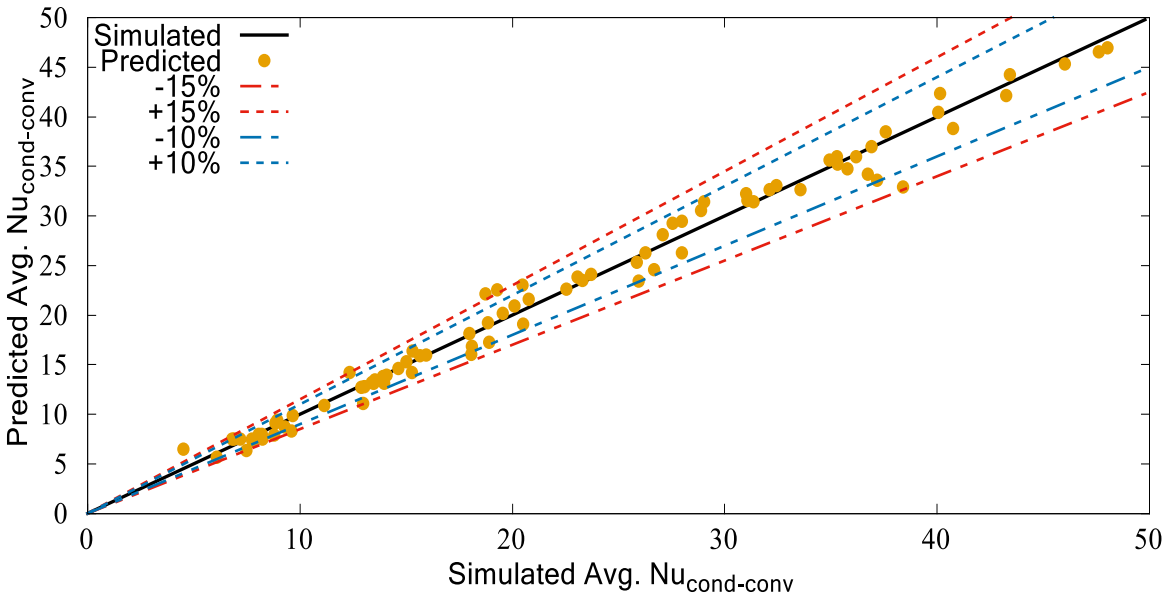

Figure 42: Predicted (Correlated) Values Versus Simulated Data (CFD Results) for the Average Condensation- Convection Nusselt Number, $\overline{Nu}_{cond-conv}$.

5.2. Pressure Drops (Hydraulic Resistance) Correlations

Previous research and experimental results summarize that the pressure drops across the tube bundle are related to the flow velocity, physical properties, N_R , and tube arrangement. The total pressure drop inside the tube bundle is described by the hydraulic resistance and is considered one of the most important attributes that impact the design of the heat exchanger. The Euler number and friction factor usually represent hydraulic resistance inside the tube bundle.

In the following sections, the flue gas pressure drop inside the TMC tube bundles was calculated for different tube N_R, tube diameters, and Reynolds numbers and was compared to the single-phase (no condensation) flow correlations developed previously in the

literature by Holman-Jakob and Gunter-Shaw. Also, a new correlation for the TMC friction factor was proposed and derived in Section 4.3.3.

The Holman-Jakob model [75], introduced in 1938, relates the pressure drop across a tubes bank by the following relation:

$$\Delta p = \frac{G_{max}^2 N_R}{\rho\left({}^{g}/_{2}\right)}\left(\frac{\mu_w}{\mu}\right)^{0.14}\left(0.25 + \frac{0.118}{\left(\frac{S_T - d_o}{d_o}\right)}\right) Re_{D,max}^{-0.16} \tag{92}$$

Where $[\Delta p] = {}^{Ibf}/_{ft^2}$ in English units.

The Gunter-Shaw model [76] was published in 1945 and implements a piecewise friction factor correction based on the Reynolds number of the flow.

$$\Delta p = \frac{f}{2}\frac{1}{g}\left(\frac{\mu_w}{\mu}\right)^{0.14}\left(\frac{D_h}{S_T}\right)^{0.4}\left(\frac{S_L}{S_T}\right)^{0.6}\left(\frac{G^2 l}{D_v \rho}\right) \tag{93}$$

The friction relation, $\frac{f}{2}$, of Gunter and Shaw is present as follows:

$$\frac{f}{2} = \begin{cases} 90Re^{-1} & Re \leq 200 \\ 0.96Re^{-0.145} & Re > 200 \end{cases} \tag{94}$$

Figure 43 represents the pressure drop inside the TMC tube bundle compared to the single-phase flow correlations developed by Holman-Jakob [75] and Gunter-Shaw [76]. The increase in N_R and Reynolds numbers increases the pressure drop inside the TMC tube bundle. At a low Reynolds number, the pressure drop inside the TMC tube bundle is close to that predicted from the correlation. However, as the Reynolds number increases, the TMC pressure drop diverges from that predicted by the correlations. For N_R= 6, both

correlations overpredict the pressure drops inside the TMC tube bundle. Reducing N_R increases the deviation from the correlations. For instance, for N_R=6 the Gunter-Shaw model [76] diverges from the TMC results with an error range 22% up to 827% for the given Reynolds number. The error range for the Holman-Jakob model [75] in all cases were over 30% and at some point, reach up to 262% It should be noted that the Gunter-Shaw correlation is not a function of N_R and could not link the relationship between the pressure drop and the number of rows. This requires changing the existing correlations by adding/modifying the term related to the effects of the N_R on the pressure drops. Although both correlations are a function of tube hydraulic diameter, decreasing the tube diameter increases the deviation between TMC numerical results and correlations results. For all cases, the effect of the Reynolds number on the pressure drop shows a similar trend as it compared with the correlations.

The effect of the variation of the tube diameter on the pressure drops was compared with the single-phase correlation with respect to the function of the Reynolds number. The results are represented in Figure 44. The results showed a significant change in the pressure drops as the tube diameter changed. At d_o = 7.62 mm, the pressure drops of the TMC were in good agreement with the Gunter-Shawn model, with a maximum error of about 19%, except for the first point where the friction relation, $\frac{f}{2}$, was evaluated at Re < 200 the error was 53. A slight divergence from the Holman-Jacob model could result in a minimum error of 30%. However, decreasing the tube diameter increases the difference between the pressure drop in the TMC and that calculated using the correlation. For d_o = 6.35 mm, 5.49 mm, and 4.57 mm, the Gunter-Shawn model showed better agreement than the Holman-

Jacob model. However, the error percentage for these tube bundles exceeds 35% and reaches more than 200% for Gunter-Shaw model. Based on these results, the correlation in most of the studied range of parameters deviates significantly from those obtained numerically using the TMC tube bundle. Based on that, define a new correlation that can predict the TMC pressure drop will be provided in the following Section.

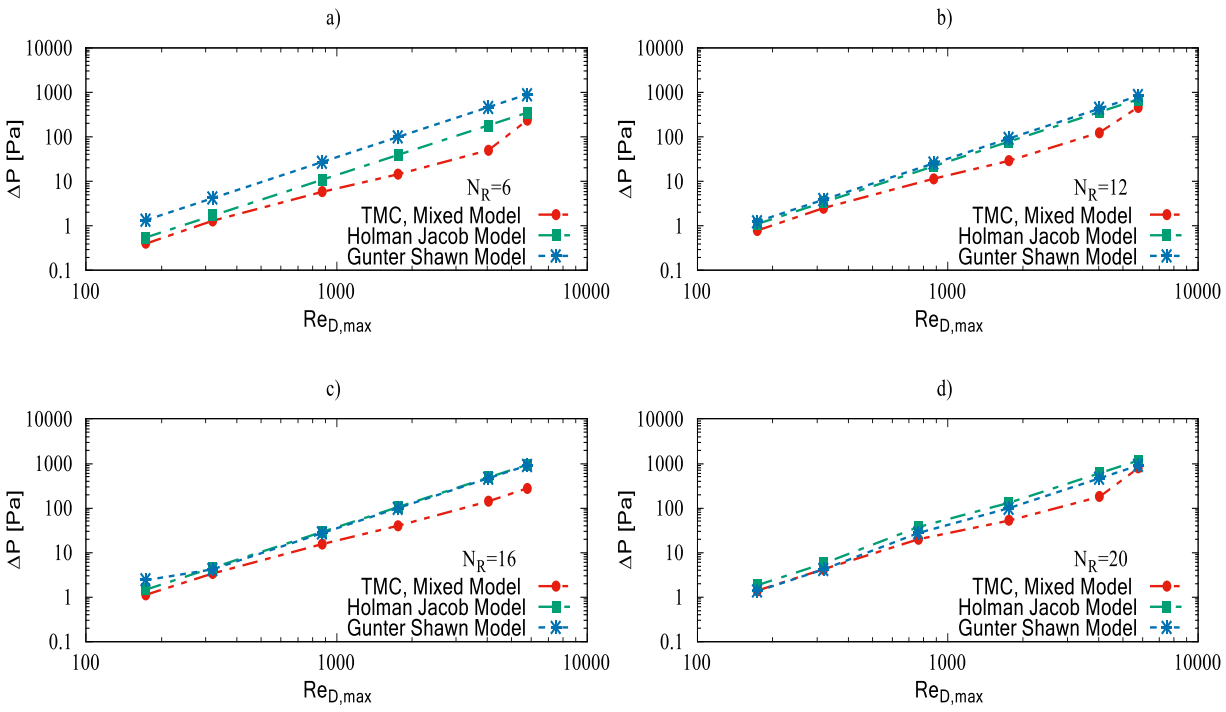

Figure 43. The Variation of the Pressure Drops Inside TMC Staggered Tube Bundle Compared to the Previously Developed Single-Phase Correlations for Different Number of Rows: (a) N_R = 6 rows, (b) N_R = 12 rows, (c) N_R = 16 rows, and (d) N_R = 20 rows with tube bundle do = 5.49 mm.

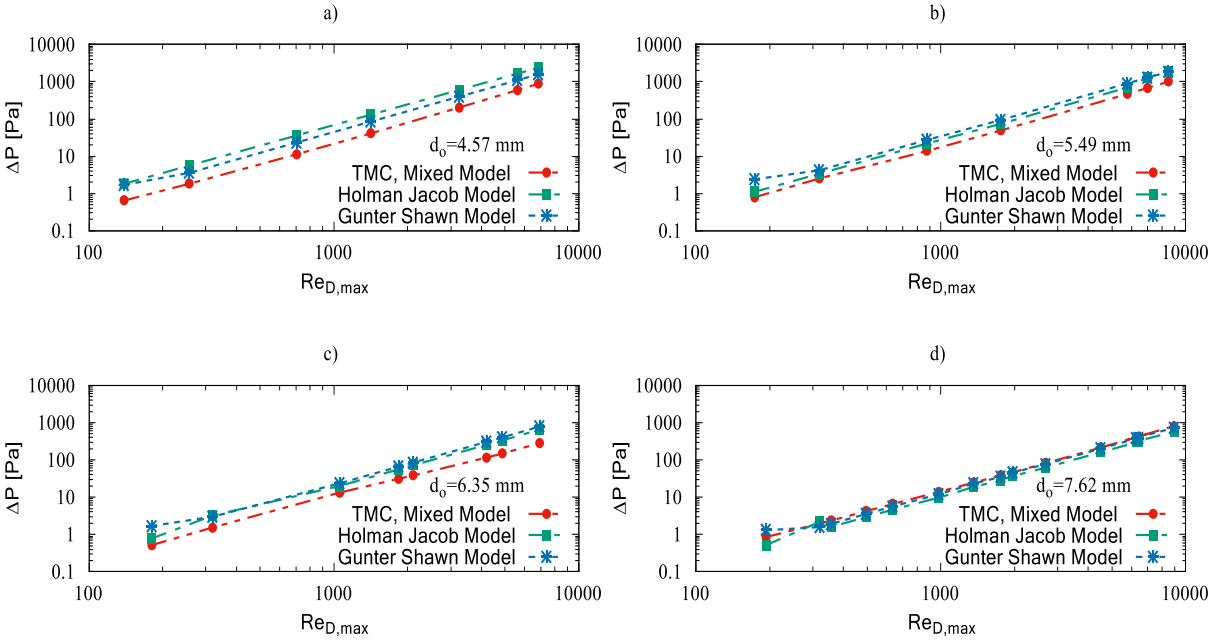

Figure 44: The Pressure Drop Inside TMC staggered tube bundle compared to the Previously Developed Single-Phase Correlations for Different Tubes Diameter: (a) d_o= 4.57 mm, (b) d_o= 5.49 mm, (c) d_o= 6.35 mm, and (d) d_o= 7.62 mm with N_R=12.

5.2.1. Proposed correlation of TMC Friction Factor

Based on the analysis provided in the previous Section, the single-phase correlations diverge significantly from the TMC pressure drops. The following TMC friction factor correlation, $f^{correlated}$, is generated based on the current numerical study and within the examined parameters:

$$f^{correlated} = D_1\left(-D_2 + Re_{D,max}^{-d1}\right)\left(\frac{D_h}{S_T}\right)^{d2} N_R^{d3} \quad (95)$$

The coefficients D_1 and $D_2$and exponents are given in Table 13.

Table 13: Coefficient and Exponents of the TMC Friction Factor Correlation.

$Re_{D,max}$	S_l/d_o	D_1	D_2	$d1$	$d2$	$d3$
$10^2 < Re_{D,max} \leq 3 \times 10^3$	< 1.5	0.84	0	0.243	0	0.004
	> 1.5	4.66	0.863	0.0173	1.173	0.0532
$3 \times 10^3 < Re_{D,max} \leq 9 \times 10^3$	< 1.5	0.0089	0.003	0.115	0	0.584
	> 1.5	0.0089	0.01	0.032	4.95	0.04

The proposed TMC friction factor correlation considered the effect of the membrane tube diameter and spacing as well as the N_R of the tube bundle. The TMC friction factor correlation shows good agreement with the TMC numerical results, as shown in Figure 45. The corresponding differences are reduced by reducing the sum of the square standard deviation SSD between the correlated data and the numerical data, 96% of the relative differences of predicted (correlated) friction factor against the TMC simulated friction factor is within ±15%. Therefore, a hydraulicly developed flow inside the TMC is better predicted with the new correlation, Equation 95, compared to the single-phase flow correlations developed previously in the literature.

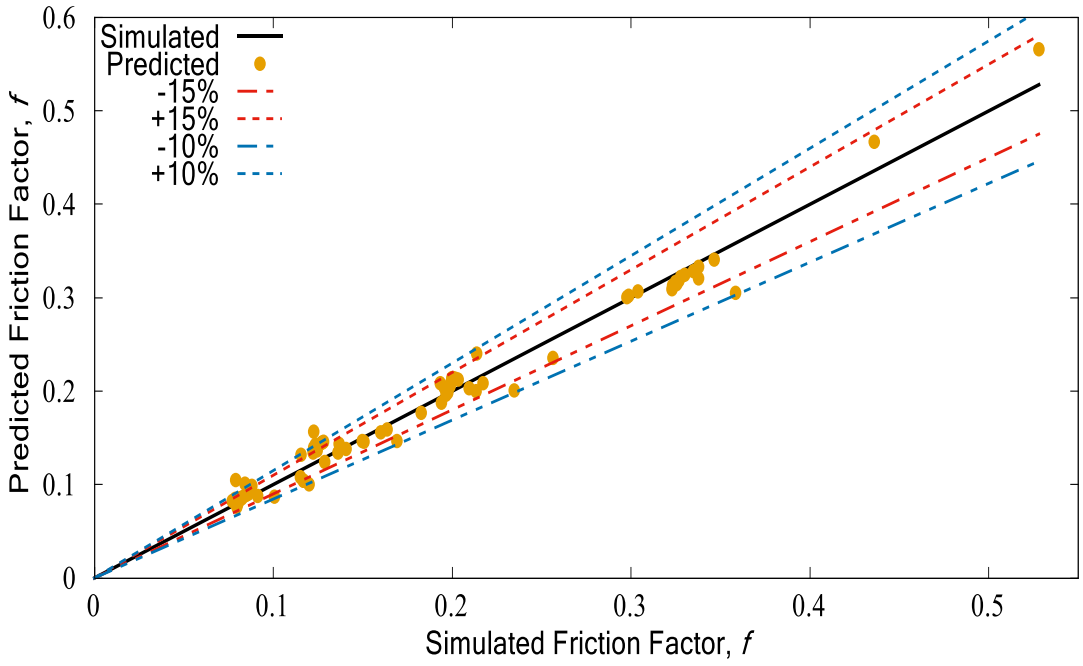

Figure 45. Predicted (Correlated) Values Versus Simulated Data for Friction Factor.

In summary, it was found that except for selected conditions, the single-phase correlations were noticed to differ from the TMC numerical results. Empirical TMC correlations for heat transfer and pressure drops with respect to condensation rate, number of rows, and the nanoporous membrane geometrical properties were derived thereby for flue gas. The effects of the tube diameter, number of rows, Reynolds number, and condensation rate and other membrane geometrical parameters were considered in the proposed correlations. The correlations show good agreement for all investigated parameters$\overline{Nu}_{conv}$, $\overline{Nu}_{cond-conv}$, and friction factor, within errors of ±10%, ±10%, and ±15%, respectively. The correlations can be used to estimate the heat transfer and pressure drop during the design of transport membrane-based heat exchangers.

6. CHAPTER VI: MULTIPHASE MODELING OF HEAT AND MASS TRANSFER INSIDE TMC TUBE BUNDLE

Most of the simulation studies on the heat and mass transfer of TMC tube bundle were conducted based on the assumption that all the condensate water vapor is recovered and transported to the cooling water through the porous membrane, which means the condensate water vapor is equal to the transported water. Recently, the experimental work of [56] on the macroporous ceramic membrane revealed that the ceramic membrane could not completely recover all the condensate under different operating conditions. They found that part of the condensate on the outer surface of the ceramic membrane drops into the flue gas and drains out as an acidic liquid after reacting with SO_2. The existence of the acidic liquid in the tube bundle can harm the heat exchanger. Also, mixing the condensate with fine particles could block the pores of the porous membrane and causes membrane fouling, which reduces the porous membrane's performance.

In addition, the previous literature reveals that the reported numerical models in the literature focused on studying heat and mass transfer using the single-phase multi-species model. However, the condensation inside the TMC tube bundles affects the flow turbulence and phase dynamics, which emphasizes the need to study the flow inside the TMC using the multiphase model. Therefore, modelling the TMC tube bundle using a multiphase flow approach can provide information that cannot be obtained by using the single-phase model. The multiphase model can calculate the possible amount of condensate water inside the

flue gas domain, which is based on the flue gas temperature and vapor content as well as ceramic membrane tube wall temperature.

For the first time, this dissertation will report a multiphase modeling of heat and mass transfer inside the TMC-based heat exchanger. The previous chapters were focused on modeling the heat and mass transfer using the single-phase model regardless of the actual phase change occurred in the domain. Also, the most reasonable example in the literature akin to this situation is a case mentioned earlier in this dissertation, but it was related to a different type of multiphase flow inside porous material, not a TMC. In this chapter, a multiphase simulation has been conducted to investigate TMC multiple tubes by applying the multiphase VOF model, species transport model, and $SST\ k-\omega$ turbulence model. The Lee (evaporation-condensation) model is applied as a source term in the main governing Equations.

6.1. Methodology and Theory

Multiphase flow modeling (two-phase flow) is an interesting and attractive topic to model the gas-liquid two-phase flow inside the heat exchanger. The flow inside the transport membrane condenser is a typical multiphase flow due to the phase change of water vapor at the outer surface of the nanoporous tube. Three different multiphase models are available in Ansys/Fluent 2021 R1: the mixture model, the VOF model, and the Eulerian model. The two most popular models are the Volume of Fluid (VOF) model and the Eulerian model. The mathematical formulations of these models cause differences in their accuracy, convergence, computational time. Table 14 represents the major differences between the two models. Also,

Guerrero et al. [94] compared the Eulerian model with VOF model to choose the appropriate model for multiphase flow simulation in a vertical pipe, they concluded that the Eulerian model is required more computational time as compared to the VOF model for the same computational mesh. However, the Eulerian model was independent of the mesh size and would spend less time if a mesh with a lower number of cells. Also, they concluded that the VOF model was capable of distinguishing the continuous and discontinuous phases in the solution visualization and predicting the experimental results better.

Table 13: Major differences between the Eulerian model and Multiphase model

VOF Model	Eulerian Model
• Solve single momentum equation and energy equation for all phases throughout the domain, the phases are sharing the velocity field. • Evaluate the material properties based on the presence of the component phases in the control volume • The VOF model treats energy, *E*, and temperature, *T*, as mass-averaged variables • The properties ρ and μ is dependent on the volume fractions of all phases. • Less CPU and simulation time	• Model a multiple separate set of equations for each phase. The phases interact and can be any combination of liquids, gases, or solids. • All phases are shared by a single pressure. • While solving the continuity and momentum for each phase. • Used volume fractions theory which based on the space occupied by each phase, and the laws of conservation of mass and momentum are satisfied by each phase individually. • More simulation time and CPU

The basic model of Eulerian and VOF model (no condensation neither transport model was considered at that time) were used to run the simulation to evaluate the outlet flue gas temperature of a staggered tube bundle, the results represented in Figure 46. According to these results and based on the computational time spent on these results, the VOF model was adopted for further investigation in the current study.

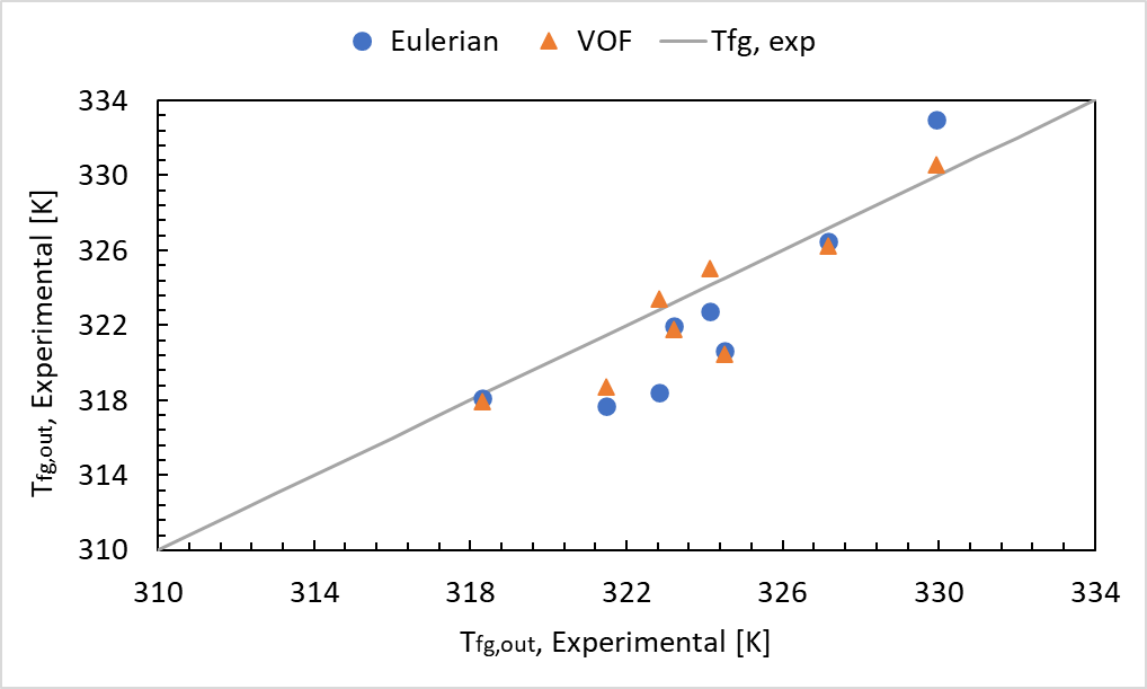

Figure 46: Numerical Outlet Flue Gas Temperature Compared with the Experimental Results for the Multiphase Eulerian Model and VOF Model.

6.1.1. VOF multiphase model

The VOF method can capture the interface between the phases easily [92]. The theoretical formulation of the VOF model is based on the assumption that each cell in the computational domain is filled by one phase or a combination of two-phases. The VOF solves a single set of momentum Equations to track the volume fraction of each phase. The VOF evaluates the material properties based on the presence of the component phases in the control volume. For example, in the two-phase model, the volume fraction of one phase is tracked and the density in each cell is calculated by:

$$\rho = \alpha_2 \rho_2 + (1 - \alpha_2)\rho_l \tag{87}$$

The volume-fraction-averaged density, ρ, and viscosity, μ, for the n-phase system are in the following form:

$$\rho = \sum_1^q \alpha_q \rho_q \qquad \text{and} \qquad \mu = \sum_1^q \alpha_q \mu_q \tag{88}$$

The properties ρ and μ are dependent on the volume fractions of all phases. In the case of multiphase flow, the fluid interactions and dynamics are described by the mass conservation within the control volume. The mass conservation depends on the phase's volume fraction. In our case, the phase change occurs between two vapor and liquid phases. In the mass conservation Equation, described below, for the second phase "q", the volume fraction is associated with the convective, transient, and source terms.

$$\frac{1}{\rho_q}\left[\frac{\partial}{\partial t}\left(\alpha_q \rho_q\right) + \nabla.\left(\alpha_q \rho_q \vec{u}_q\right) = S_{\alpha q} + \sum_{p=1}^{n}\left(\dot{m}_{pq} - \dot{m}_{qp}\right)\right] \tag{89}$$

$$\sum_{q=1}^{n} \alpha_q = 1 \tag{90}$$

where $\dot{m}_{qp}$ is the mass transfer from phase q to phase p, and $\dot{m}_{pq}$ is the mass transfer from phase p to phase q. Additional sources, $S_{\alpha q}$, in the conservation Equation were introduced to model the mass transfer between the phases. The VOF model solves a single momentum Equation and energy Equation for all phases throughout the domain, and the phases share the velocity field. The momentum and energy Equations used in VOF model are:

$$\frac{\partial}{\partial t}(\rho\vec{v}) + \nabla.(\rho\bar{u}\bar{u}) = -\nabla p + \nabla.[\mu(\nabla\bar{u} + \nabla\bar{u}^T)] + \rho\vec{g} + \vec{F} \quad (91)$$

$$\frac{\partial}{\partial t}(\rho E) + \nabla.\left(\bar{u}\,(\rho E + p)\right) = \nabla.\left[k_{eff}\nabla T\right] + S_h \quad (92)$$

The VOF model treats energy, E, and temperature, T, as mass-averaged variables:

$$E = \frac{\sum_{q=1}^{n} \alpha_q \rho_q E_q}{\sum_{q=1}^{n} \alpha_q \rho_q} \quad (93)$$

where E_q for each phase is based on the specific heat of that phase and the shared temperature. The properties ρ and k_{eff} are shared by the phases. The heat source S_h is calculated from the interfacial mass transfer rate per unit volume, multiplied by the latent heat. The interfacial mass transfer rate is due to the phase change that occurs inside the TMC domain and is calculated from Lee's model presented below, Section 6.2.4.

The interfacial force effect between the water vapor and liquid was included by adding the $\vec{F}$ to the momentum Equation and turning on the continuous surface force in the fluent. The value of surface tension value is calculated using this formula [112]:

$$\sigma = 0.09805856 - 1.845\ \times 10^{-5}\mathrm{T} - \ 2.3 \times 10^{-7}T^2 \quad (94)$$

6.1.2. Turbulence model

The turbulence inside the TMC tube bundle was modeled using shear stress transport SST $\mathrm{k} - \omega$. The SST $\mathrm{k} - \omega$ was selected to meet the requirements of the generated mesh

with Y_{plus} less than 2. The transports Equations of the turbulence kinetic energy k, and dissipation rate ω are defined in Chapter 2.

6.1.3. Multiphase species transport model

The flue gas comprises multispecies with different mass fractions in wt.%, H_2O= 11.4, CO_2= 4.0%, N_2= 75.6%, and O_2= 9.0%. The multi-species transport model can be applied to multiphase flows. The conservation Equations for chemical species in multiphase flows, for each phase q, predict the local mass fraction of each species, Y_i^q, by solving a convection-diffusion Equation for the i^{th} species. The general conservation Equation for chemical species, when applied to a multiphase mixture, flue gas in our case, is defined as:

$$\frac{\partial}{\partial t}\left(\rho^q \alpha^q Y_i^q\right) + \nabla.\left(\rho^q \alpha^q \vec{u}^q Y_i^q\right) = -\nabla.\,\alpha^q J_i^q + \alpha^q S_i^q + \sum_{p=1}^{n}\left(\dot{m}_{p^i q^i} - \dot{m}_{q^i p^i}\right) \qquad (95)$$

where $\dot{m}_{p^i q^i}$ is the mass transfer source between species *I* and *j* from phase *q* to *p*, and S_i^q is the creation rate by addition from the user-defined function.

6.1.4. Phase change (Lee's) model

The most popular phase change model is the condensation-evaporation model named Lee model [112]. The Lee model is able to detect the phase change along the phases interface and within the saturated phase. The Lee model assumed the phase change occurs at the quasi-thermo-equilibrium state and at a constant pressure. The current study adopted the Lee model to track the condensation of the water vapor from the flue gas. The mass transfer model is custom-built and programmed as a user-defined function (UDFs). The UDFs are integrated

into the ANSYS/Fluent 2021 R1 computer software for condensation simulations. Consequently, the related source term $S_{\alpha q}$ can be defined as follows:

$$S_{\alpha q} = r_l \alpha_l \rho_l \frac{(T_1 - T_{sat})}{T_{sat}}, \quad \text{Evaporation process if} \quad T_1 \geq T_{sat} \tag{96}$$

$$S_{\alpha q} = r_v \alpha_v \rho_v \frac{(T_1 - T_{sat})}{T_{sat}}, \quad \text{Condensation process if} \quad T_1 < T_{sat} \tag{97}$$

The values of r_l and r_v are used to avoid the divergence problem and to maintain the interfacial temperature between the phases close to the saturation temperature. Different values of the coefficients r_l and r_v were used in the literature to maintain the interface temperature at the saturation temperature. In the numerical simulation of Yang et al. [92], the r values were set to 100 s^{-1}. Sandra et al. [95] used an r value of 0.1 s^{-1} to simulate the flow boiling process of a hydrocarbon feedstock. Based on the works of Lee [112] and Wu et al. [113], too-large values of the r_l and r_v may cause numerical convergence, while minimal values cause a considerable variation between the saturation temperature and the interfacial temperature. They used a value of 0.1 for both r_l and r_v in their simulation. In the current study, the convergence was reached using values of 0.1 s^{-1} for r_l and r_v.

The following relation was implemented in the UDF and used to calculate the water vapor condensate percentage out of all the water vapor from flue gas inside the flue gas domain by using the following relation:

$$\text{Condensation \%} = \frac{S_{aq} * cell\_volume}{(water\ vapor\ mass\ fraction\ wt.\%) * \dot{m}_{fg}} \quad (98)$$

6.1.5. Water transport model

The transport of the condensate water through the porous media was modeled using the Darcy law model [85, 106, 114, and 115] written in the user-defined functions (UDF's) in the computational fluid dynamic code Ansys/fluent. The model is capable of detecting the existence of the water liquid at the nanoporous membrane wall and inside the flue gas domain. The Darcy law is defined as:

$$Q = -\varepsilon \rho A \frac{K_l}{\mu_l} \frac{\partial (P - P_c)}{\partial s} \quad (99)$$

$$Q = -\varepsilon \rho A \frac{K_l}{\mu_l} \frac{\Delta P}{\Delta s} + \varepsilon \rho A \frac{K_l}{\mu_l} \frac{\Delta P_c}{\Delta s} \quad (100)$$

The first term in Equation (100) is the water diffusion due to pressure difference, and the second term is the water diffusion due to the capillary pressure. Where, Q is the liquid mass flow rate [kg/s], ρ_l is the liquid density, and $\frac{K_l}{\mu_l}$ is the permeability of the porous layer [m^2/pa.s]. K_l [m^2] is the liquid permeability of the nanoporous material, and μ_l is liquid dynamic viscosity [pa.s].

Capillary flow is due to the difference between the relative attraction of the molecules of the liquid for each other and for those of the solid. A familiar example is the rise of water in an open tube of a small cross-section. As the radius becomes very small, capillary rise

increases significantly. The liquid flux in pores is modeled through capillary pressure difference that can be modeled by the Young Laplace Equation:

$$\Delta P_c = -\frac{2\sigma cos\theta}{r_p} \tag{101}$$

where θ is the equilibrium contact angle of the liquid on the solid, and r_p is the radius of the pore.

The detailed derivation of the capillary pressure difference in the nanopores, which was modeled using the Kelvin Equation, is represented in Chapter 2. The final form of the capillary pressure is defined by Equation (63) in Chapter 2.

The porous permeability, K_l, to the water liquid was calculated using the following Equation, [11]:

$$k_l = \frac{\varepsilon d_p^2}{72(1-\varepsilon)^2\tau} \tag{102}$$

where d_p is the pore diameter of the porous medium.

Figure 47 represents the multiphase approach for modeling a single tube of TMC and the corresponding different domains were involved in the simulation.

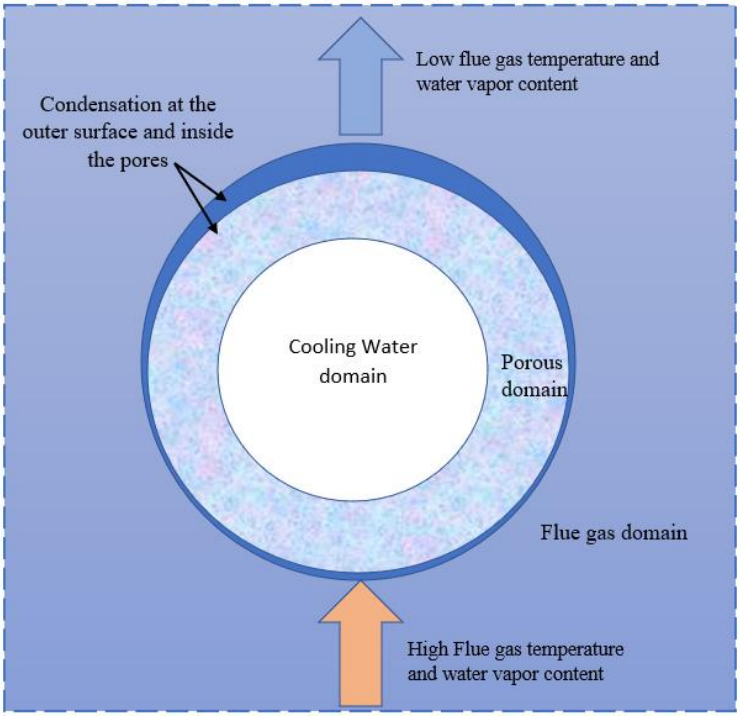

Figure 47: Multiphase Approach for Modeling Single Tube of TMC

6.1.6. Solver Settings

The volume of fraction Equation may be solved either through implicit or explicit time discretization. In this study, the implicit scheme has been used to track the phase at the porous membrane surface. The pressure-velocity is coupled using the coupled algorithm, the momentum and energy are solved using the second-order upwind scheme, and the pressure and volume fraction are solved using PRESTO and Modified HRIC discretization. These schemes are used to obtain the face fluxes for all cells, including those near the interface. The continuity Equation discretization is defined as:

$$\frac{\alpha_q^{n+1}\rho_q^{n+1}-\alpha_q^n\rho_q^n}{\Delta t}V+\sum_f\left(\rho_q^{n+1}U_f^{n+1}\alpha_{q,f}^{n+1}\right)=\left[S_{\alpha q}+\sum_{p=1}^{n}\left(\dot{m}_{pq}-\dot{m}_{qp}\right)\right]V \qquad (103)$$

where $n+1$, n, V, $\alpha_{q,f}$, and U_f are index for the current time step, the index for the previous time step, the volume of the cell, the face value of the q^f volume fraction computed from the Modified HRIC scheme, and volume flux through the face based on normal velocity, respectively.

Since this Equation requires the volume fraction values at the current time step (rather than at the previous step, as for the explicit scheme), a standard scalar transport Equation is solved iteratively for each of the secondary-phase volume fractions at each time step.

The adaptive time step *dt* is controlled to maintain the Courant number CFL at a specified value. The relation between the Courant number and the time step is given as:

$$CFL = \frac{\Delta t}{\Delta x/|\vec{v}|} \tag{104}$$

where Δt is the time step, Δx is the grid size and $|\vec{v}|$ is the fluid velocity. The coupled scheme of discretization is used for coupling the pressure and velocity. The second-order upwind scheme was used to solve the momentum and energy Equations, and the Modified HRIC and PRESTO discretization schemes were used to solve the volume of fractions and pressure.

6.1.7. Grid Independence Study

Similar geometry and dimensions used in single-phase model analysis was used to perform the multiphase simulation. However, the grid independence study was repeated using the multiphase theoretical formulation. The mesh was prepared using the meshing tools of Ansys/workbench with hexahedral elements. The solution sensitivity to the mesh quality was

performed by increasing the mesh size from 0.22 million to 2.78 million cells. Multiple simulations were run, and it was found that the simulation results were almost the same as the grid size changed from 1.72 to 2.78 million control volumes. Figure 48 represents the mesh independence study for the TMC tube bundle, with the boundary conditions being set to V_{fg}=0.526 m/s, T_{fg}=355 K, V_w=0.05 m/s, and T_w=298 K.

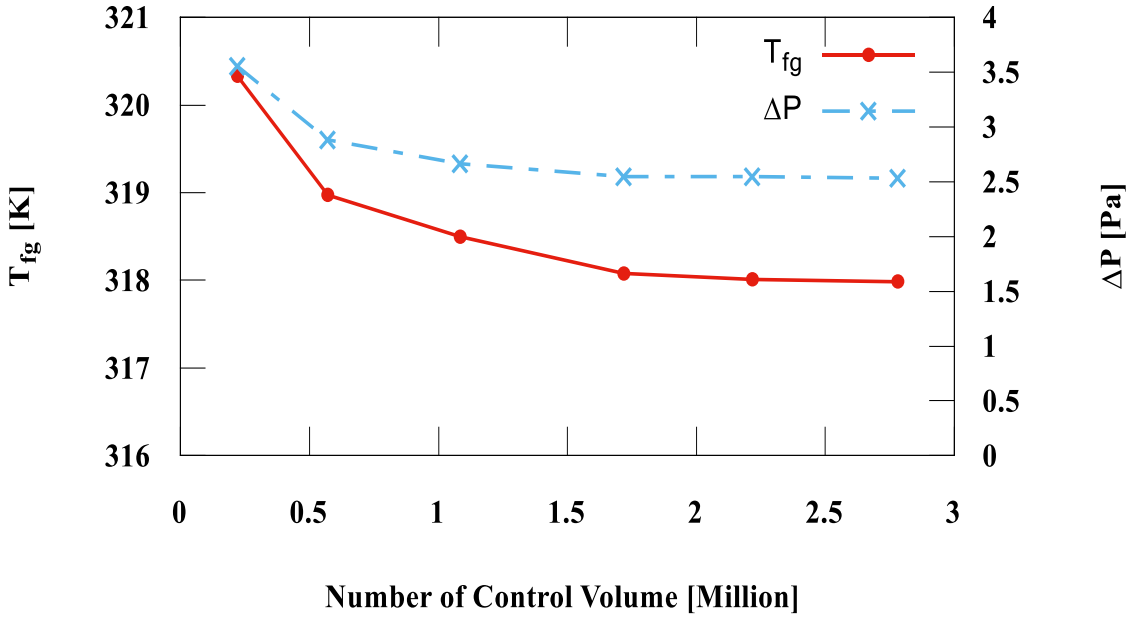

Figure 48. Mesh Independence Study.

6.2. Multiphase Model Validation

The CFD multiphase model is validated using geometry and experimental data from the available literature by GTI [28]. In their experiment, 78 TMC tubes arranged in staggered configurations were used to recover the heat and water from the flue gas of a gas power plant. The outlet flue gas temperature and outlet water temperature calculated using the

proposed model are compared with the experimental data, and the comparison results are represented in Figure 46 and Figure 47.

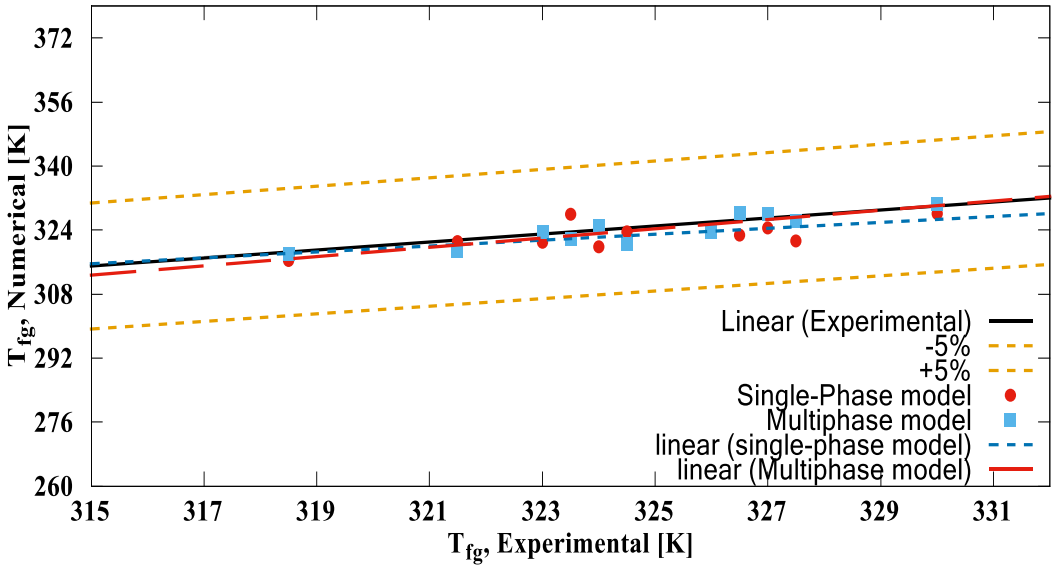

Figure 49. Outlet Flue Gas Temperature Calculated using the Multiphase Model Compared to the Experimental Data and The Single-Phase Model.

Good agreement is observed between the multiphase model and the experimental results. The error percentage for outlet flue gas temperature, Figure 49, was less than 1% for all cases except for one case of 1.25%. The error percentage for outlet water temperature, Figure 50, was less than 5% for all the cases. The Figures also compared the multiphase model with the single-phase multi-species model. In the case of the comparison with the outlet flue gas temperature, the multiphase model was closer to the experimental results than the single-phase model. It should be mentioned that the correction factors to the source terms were required in the case of using a single-phase multi-species model to reduce the

error between numerical results and the experimental data. However, the correction factors were not required in the case of using the multiphase model.

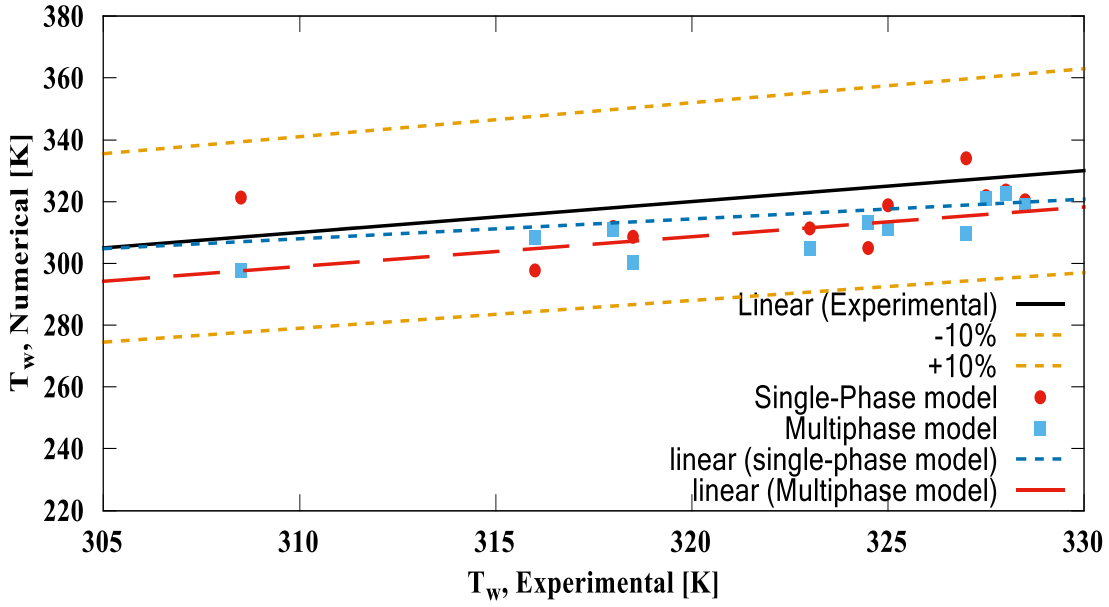

Figure 50. Outlet Cooling Water Temperature Calculated using the Multiphase Model Compared to the Experimental Data and the Single-Phase Model.

6.3. Transport Model Validation

The correction factors were added to the condensation rate calculated by the Darcy law to validate the transport model coupled with the experimental results. Previously, in modeling the single-phase condensation rate using the mixed condensation rate, the correction factor was chosen to reduce the error between the numerical model and experimental model. In the current study, dimensionless operating conditions, such as the water-flue gas velocity ratio and temperatures across the TMC-based heat exchanger, were employed to model the transported water rate. Since it was noted that the experimental condensation rate and the

dimensionless ratio of the water/flue-gas velocity and temperature follow the same trend; as the velocity ratio and LMTD increase so does the experimental condensation rate, as seen in Figure 51.

Equation 100 multiplied by the correction which builds based on the velocity ratio and LMTD, the correction factor, C_{mf} is written as:

$$C_{mf} = \left(\frac{V_w}{V_{fg}}\right)^{0.6} \left(0.09 \times \frac{(T_{fg,out} - T_{wall}) - (T_{fg,in} - T_{wall})}{\ln \frac{(T_{fg,out} - T_{wall})}{(T_{fg,in} - T_{wall})}} \right) \quad (105)$$

Figure 52 represents the numerical condensation (transported through the membrane) results of the multiphase model coupled with Darcy law and Lee phase change model, as compared to the single phase (Mixed condensation rate) and experimental condensation rate (transported). The model was implemented in Ansys/fluent using User Defined Functions (UDFs). The comparison showed that the multiphase model predicts the condensation rate better than the mixed model.

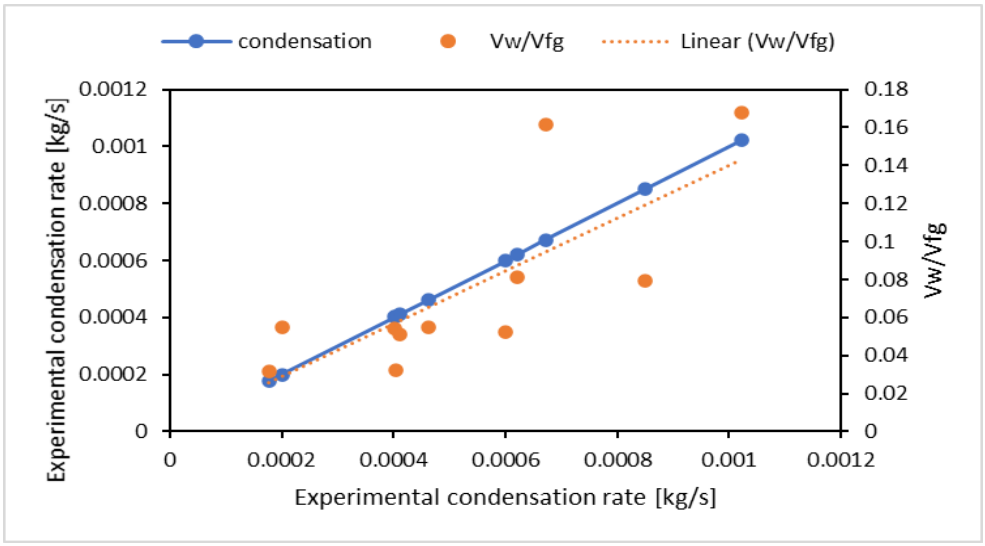

(a)

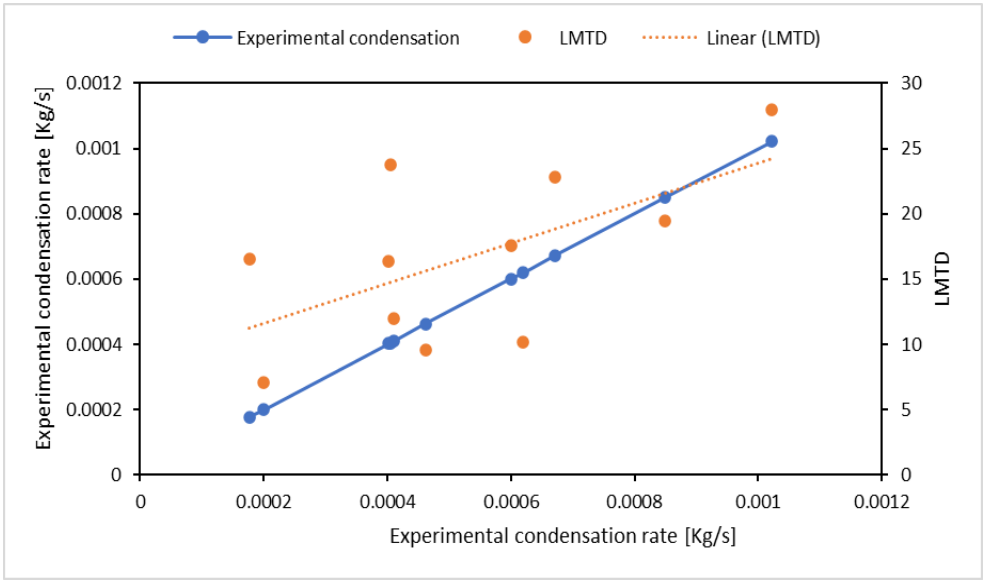

(b)

Figure 51. Relation Between the Experimental Condensation Rate and the Operating Conditions in Form of Corrections Factor to the Numerical Multiphase Model: a) Ratio of inlet velocities $\frac{V_w}{V_{fg}}$, b) Log mean temperature LMTD.

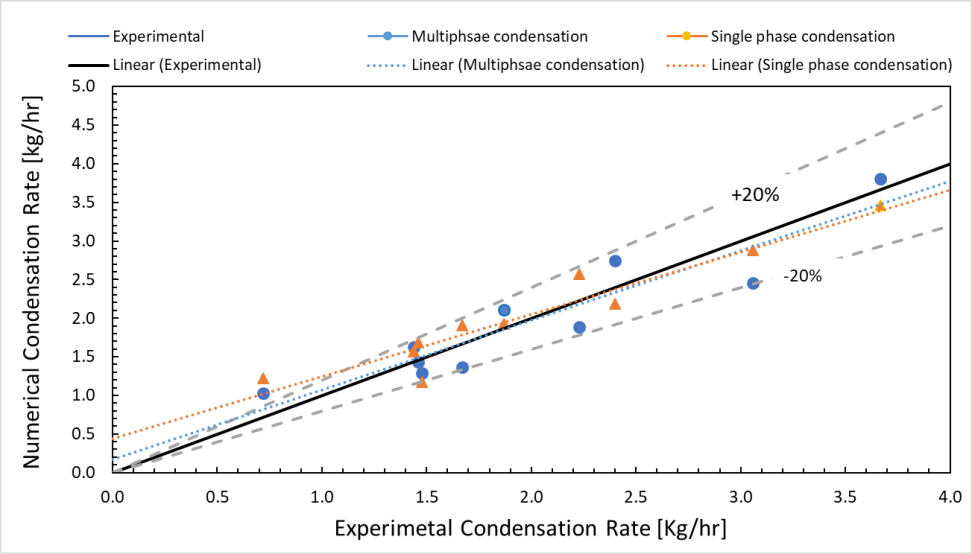

Figure 52. Comparison Between the Numerical Multiphase Condensation Rate (Transported), the Numerical Single Phase, and the Experimental Condensation Rate (Transported).

6.4. Condensation Rate Versus Transport Rate Inside the TMC

It was reported that the condensed water vapor in the TMC was transported completely in the ceramic porous membrane. Recently, researchers in [56] have reported that part of the condensed water vapor is transported by the ceramic porous membrane, but the rest is drained out with the flue gas. In the current study, the multiphase model built in Ansys/Fluent using the VOF model coupled with the condensation-evaporation Lee model has been used to calculate the possible amount of condensation of water vapor. The numerical setup and conditions used in this study replicate the reported experimental results [28]. The condensation rate using the multiphase VOF and Lee model is compared to the reported experimental results, as represented in Figure 53. The experimental results have reported a 7% to 49% condensation rate under different operating conditions. However, the numerical results showed that the condensation inside the flue gas domain

was between 21% to 81% of the amount of water vapor that exists in the inlet flue gas. Assuming the prediction is correct numerically, these results confirm that the TMC module was able to condensate water vapor under the flue gas condition inside the TMC tube bundle, more than the transport through the TMC porous membrane.

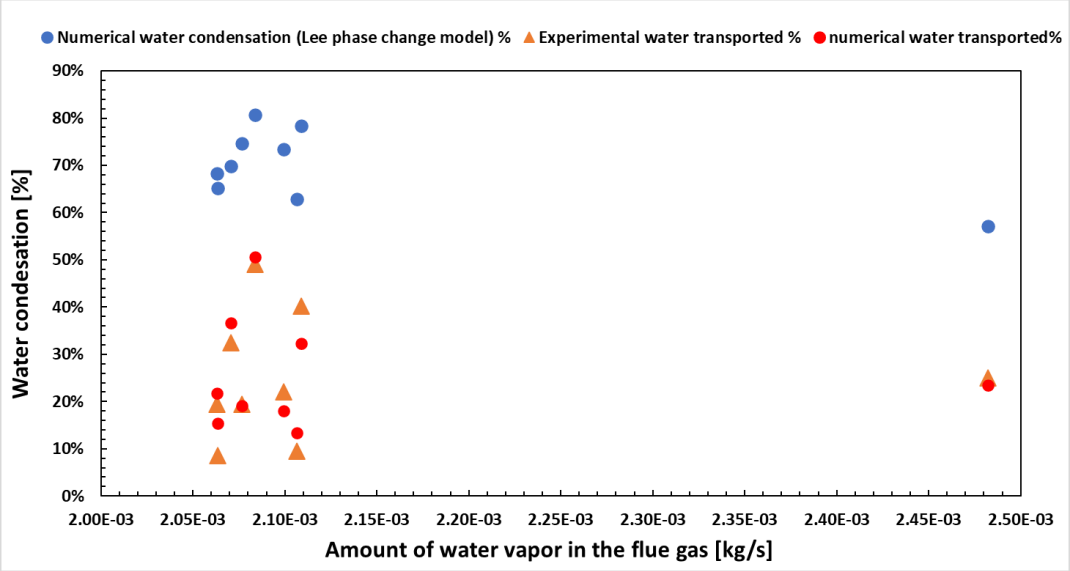

Figure 53. Percentage of Water Condensate inside the Flue Gas Domain Compared to the Experimental Transferred Water Through the Porous Media.

6.5. Multiphase Model Versus Single Phase Model Visualization

Although the multiphase model required more simulation time and CPU hours compared to the single-phase model, it has an advantage over the single phase due to its capability to model fluid flow, phase change, and mass transfer inside the porous membrane wall. The multiphase model can model the fluid flow and mass transfer as illustrated in Figure 54, while the single-phase model treats the membrane wall as a solid wall and no mass transfer and fluid flow are resolved in that area.

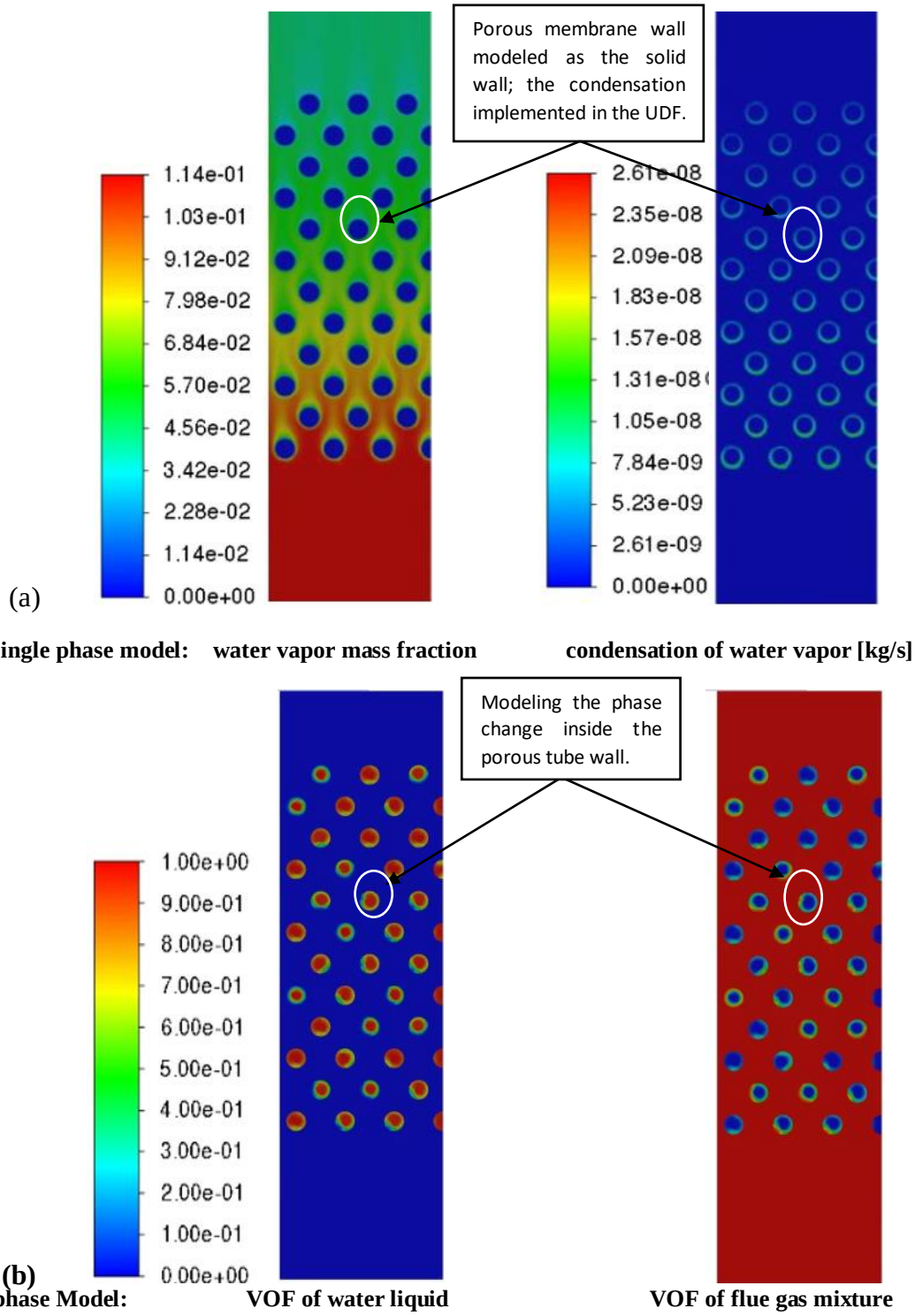

Figure 54. Visualization of the Differences Between the Single-Phase Model and the Multiphase Model.

6.6. Parametric Study using Multiphase flow

Effect of flue gas Reynolds number : Using the proposed multiphase model coupled with the Lee model and the transport model based on Darcy law, the effect of flue gas Reynolds number and inlet water temperature on the condensation rate and condensation% at different inlet water temperatures were studied numerically. The results are shown in Figure 55 and Figure 56. As seen, increasing the Reynolds number reduces the condensation rate and the condensation%. This is related to the reduction in the flow residence time inside the domain as the flow velocity increases. While the outlet flue gas temperature increases linearly because of the increase in the latent heat released during the condensation of water vapor. The Figures also show that an increase in the inlet water temperature reduces the condensation rate and increases the outlet flue gas temperature.

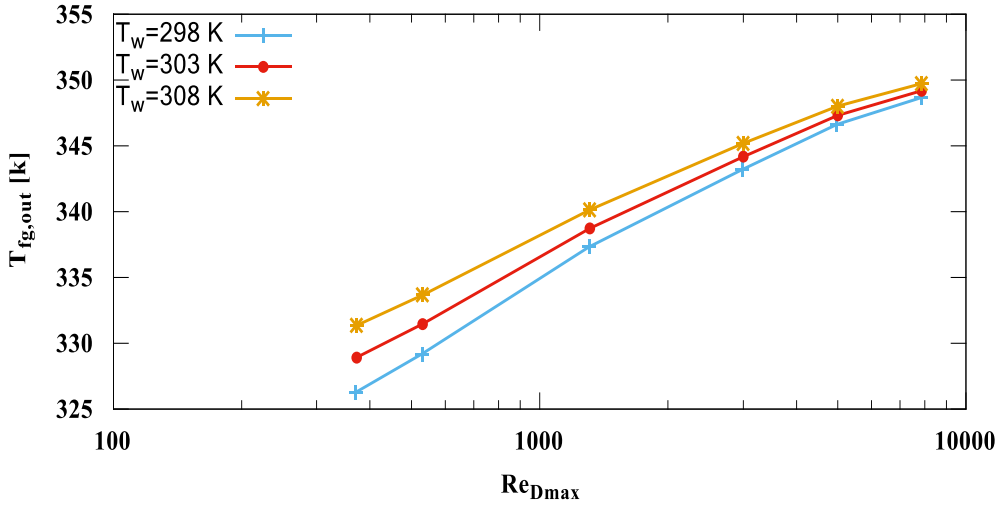

Figure 55: Effect of Flue Gas Reynolds Number on the Flue Gas Outlet Temperature for Different Inlet Water Temperatures, at Inlet Boundary Conditions: $\dot{m}_{fg}$ = 0.526 m/s, $\dot{m}_w$=0.05 m/s, and T_{fg}=355 K.

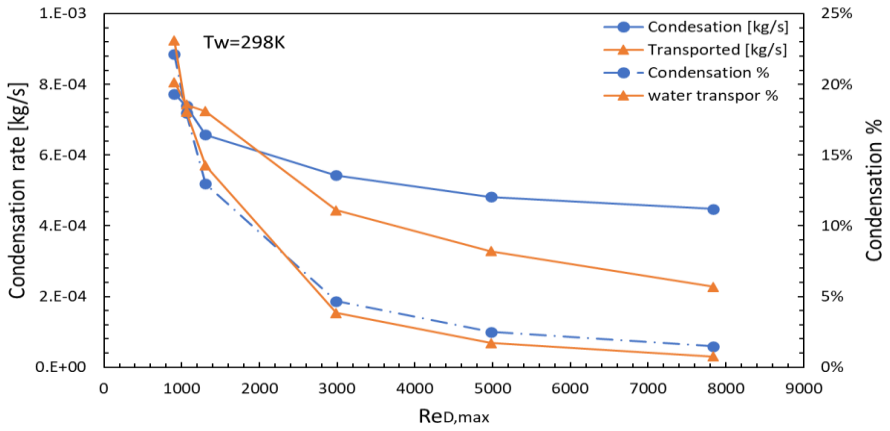

a)

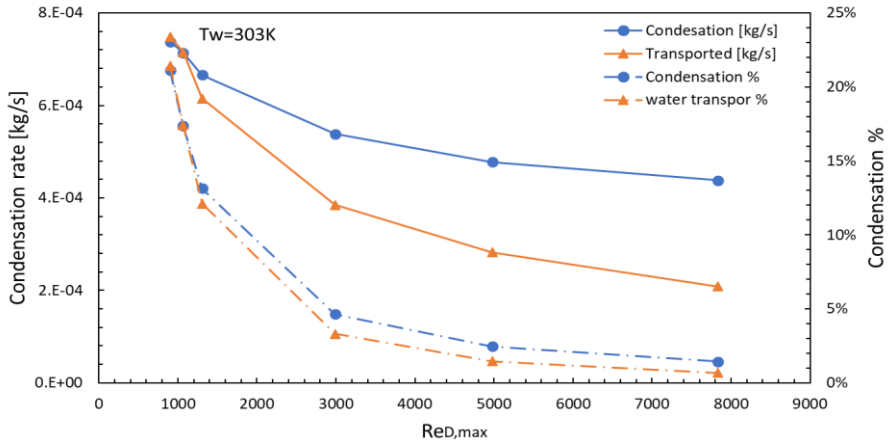

b)

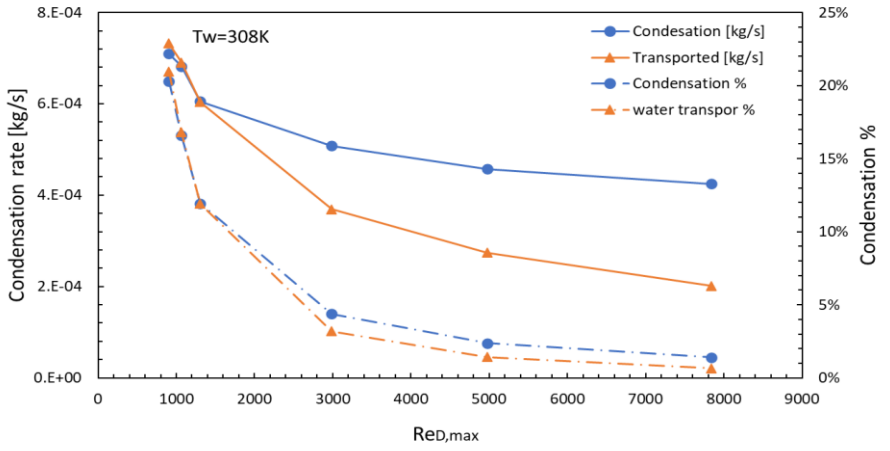

c)

Figure 56. Effect of Cooling Water and Flue Gas Reynolds Number on the Condensation and Transported Water (a) Tw= 298 K, (b) Tw=303 K, and (c) Tw= 308 K, with inlet

boundary conditions: V_{fg}= 0.526 m/s, $\dot{m}_w$=0.05 m/s, and T_{fg}=355 K, and water vapor mass farction=14%.

Effect of water-vapor mass fraction: The effect of the water-vapor mass fraction entering the domain with flue gas is represented in Figure 57. It can be noticed that an increase in the water vapor mass fraction increases the condensation rate significantly as expected but reduced the condensation% slightly. This is related to the significant increase in the water vapor discharge inside the domain compared to the system's ability to condensate more water vapor and transported through the membrane under the flue gas condition, as a significant amount of heat was added because of the released latent heat as a result of the condensation. It should also be noticed that the transport rate increased to a certain amount and then moved to a slight unnoticeable increase with an increase in the water vapor mass fraction. This can be related to the limited capacity of the membrane pores under the same operating conditions.

The current parametric study using the multiphase model revealed that the condensation percentage of water vapor out of all water vapor of the flue gas were less than 25% for different range of water vapor and inlet water temperature and less than 50% for the given of inlet water vapor mass fraction and under the defined boundary conditions. These results also confirm that part of the condensate stays inside the flue gas and might drain with flue gas in the form of condensed water or stay at the outer surface of the membrane tube. Therefore, designing the TMC at the optimum conditions to avoid large accumulation of condensate water outside the membrane should be considered in this matter. The accumulation of condensate water outside the membrane could mix with the other species of particulate of the flue gas. The existence of condensation with fine particles blocks the pores of the porous

membrane and causes membrane fouling, which reduces the porous membrane performance. However, this study is limited to the CO_2, N_2, H_2O and O_2 species. Study the effect of the existence of the water condensate inside the flue gas domain simultaneously with a harmful flue gas species such as NO_x and SO_2 and ashes on the TMC performance need further investigation and it should be considered for a future work.

(a)

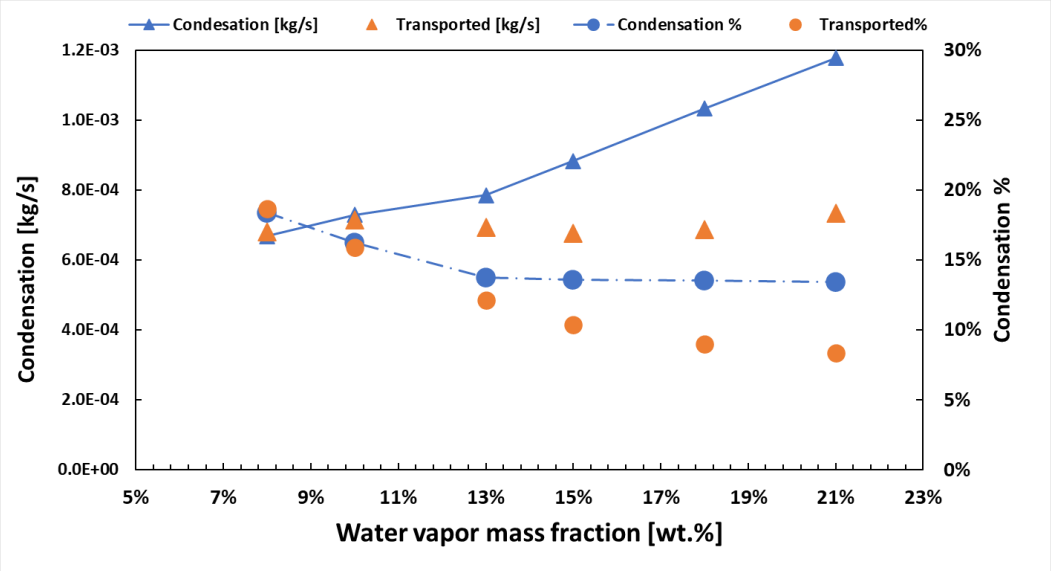

(b)

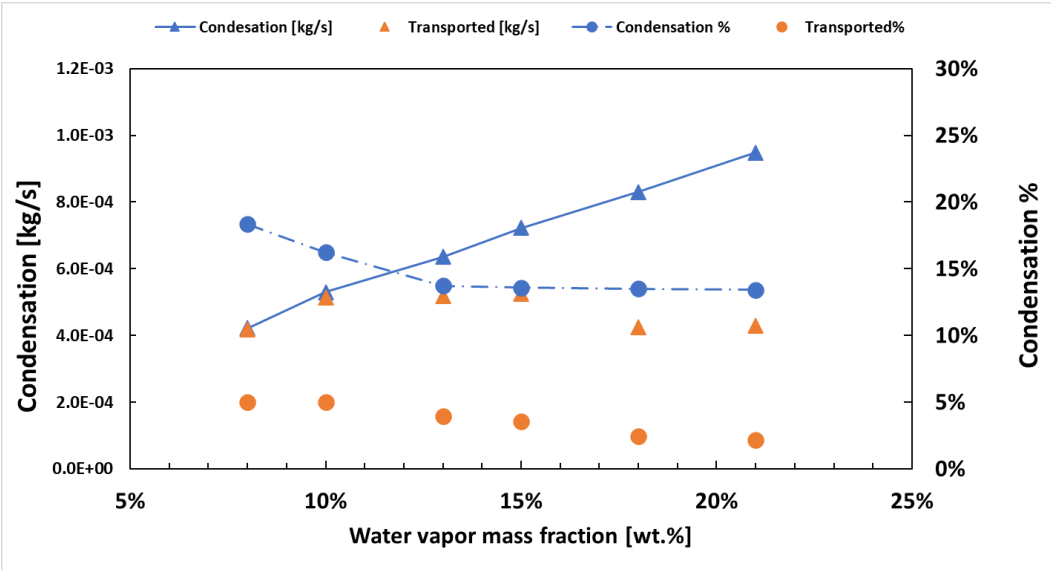

Figure 57. Effect Water Vapor Mass Fraction on the Condensation Rate, Transported Water, Transported % and Condensation% Calculated Using the Lee Model under the inlet

boundary conditions (a) $V_{fg,in}$=2.47 m/s, and (b) $V_{fg,in}$=5.64 m/s. For V_w=0.05 m/s, T_{fg}=355 K, and T_w=298 K.

6.7. Flow Patterns for Condensed Water Vapor in a TMC Single Tube

The analysis of the heat and mass transfer of a staggered ceramic membrane tube bundle is reduced to a single ceramic tube to reduce the computational time and facilitate representation of condensation in the porous membrane tube The single tube dimension was adopted from [55].

The flow pattern in the nanoporous ceramic membrane has not been studied before. The condensate of water vapor at the outer surface of the ceramic membrane and inside of the porous material are function of time as well as the flow conditions. For accurate understanding and predictions of heat and mass transfer for condensation inside the TMC, the flow pattern has been monitored at different operating conditions. Figure 58 and Figure 59 represent the flow pattern for different cooling water flow rate and air flow rate, respectively. The water VOF inside the nanoporous ceramic membrane was captured at a specific time step during the transient simulation. In the first five seconds of the simulation, the water liquid start accumulates fast in the nanoporous membrane, after that the process getting slower due to the increase in the membrane temperature, decrease in the temperature difference between the two-working fluid, and the limited capacity of the membrane tube. As the flow move from the inlet to the outlet, the heat transfer continues, and the fluid temperature decreases gradually resulting in condensate more water vapor. However, the process of water vapor condensation decreases with cooling water flow direction, where the most part of condensation take place at the first half part of the

membrane tube this is related to the highly content of water vapor in the flue and the temperature difference across the membrane tube which reduces as the flow moves from inlet to outlet.

It should be noted that, in some cases, the software builds condensation faster than the other cases, and this is related to the variation in the BC's also variation in the time step with respect to the conversion criteria. The above analysis of the heat and mass transfer and flow field, combined with the distribution characteristics of the flow and liquid phase VOF, shows that the temperature difference is higher at the first half of the membrane tube from the direction of cooling water flow and also it's the region of high water vapor content showing that more than 60% of water transport occurs in the first half of the nanoporous membrane and first five seconds of the flow.

The above investigation of the flow field and heat and water transfer, combined with the distribution characteristics of the flow and water phase condensation in the nanoporous material is a tool that can be used to study the effect of the existence of fine particulate and other harmful species with condensate water on the membrane performance and membrane life cycle. In addition, determining the region of high condensate concentration which accompanied with flow conditions can be used to determine optimum operating conditions. As seen from the figures, the distribution of high concentration region associated with water flow and air-water vapor mixture flow rate, as both flow rates increase, the high concentration region extended through the membrane tube.

Water flow rate	Flow time = 0.5 sec	Flow time = 1 sec	Flow time = 5 sec	Flow time = 15 sec	Flow time = 20 sec	Flow time = 25 sec
Volume fraction (water-liq) [-] 						
5L/h	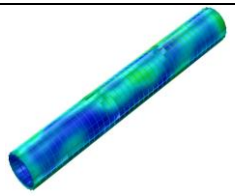	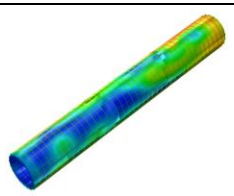	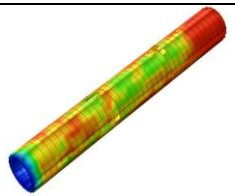	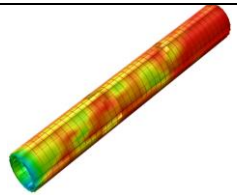	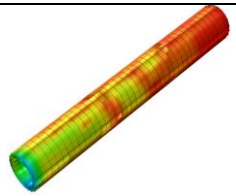	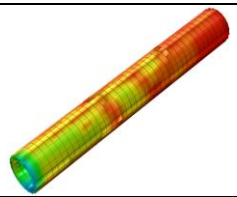
10L/h	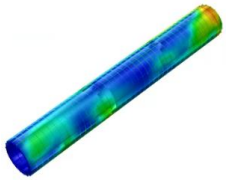	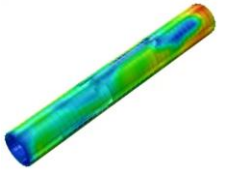	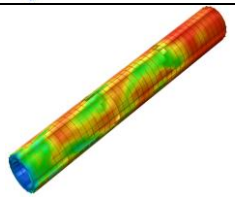	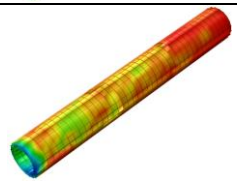	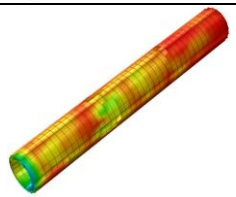	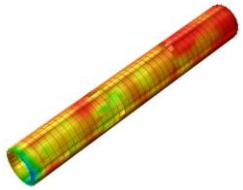
15L/h	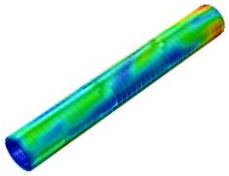	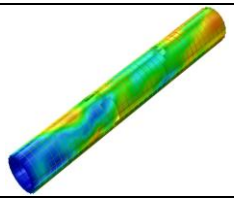	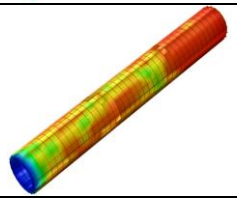	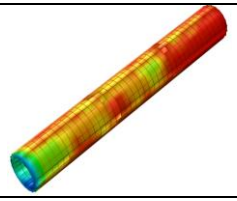	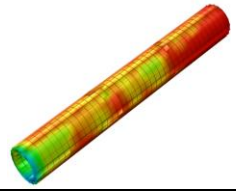	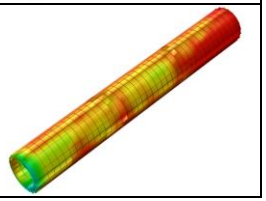

Figure 58: Multiphase Flow Pattern in the Nanoporous Ceramic Membrane under the Effect of Different Cooling Water Flow Rate at inlet water temperature 300 K, and inlet gas temperature 350 K.

Air-vapor mixture	Flow time = 0.5 sec	Flow time = 1 sec	Flow time = 5 sec	Flow time = 15 sec	Flow time = 20 sec	Flow time = 25 sec
Volume fraction (water-liq) [-] 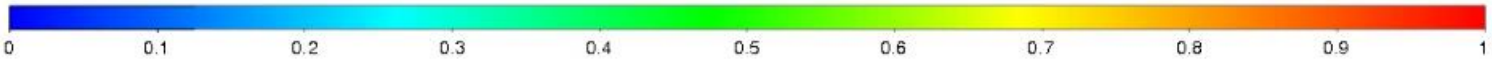						
2 L/h	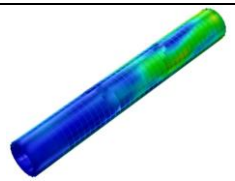	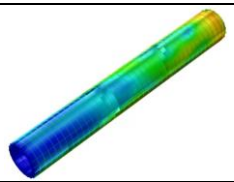	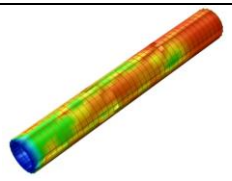	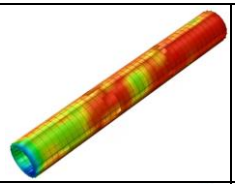	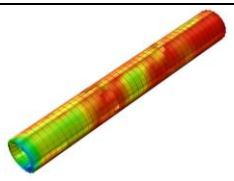	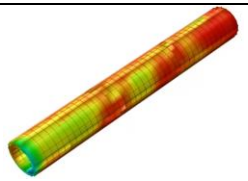
3 L/h	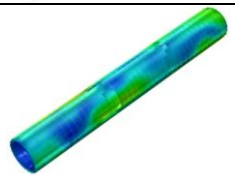	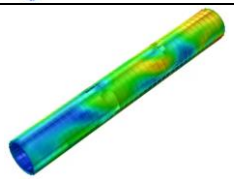	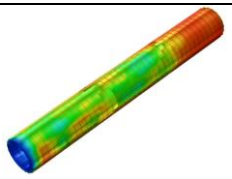	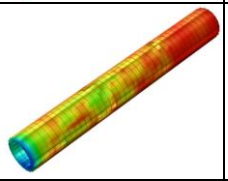	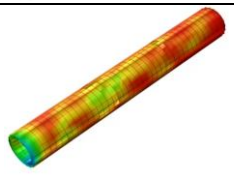	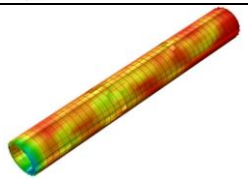
4 L/h	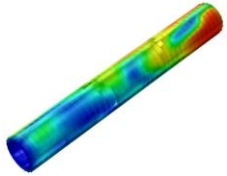	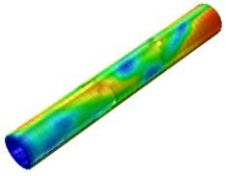	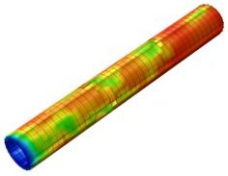	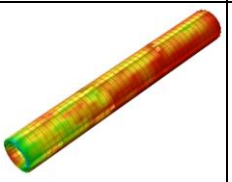	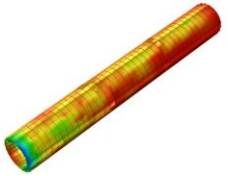	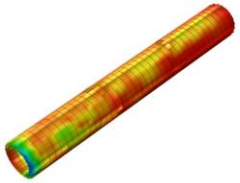

Figure 59: Multiphase Flow Pattern in the Nanoporous Ceramic Membrane Under the Effect of Different Air Flow Rate on Water and Heat Fluxes. Experimental conditions: water vapor saturated air as the gas stream; gas mixture temperature 348 K; liquid flow rate 5L/h; liquid side gauge pressure 0; gas side gauge pressure 0.04 MPa; effective membrane area 0.0021 m^2.

7. CHAPTER VII: SUMMARY AND CONCLUSION

Summary and Conclusions

The current research objectives were focused in investigating and reporting the optimum heat and mass transfer under different operating conditions, nanoporous membrane characteristics and staggered TMC geometrical parameters. A second objective was to derive empirical correlations can predict the heat and mass transfer and pressure drop from TMC staggered tube bundle, and develop a multiphase numerical model to model the phase change through TMC tube and provide a visualization of the mass transfer through the nanoporous membrane tube. Based on the current research activities, the following summary and conclusions can be drawn:

- The heat and mass transfer of transport membrane-based heat exchangers were numerically investigated. The single-phase species transport model coupled with the condensation model written in an appropriate user-defined function (UDFs) was used to run the simulation using Ansys/Fluent software. Two condensation mechanisms were examined. The results were validated against the previously published experimental data points.
- An extensive parametric study was done for the effects of the operating conditions, membrane characteristics, and geometrical parameters of the staggered TMC tube bundle. Particularly, the variation of the flue gas inlet temperature and cooling water temperature, water vapor mass fraction, membrane porosity, tube rows, flue

gas Reynolds numbers, and inner and outer membrane tube diameters on the flue gas heat transfer, condensation rate, and pressure drop were investigated.

- The results of numerical results using a validated mixed condensation model were compared with different single-phase Nusselt number and pressure drop (no condensation) correlations developed previously in the literature. New TMC correlations for convective and overall Nusselt number and friction factor were derived for the TMC tube bundle based on the examined parameters.
- Within the examined parameter ranges, the average convective Nusselt number was first evaluated based on sensible heat transfer. The results showed that an increase in the N_R for the same tube dimensions and the Reynolds number can enhance the heat transfer and therefore the Nusselt number significantly. The correlations of Zukauskas 1972 were in better agreement with the numerical results than other correlations examined. For example, a satisfactory agreement with the correlations was observed at an N_R of 6 and 12, with a maximum error of 17% and 28% at $Re_{D,max}$ = 320, respectively. The results also showed that the tube diameters of 5.49 mm and 4.57 mm have a lower heat transfer than the other two tube diameters. The optimum overall convective Nusselt was obtained at d_o= 7.62 mm.
- The effects of the row number and tube outer diameter as well as the Reynolds number on the condensation rate and water recovery efficiency were also studied numerically. As N_R and Reynolds number increases, so does the condensation rate, while the water recovery efficiency decreases. Higher water recovery efficiency was obtained at a lower Reynolds number associated with a lower mass flow rate of the flowing gas. A change in the N_R from 4 to 24 would increase the condensation

rate by 326% and 1087% and the overall Nusselt number by 917% and 1532% for Reynolds numbers at 320 and 4037, respectively.

- As the row number N_R and Reynolds number increase, the pressure drops inside the TMC tube bundle increase. The pressure drops inside the TMC tube bundle obtained numerically were also compared with the single-phase flow correlations. At a low Reynolds number, the pressure drops obtained numerically were very close to that ~~one~~ predicted from the correlations. However, as the Reynolds number increases, the TMC pressure drop diverges from the correlations.
- A significant change in the pressure drops was noticed as the tube diameter changed. Decreasing the tube diameter increases the difference between the numerical and single-phase correlation results. At d_o=7.62 mm, the pressure drop of the TMC was in good agreement with the Gunter-Shawn model, with a maximum error of about 19%. A slight divergence from the Holman-Jacob model produced a maximum error of 30%.
- New correlations for average convection Nusselt number, condensation-convection Nusselt number, and pressure drop inside the TMC tube bundles were proposed for flue gas. The effects of the tube diameter, number of rows, Reynolds number, condensation rate, and other membrane geometrical parameters were considered in the proposed correlations. The correlations for $\overline{Nu}_{conv}$, $\overline{Nu}_{cond-conv}$, and friction factor show good agreement for all investigated parameters within errors of ±10%, ±10%, and ±15%, respectively. The correlations can be used to estimate the heat transfer and pressure drop during the design of transport membrane-based heat exchangers.

- The dominant condensation mechanism in the transport membrane condenser was investigated numerically. The numerical results were in good agreement with the experimental results. The membrane porosity and the water vapor mass fraction were varied during the simulation. The results showed that the total condensation rate increases by about 18%, as the porosity increases from 0.15 to 0.50. The percentage of wall condensation decreases as porosity increases, while the percentage of capillary condensation increases. The wall condensation is able to recover more latent heat than the capillary condensation mechanism, due to the amount of condensate of water vapor by this mechanism. Also, an increase in the membrane porosity reduces the convection Nusselt number.
- Also, the results showed an increase in the wall's condensation percentage, about 69% to 87% of the total condensation rate, as a result of an increase in the flue gas water vapor mass fraction from 8% to 21%. It was found that the wall condensation mechanism is the dominant condensation mechanism within the investigated water-vapor mass fraction. Furthermore, As the water vapor mass fraction increases, the latent Nusselt number increases for the wall condensation mechanism and decreases for the capillary condensation mechanism.
- The effects of flue gas turbulence intensity on the condensation rate, convective heat transfer, and pressure drop of the TMC heat exchanger in cross-flow were numerically investigated with a validated CFD model. The results showed a significant enhancement in the TKE, condensation rate, pressure drop, and heat transfer at a given Reynolds number with an increase in turbulence intensity. The maximum increase in the condensation rate was 12.15%, at $Re_{D,max} = 5000$, for the

tube bundle with do= 4.57 mm, when the turbulence intensity increases from 5% to 25%. The maximum increase in the pressure drop was 9.91% at $Re_{D,max}$=5000, for the tube bundle with do= 5.49. The maximum increase in the Nusselt number was 15.24% at $Re_{D,max}$=10000, for tube bundle with do= 4.57.

- A multiphase modeling approach using the VOF, species transport, and Lee condensation models were proposed for modeling the heat and mass transfer inside the TMC tube bundle. The water transport through the TMC was modeled using the Darcy law approach.
- The multiphase model was in good agreement with the previously published experimental results. The error percentages were less than 1% and 5% for the outlet flue gas temperature, and less than 5% for the outlet water temperature. The multiphase model results were closer to the experimental results than the single-phase model in terms of the outlet flue gas temperature and condensation rate.
- Using the multiphase model approach under different operating conditions, the numerical results revealed that the condensation percentage of water vapor out of all water vapor of the flue gas inside the flue gas domain was between 21% and 81%, compared to the reported experimental condensation between 7% and 49%. The effect of the flue gas Reynolds number, inlet water temperature, and inlet water vapor mass fraction was studied. An increase in the Reynolds number reduces the condensation rate and the condensation percentage. Increasing the inlet water temperature reduces the condensation rate and increases the outlet flue gas temperature. Furthermore, increasing the water vapor mass fraction increases the condensation rate significantly and reduces the condensation percentage slightly.

- The flow pattern in the nanoporous ceramic membrane was observed and monitored using the proposed multiphase model. The condensate of water vapor at the outer surface of the ceramic membrane and inside of the porous material are a function of time as well as the flow conditions. More than 60% of water transport occurs in the first half of the nanoporous membrane and within the first five seconds of the flow.
- The multiphase model can be used to predict phase change and water transport in the TMC wall. That is very helpful for accurate understanding and predictions of the TMC working principles to improve its design in future development.

In conclusion, the current study was able to model the heat and mass transfer from the TMC based heat exchanger numerically. The results showed that the condensate water vapor enhances the heat transfer with a maximum increase of 23% for the given parameters. The variation of tube number of rows has a significant effect on both heat transfer and condensation rate. However, working with a laminar flue gas shows no effect for increasing the NR above 12 rows, as compared to the turbulent flow of flue gas that increase the NR to 24 rows increase both heat transfer and condensation linearly. The effect of flue gas turbulence intensity has an attractive effect on heat transfer and condensation. An increase in the turbulence intensity could lead to an enhancement in the condensation rate and Nusselt number, about 12.15% and 15.24% at ReD,max=10000, respectively. The Selection of the of TMC tube diameter is a critical to the performance of the TMC tube bundle. The optimum condensation rate was obtained for the tube bundle with do=5.49 mm, and the maximum Nusselt number for the tube bundle with do=7.62 mm.

The heat transfer and pressure drop of TMC tube bundle were compared with the existence of single-phase correlation. It was found that except for selected conditions, the single-phase correlations were noticed to differ from the TMC numerical results. Empirical TMC correlations for heat transfer and pressure drops with respect to condensation rate, number of rows, and the nanoporous membrane geometrical properties were derived thereby. The derived correlations for TMC show a good agreement with numerical data for all investigated parameters and can predict the 96% of the convective Nusselt number, overall Nusselt number, and friction factor inside the TMC within ±10%, ±10% and ±15% respectively. The effects of key parameters on the heat transfer, mass transfer, and pressure drops are illustrated and discussed in detail. The proposed correlation was defined from numerical results within a wide range of tube diameters (4.57-7.62 mm), number of rows (2-24 rows), and Reynolds number (170-8900), under flue gas condensation. The proposed correlation is able to model the heat transfer and pressure drops from TMC within the defined range of parameters, accurately.

8. FUTURE WORK

The current study has a limitation, the condensation model was built based on the assumption that the nanoporous layers are regular shape. however, The TMC tubes have a multi-layer structure, and each layer has different thickness, pore size , and surface tension, which need to more investigation in term of the TMC total performance.

The proposed TMC correlations were developed based on the Numerical study for a defined range of the design parameters. Extend the parametric study to a larger range of design parameters to test the correlation accuracy in a further range of design parameters.

The flue gas species in the current research was limited to H_2O (v), O_2, CO_2, and N_2. However, in most of the power plants, flue gas holds a significant percentage of solid particulate, ashes, and some of the harmful species, such as the SO_2 and NO_x. The effect of the existence of these species with the condensate water on the membrane tube performance life span is still not studied. The proposed multiphase model can be used to study the effect of the existence of fine particulate and other harmful species with condensate water on the membrane performance and membrane life cycle.

LIST OF REFERENCES

[1] Pellegrino, J. L., Margolis, N., Justiniano, M., Miller, M., & Thedki, A. (2004) "Energy use, loss, and opportunities analysis for US manufacturing and mining," *Energetics Inc.*, Columbia, MD (United States).

[2] Chen, H.; Zhou, Y.; Cao, S.; Li, X.; Su, X.; An, L.; Gao, D., 2017, "Heat Exchange and Water Recovery Experiments of Flue Gas with Using Nanoporous Ceramic Membranes," *Applied Thermal Engineering*, Vol. 110, pp. 686–694.

[3] Ray R. J., 1986, "Research on an Energy-Efficient Drying Process," Final Rep. (No. DOE/ID/12293-1). Bend Res. Inc., OR, USA.

[4] Song, X., Zhang, C., Li, P., Zheng, J., Hu, Y., Hou, X., & Xu, G., (2013), "Experiment and Analysis on Flue Gas Low Temperature Corrosion Monitoring," Energy and Power Engineering, Vol. 5 (4), pp. 1383-1386.

[5] Chen, Z. B., Chen, Y. H., Li, B. Y., Zeng, X. Y., Lv, Y. S., & Liu, X., (2013) "Corrosion of Tail Heated Surface Tube under Flue Gas Medium in LNG Power Station," *Applied Mechanics and Materials, Vol*. 331, pp. 74-78.

[6] Folkedahl, B. C., Weber, G. F., & Collings, M. E. (2006), "Water extraction from coal-fired power plant flue gas," *National Energy Technology Laboratory*, Final Report, DOE Cooperative Agreement No. DE-FC26-03NT41907, Pittsburgh, PA.

[7] Scott K., (1995) "Handbook of Industrial Membranes," *Elsevier*, pp. 271-305.

[8] Michels, B., Adamczyk, F., Koch, J., 2004, "Retrofit of a Flue Gas Heat Recovery System at the Mehrum Power Plant an Example of Power Plant Lifetime Evaluation in Practice," *Proceedings of the POWER-GEN Europe Conference*, pp. 10-11.

[9] Soleimanikutanaei, S., Lin, C.X., and Wang, D., 2017, "Performance Evaluation of Multi-Stage Shell and Tube Transport Membrane Condenser Heat Exchangers for Low Grade Waste Heat and Water Recovery," *ASME Heat Transfer Summer Conference*, Vol. 1, HT2016-7291, V001T01A004.

[10] Soleimanikutanaei, S., Lin, C.X., and Wang, D., 2018, "Modeling and simulation of cross-flow transport membrane condenser heat exchangers," *International Communications in Heat and Mass Transfer* Vol. 9, pp. 92–97.

[11] Soleimanikutanaei, S., Lin, C.X., and Wang, D., 2019, "Numerical Modeling and Analysis of Transport Membrane Condensers for Waste Heat and Water Recovery from Flue Gas," *International Journal of Thermal Sciences,* Vol. 136, pp. 96–106.

[12] Soleimanikutanaei, S., Lin, C.X., and Wang, D., (2016) "Modelling of Shell and Tube Transport Membrane Condenser Heat Exchangers in Low Grade Exchanger Units," *Proceeding of ASME Heat Transfer Summer Conference*, HT2016-7291, V001T01A004.

[13] Soleimanikutanaei, S., Ghasemisahebi, E., Lin, C. X., & Wang, D., (2016), "Modelling of Shell and Tube Transport Membrane Condenser Heat Exchangers in Low Grade Waste Heat and Water Recovery Applications.," *Proceeding of ASME International Mechanical Engineering Congress and Exposition*, Vol. 8, IMECE2016-67906, V008T10A011.

[14] Soleimanikutanaei, S., Ghasemisahebi, E., Lin, C.X., Wang, D., (2017) "Off-Design Modeling of Shell and Tube Transport Membrane Condenser Heat Exchangers," *ASME International Mechanical Engineering Congress and Exposition, Proceedings (IMECE)*, Vol. 8, IMECE2017-72495, V008T10A061.

[15] Huang, S. M., Yang, M., Hong, Y., & Ye, W. B., (2018) "Performance correlations of an adjacently internally cooled membrane contactor applied for liquid desiccant air dehumidification," *Applied Thermal Engineering*, Vol. 129, pp. 1660–1669.

[16] Bao, A., Wang, D., & Lin, C. X. (2015), "Nanoporous Membrane Tube Condensing Heat Transfer Enhancement Study," *International Journal of Heat and Mass Transfe*r, Vol. 84, pp. 456–462.

[17] Lin, C. X., Wang, D., & Bao, A., (2013) "Numerical modeling and simulation of condensation heat transfer of a flue gas in a bundle of transport membrane tubes," *International Journal of Heat and Mass Transfer*, Vol. 60. pp. 41–50.

[18] Aly, S., & Cunningham, J., (1979) "Effect of Mass Transfer on Flow Across a Staggered Tube Bundle." *International Journal of Heat and Fluid Flow*, Vol. 1, pp. 169-175.

[19] Zhang, C., Sousa, A. C., & Venart, J. E., (1993) "The Numerical and Experimental Study of a Power Plant Condenser," *Journal of Heat Transfer*, Vol. 115, pp. 435-445.

[20] Nazarimanesh , M., Yousefi, T. and Ashjaee, M., (2015) "Experimental Study on the Effects of Inclination Situation of the Sintered Heat Pipe on its Thermal Performance." *Experimental Thermal and Fluid Science*, Vol. 68, pp. 625-633.

[21] Alammar A. A., Al-Dadah R. K., and Mahmoud S. M., (2016), "Numerical Investigation of Effect of Fill Ratio and Inclination Angle on a Thermosiphon Heat Pipe Thermal Performance," *Applied Thermal Engineering*, Vol. 108 (5), pp. 1055–1065.

[22] Anderson Jr, J. H., and P. B. Pribis, (1979) "Compact heat Exchanger Design Progress." *Proceedings of the 6th Ocean Thermal Energy Conversion Conference: Ocean Thermal Energy for the 80's,* Washington, DC, 1979. Vol. 2. Department of Energy.

[23] Idem, S. A., Jacobi, A. M., and Goldschmidt, V. W., (1990) "Heat Transfer Characterization of a Finned-Tube Heat Exchanger (With and Without Condensation)." Journal of Heat Transfer Vol. 112, pp. 64-70.

[24] Ellis, I. I., (1983) "Review of Shell-and-Tube Heat Exchanger Fouling and Corrosion in Geothermal Power Plant Service," Report No. DE84004539. United States Department of Energy, Fossil, Geothermal, and Solar Energy Division, Oakland, California. DOE/SF/11503-2.

[25] Browne, M. W. and Bansal, P. K., (1999) "An Overview of Condensation Heat Transfer on Horizontal Tube Bundles," *Applied Thermal Engineering*, Vol. 19 (6), pp. 565–594.

[26] Alam, M. D., Hossain, S. T., Simanto, M. H. S., Mithu, M. S. U., & Islam, M. A. (2014) "Experimental and Numerical Investigation of an Air to Water Heat Exchanger," *Proceedings of the International Conference on Mechanical, Industrial and Energy Engineering*, Bangladesh, December 26-27, 2014. ICMIEE-PI-140305-5.

[27] Alam, M. D., Popoola, O.T., and Cao Y., (2019) "Mechanically Driven Oscillating Flow Cooling Loops -A Review," Frontiers in Heat and Mass Transfer (FHMT), Vol. 13. DOI: 10.5098/hmt.13.17.

[28] Wang, D., (2011) "Advanced Energy and Water Recovery Technology from Low Grade Waste Heat," Final Technical Report, Gas Technology Institute, DE-EE0003477.

[29] Wang, D., (2016) "Simultaneous Waste Heat and Water Recovery from Power Plant Flue Gases for Advanced Energy Systems," Technical Report, Gas Technology Institute, DE-FE0024092.

[30] Wang, D., Bao, A., Kunc, W.r, and Liss, W.D., (2012) "Coal Power Plant Flue Gas Waste Heat and Water Recovery," Applied Energy, Vol. 91, pp. 341–348.

[31] Dittmeyer, R. and Caro, J., (2008) "Catalytic Membrane Reactors," *In Handbook of Heterogeneous Catalysis*.

[32] Qiu, M. M. and Hwang, S. T., (1991) "Continuous Vapor-Gas Separation with a Porous Membrane Permeation System," *Journal of Membrane Science*, Vol. 59 (1), pp. 53–72.

[33] Strathmann, H., Bauer, B., and Kerres, J., 1990, "Polymer Membranes with Selective Gas and Vapor Permeation Properties," *In Makromolekulare Chemie. Macromolecular Symposiavol,* Vol. 33 (1), pp. 161–178.

[34] Randan, J. and Paterson, R., 1997, "Preliminary Studies on the Potential for Gas Separation by Mesoporous Ceramic Oxide Membranes Surface Modified by Akyl Phosphonic Acids," *Journal of Membrane Science,* Vol. 134, pp. 219–223.

[35] Grant, R. G., (1989) "Membrane Separations," *Material Manufacturing Process,* vol. 4, no. 4, pp. 483–503.

[36] Zhaohao, L. , Zhang, H. and Haiping, C., (2020) "Application of Transport Membrane Condenser for Recovering Water in a Coal-Fired Power Plant: A Pilot Study." *Journal of Cleaner Production,* Vol. 26, pp. 1-14.

[37] Huang, C., Qian, X., & Yang, R., (2018), "Thermal Conductivity of Polymers and Polymer Nanocomposites." Materiel Science and Engineering: R: Reports Vol. 132, pp. 1–22.

[38] Xiao, L., Yang, M., Zhao, S., Yuan, W. Z., & Huang, S. M., (2019) "Entropy Generation Analysis of Heat and Water Recovery from Flue Gas by Transport Membrane Condenser. *Energy*, Vol. 174, pp. 835-847.

[39] Ghaneifar, M., Raisi, A., Ali, H. M., & Talebizadehsardari, P. (2021), "Mixed Convection Heat Transfer of AL2O3 Nanofluid in a Horizontal Channel Subjected with Two Heat Sources," *Journal of Thermal Analysis and Calorimetry*, Vol. 143, pp. 2761–2774.

[40] Wang, D., (2016) "Simultaneous Waste Heat and Water Recovery from Power Plant Flue Gases for Advanced Energy Systems," Technical report, United States: N. p., 2016. Web. doi:10.2172/1347684.

[41] Zhang, F., Ge, Z., Shen, Y., Du, X., and Yang, L., (2017) "Mass Transfer Performance of Water Recovery from Flue Gas of Lignite Boiler by Composite Membrane," *International Journal of Heat and Mass Transfer,* Vol. 115, pp. 377–386.

[42] Bakeri, G., Ismail, A. F., Rahimnejad, M., & Matsuura, T., (2014) "Porous polyethersulfone hollow fiber membrane in gas–liquid contacting processes," *Chemical Engineering Research and Design*, Vol. 92, pp. 1381–1390.

[43] Brunetti, A., Macedonio, F., Barbieri, G. and Drioli, E., (2019) "Membrane Condenser as Emerging Technology for Water Recovery and Gas Pre-Treatment: Current Status and Perspectives," *BMC Chemical Engineering,* Vol. 19.

[44] Macedonio, F., Cersosimo, M., Brunetti, A., Barbieri, G., & Drioli, E. (2014), "Water Recovery from Humidified Waste Gas Streams: Quality Control Using Membrane

Condenser Technology," *Chemical Engineering and Processing: Process Intensification,* Vol. 86, pp. 196-203.

[45] Yana S., Cuia Q., Xua L., Tua T., Hea Q., (2019) "Reducing CO2 Regeneration Heat Requirement Through Waste Heat Recovery from Hot Stripping Gas Using Nanoporous Ceramic Membrane," *International Journal of Greenhouse Gas Control*, Vol. 82, pp. 269-280.

[46] Tu T., Cui Q., Liang F., Xu L., He Q., Yan S., (2019) "Water Recovery from Stripping Gas Overhead CO2 Desorber Through Air Cooling Enhanced by Transport Membrane Condensation," *Separation Purification Technology*, Vol. 215, pp. 625–633.

[47] Kim J. F., Park A., Kim S. J., Lee P., Cho Y., Park H., Nam S., Park Y., (2018) "Harnessing Clean Water from Power Plant Emissions Using Membrane Condenser Technology," ACS Sustainable Chemistry and Engineering, Vol. 6, pp. 6425–6433.

[48] Gao D., Li Z., Zhang H., Chen H., Wang L., Liu H, (2019) "The Investigation of Desulphurization and Water Recovery from flue Gas Using Ceramic Composite Membrane," *International Journal of Energy Research*, Vol. 43, pp. 1747–1759.

[49] Cheng C., Zhang H., Chen H., (2020) "Experimental study on water recovery and SO2 permeability of ceramic membranes with different pore sizes," *International Journal of Energy Research*, Vol. 44, pp. 6313–6324.

[50] Cheng C., Liang D., Zhang Y., Zhang H., Chen H., Gao D., (2021) "Pilot-Scale Study on Flue Gas Moisture Recovery in a Coal-Fired Power Plant*," Separation Purification Technology*, Vol. 254, 117254.

[51] Cheng C., Zhang H., Chen H., (2020) "Experimental Study on Water Recovery from Flue Gas Using Macroporous Ceramic Membrane," *Materials*, Vol. 13, 804.

[52] Gao D., Li Z., Zhang H., Zhang J., Chen H., Fu H., (2019) "Moisture recovery from gas-fired boiler exhaust using membrane module array," *Journal of Cleaner Production*, Vol. 231, pp. 1110-1121.

[53] Chen, H., Zhou, Y., Cao, S., Li, X., Su, X., An, L., and Gao, D., (2017) "Heat exchange and Water Recover Experiments of Flue Gas with Using Nanoporous Ceramic Membranes," *Applied Thermal Engineering*, Vol. 110, pp. 686–694.

[54] Soleimanikutanaei S., Lin C. X., Wang D., (2016) "Numerical Investigation of heat Transfer and Condensation Rate in Two-Stage Transport Membrane Condenser Heat Exchanger Units," *Proceedings of ASME Heat Transfer Summer Conference*, HT2016-7291.

[55] Wang T., Yue M, Qi H., Feron P., Zhao S., (2015) "Transport Membrane Condenser for Water and Heat Recovery from Gaseous Streams: Performance Evaluation," *Journal of Membrane Science*, Vol. 484, pp. 10–17.

[56] Zhang H., Zhang J., Liu Z., Li Z., Chen H., (2021) "Simulation Study of Using Macroporous Ceramic Membrane to Recover Waste Heat and Water from Flue Gas," *Separation and Purification Technology*, Vol. 275, 119218.

[57] Li, Z., Xue, K., Zhang, H., Chen, H., and Gao, D., (2020) "Numerical Investigation on Condensation Mode of the Transport Membrane Condenser," *International Journal of Heat and Mass Transfer*, Vol. 161, 120305.

[58] Li, Z., Zhang, H., Chen, H., Huang, J., and Fu, H., (2020) "Water Vapor Capture Using Microporous Ceramic Membrane," *Desalination*, 482, 114405.

[59] Zhang, J., Li, Z., Zhang, H., Chen, H., and Gao, D., (2020) "Numerical Study on Recovering Moisture and Heat from Flue Gas by Means of a Macroporous Ceramic Membrane Module," *Energy*, Vol. 207, 118230.

[60] Chen H., Yang, B., (2018) "Experiment and Simulation Method to Investigate the Flow Within Porous Ceramic Membrane," *Journal of the Australian Ceramic Society*, Vol. 54, pp. 575–586.

[61] Chen, H., Zhou, Y., Su, X., Cao, S., Liu, Y., Gao, D., and An, L., (2018) "Experimental Study of Water Recovery from Flue Gas Using Hollow Micro–Nano Porous Ceramic Composite Membranes," *Journal of Industrial and Engineering Chemistry*, Vol. 57, pp. 349-355.

[62] Zhao, S., Yan, S., Wang, D. K., Wei, Y., Qi, H., Wu, T., and Feron, P.H.M., (2017) "Simultaneous Heat and Water Recovery from Flue Gas by Membrane Condensation: Experimental investigation," *Applied Thermal Engineering*, Vol. 113, pp. 843–850.

[63] Zhou, Y., Chen, H., Xie, T., Wang, B., and An, L., (2017) "Effect of Mass Transfer on Heat Transfer of Microporous Ceramic Membranes for Water Recovery," *International Journal of Heat and Mass Transfer*, Vol. 112, pp. 643-648.

[64] Yue, M., Zhao, S., Feron, P. H. M., and Qi, H., (2016) "Multichannel Tubular Ceramic Membrane for Water and Heat Recovery from Waste Gas Streams," *Industrial & Engineering Chemistry Research*, Vol. 55, pp. 2615–2622.

[65] Song, C., Pan, W., Srimat, S.T., Zheng, J., Li, Y., Wang, Y.H., Xu, B.Q. and Zhu, Q.M., (2004) "Tri-reforming of Methane over Ni Catalysts for CO2 Conversion to Syngas with Desired H2/CO Ratios Using Flue Gas of Power Plants Without CO2 Separation," *Studies in Surface Science and Catalysis*, Vol. 153, pp. 315-322.

[66] Zhang, C., Sousa, A.C.M., and Venart, J.E.S., (1993) "The Numerical and Experimental Study of a Power Plant Condenser." *Journal of Heat Transfer-Transactions of the ASME*, Vol. 115, pp. 435- 445.

[67] Grimison, E.D., (1937) "Correlation and Utilization of New Data on Flow Resistance and Heat Transfer for Cross Flow of Gases Over Tube Banks," *Trans. ASME*, Vol. 59, pp. 583–594.

[68] Pierson, O.L., (1937) "Experimental Investigation of the Influence of Tube Arrangement on Convection Heat Transfer and Flow Resistance in Cross Flow of Gases Over Tube Banks," *Trans. ASME*, Vol. 59, pp. 563–572.

[69] Huge, E.C., (1937) "Experimental Investigation of Effects of Equipment Size on Convection Heat Transfer and Flow Resistance in Cross Flow of Gases Over Tube Banks," *Trans. ASME*, Vol. 59, pp. 573–581.

[70] Hausen, H., (1983) "Heat Transfer in Counterflow, Parallel Flow and Cross Flow," *McGraw-Hill Book Company*, New York, , xx+ 515, 23 x 16 cm, illustrated, pounds sterling 45. 25.

[71] Zukauskas, A ., (1972) "Heat Transfer from Tubes in Crossflow," *Advances in Heat Transfer*, Vol. 8, pp. 93-160.

[72] Zukauskas, A., (1978) "Convective Heat Transfer in Cross Flow, in: S. Kakac, R.K. Shah, W.Aung (Eds.), *Handbook of Single-Phase Convective Heat Transfer*, Chap. 6, John Wiley & Sons, New York.

[73] Zukauskas, A., Ulinskas, R., (1988) "Heat Transfer in Tube Banks in Crossflow," *Hemisphere Publishing*, New York, 1, pp. 63–93.

[74] Wilson, A. S., Bassioun,y M. K., (2000) "Modeling of Heat Transfer for Flow Across Tube Banks," *Chemical Engineering and Processing: Process Intensification*, Vol. 39, pp. 1–14.

[75] Jakob, M., (1938) "Transfer and Flow Resistance in Cross Flow of Gases Over Tube Banks," *Trans ASME*, Vol. 60, pp. 384–386.

[76] Gunter, A. Y., W. A. Shaw, (1945) "A General Correlation of Friction Factors for Various Types of surfaces in Crossflow," *Trans ASME*, Vol. 67, pp. 643-660.

[77] Boucher, D. F., Lapple, C. E., (1984) "Pressure Drop Across Tube Banks: Critical Comparison of Available Data and of Proposed Methods of Correlation," *Chemical Engineering Progress*, Vol. 44, pp. 117-134.

[78] Tahir M. T., Jing D., Hatami M., Elahi H., (2019) "Trends in Complex Multiphase Flow Modeling for Effective Fuel Energy Acquisition," *Proceedings of 4th World Congress on Momentum, Heat and Mass Transfer*, ICMFHT 119.

[79] Wang Y., Brannock M., Cox S., Leslie G., (2010) "CFD simulations of membrane filtration zone in a submerged hollow fiber membrane bioreactor using a porous media approach," *Journal of Membrane Science*, Vol. 363, pp. 57-66.

[80] Brannock M., Wang Y., Leslie G., (2010) "Mixing characterization of full-scale membrane bioreactors: CFD modelling with experimental validation" *Water Research,* Vol. 44. pp. 3181–319.

[81] Piller M., Casagrande D., Schena G., Santini M., (2013) "Pore-scale simulation of laminar flow through porous media," *Proceeding of Heat Transfer Conference*, Conf. Ser. 501 012010.

[82] Yazgan-Birgi, P., Arafat, H. A., & Ali, M. I. H., (2019), "Implementation of two multiphase flow methods in modeling wetting of microporous hydrophobic membranes," *Science of The Total Environment*, Vol. 691, pp. 1251-1261.

[83] Porto, T. R., Barbosa de Lima, A. G., & de Amorim Júnior, W. F., (2019), "Multiphase Fluid Flow in Porous-Fibrous Media: Fundamentals, Mathematical Modeling and Applications on Polymeric Composites Manufacturing," *Diffusion Foundations,* Vol. 20, pp. 55-77.

[84] Chen, L., Chu, H. W., & Fan, X. (2015), "A Convection–Diffusion Porous Media Model for Moisture Transport in Polymer Composites: Model Development and Validation," Journal of Polymer Science, *Part B: Polymer Physics,* Vol. 53, pp. 1440–1449.

[85] Ni, H., Datta, A. K., & Torrance, K. E., (1999), "Moisture Transport in Intensive Microwave Heating of Biomaterials a Multiphase Porous Media Model," *International Journal of Heat and Mass Transfer*, 42, pp. 1501-1512.

[86] Scardovelli, R., Zaleski, S., (1999) "Direct numerical simulation of free-surface and interfacial flow, *Annual Review of Fluid Mechanics,* Vol. 31, pp. 567–603.

[87] Yabe, T., Xiao, F., Utsumi, T., (2001) "The constrained interpolation profile (cip) method for multi-phase analysis," *Journal of Computational Physics,* Vol. 169, pp. 556–593.

[88] Sethian, J.A., (2001), "Evolution, implement, and application of level set and fast marching methods for advancing fronts," *Journal of Computational Physics,* Vol. 169, pp. 503–555.

[89] Jacqmin, D., (1999) "Calculation of two-phase Navier–Stokes flows using phase-field modeling," *Journal of Computational Physics,* Vol. 155, pp. 96–127.

[90] Fadhl, B., Wrobel, L. C., & Jouhara, H. (2013), "Numerical Modelling of the Temperature Distribution in a Two-Phase Closed Thermosyphon," *Applied Thermal Engineering,* Vol. 60, pp. 122-131.

[91] Sun, D., Xu, J., and Chen, Q., (2014), "Modeling of The Evaporation and Condensation Phase-Change Problems with Fluent," *Numerical Heat Transfer, Part B, Fundamentals,* Vol. 66, pp. 326–342.

[92] Yang, Z., Peng, X. F., & Ye, P., (2008), "Numerical and experimental investigation of two phase flow during boiling in a coiled tube," *International Journal of Heat and Mass Transfer, Vol.* 51, pp. 1003–1016.

[93] El Mghari, H., El Amraoui, R., Grimech, H., Ihsane, Z., & Mouqallid, M., (2018), "Annular Condensation CFD Models for the Water-Steam in the Heat Pipe Systems," *Journal of Material and Environmental Science,* Vol. 8, pp. 763-771.

[94] Guerrero, E., Muñoz, F., & Ratkovich, N., (2017), "Comparison between Eulerian and VOF Models for Two-Phase Flow Assessment in Vertical Pipes," *CT&F - Ciencia, Tecnología y Futuro,* Vol. 7, pp. 73 – 84.

[95] Sandra C.K. De Schepper, Geraldine J. Heynderickx, Guy B. Marin, (2009) "Modeling the evaporation of a hydrocarbon feedstock in the convection section of a steam cracker," *Computers and Chemical Engineering,* Vol. 33, pp.122–132.

[96] ANSYS Fluent 2019, R1, ANSYS Inc.

[97] Imumbhon, J. O., Alam, M. D., & Cao, Y. (2021), "Design and structural analyses of a reciprocating S1223 high-lift wing for an RA-driven VTOL UAV," *Aerospace,* Vol. 8, 214.

[98] Alam, M. D., & Cao, Y. (2021), "Static and modal analysis of a crankshaft reciprocating driver for reciprocating-airfoil (RA) driven VTOL aircraft," *Mechanics Based Design of Structures and Machines,* pp. 1-16. DOI: 10.1080/15397734.2021.1991807.

[99] Moukalled, F., Mangani, L., and Darwish, M., 2016, "The Finite Volume Method in Computational Fluid Dynamics," *An Advanced Introduction with OpenFOAM and Matlab,* Springer, Berlin, Germany.

[100] Kader, B. A., (1981) "Temperature and Concentration Profiles in Fully Turbulent Boundary Layers," *International Journal of Heat and Mass Transfer*, Vol. 24 (9), pp. 1541–1544.

[101] Menter, F. R. (2011) "Turbulence modeling for engineering flows," *Ansys, Inc*.

[102] Menter, F. R. (1993), "Zonal two equation kw turbulence models for aerodynamic flows," *In 23rd fluid dynamics, plasmadynamics, and lasers conference*, pp. 2906.

[103] Menter, F. R., (1994) "Two-Equation Eddy-Viscosity Turbulence Models for Engineering Applications," *AIAA J*, Vol. 32, pp. 1598-1605.

[104] A Dehbi, A., Janasz, F., & Bell, B., (2013) "Prediction of Steam Condensation in the Presence of Noncondensable Gases Using a CFD-Based Approach," *Nuclear Engineering and Design*, Vol. 258, pp. 199– 210.

[105] Bird, R. B., Stewart, W. E., and Lightfoot E. N., (2002) "Transport Phenomena," *John Wiley & Sons, Inc*., New York, 2002.

[106] Uchytil P., Petrickovic, R., and Seidel-Morgenstern, A., (2005) "Study of Capillary Condensation of Butane in a Vycor Glass Membrane," *Journal of Membrane Science*, Vol. 264, pp. 27–36.

[107] Choi, J. G., Do, D. D., & Do, H. D., (2001) "Surface Diffusion of Adsorbed Molecules in Porous Media: Monolayer, Multilayer, and Capillary Condensation Regimes," *Industrial & Engineering Chemistry Research*, Vol. 40, (19), pp. 4005–4031.

[108] Ramezanpour, A., Shirvani, H., Rahmani, R., & Mirzaee, I. (2006), "Numerical Study of Staggered Tube Bundle in Turbulent Cross Flow for an Optimum Arrangement," *International Journal of Heat Exchanger*, Vol. 7, pp. 37-56.

[109] "NIST webbook," [Online]. Available: http://webbook.nist.gov/chemistry/.

[110] Ansys, Inc., theory guide [Online] Available: http://www.ansys.com/.

[111] Russo, F., & Basse, N. T., (2016) "Scaling of Turbulence Intensity for Low-Speed Flow in Smooth Pipes" *Flow measurement and Instrumentation*, Vol. 52, pp. 101-114.

[112] Lee, W. H. (1980), "A Pressure Iteration Scheme for Two-Phase Flow Modeling," *In T. N. Veziroglu (Ed.), Multiphase Transport Fundamentals, Reactor safety, Applications*. Washington, DC: Hemisphere Publishing.

[113] Wu H. L., Peng X. F., Ye P., Gong Y. E., (2007) "Simulation of refrigerant flow boiling in serpentine tubes," *International Journal of Heat and Mass Transfer*, Vol. 50, PP. 1186.

[114] Halder, A., (2010) "A Framework for Multiphase Heat and Mass Transport in Porous Media with Applications to Food Processes, "PHD thesis.

[115] Vincent, O., Marguet, B., & Stroock, A. D., (2017) "Imbibition Triggered by Capillary Condensation in Nanopores," *Langmuir*, Vol. 33, pp. 1655−1661.

VITA

SAJA HANI AL-RIFAI

	Born, Sur, Oman
2002-2007	B.A., Biosystem Engineering Jordan University of Science and Technology Jordan
2012- 2015	M.S., Mechanical Engineering Jordan University of Science and Technology Jordan
2015-2018	Staff Engineer ALTEK Engineering Miami, Florida
2018 -2022	Doctoral Candidate Florida International University Miami, Florida

PUBLICATIONS AND PRESENTATIONS

Saja Al-Rifai, Cheng-Xian Lin, (2021). *Heat and Mass Transfer Correlations for Staggered Nanoporous Membrane Tubes in Flue Gas Crossflow.* Journal of Heat Transfer. Jun 2022, 144(6): 062702 (15 pages).

Saja Al-Rifai, Cheng-Xian Lin, (2022). *Steady State Multiphase Modeling of Heat and Mass Transfer Inside Transport Membrane Condenser.* Proceedings of the 7th Thermal and Fluids Engineering Conference (TFEC), Partially Online Virtual and in Las Vegas, NV Conference, TFEC-2022- 40942.

Saja Al-Rifai, Cheng-Xian Lin, (2022). *Numerical Study in the Dominant Condensation Mechanism in the Cross-Flow Transport Membrane Condenser.* Proceedings of the ASME 2022 Heat Transfer Summer Conference SHTC, SHTC 2022-81884.

Saja Al-Rifai, Cheng-Xian Lin, (2021). *Heat and Mass Transfer in Cross Flow Transport Membrane Condenser Based Heat Exchanger: A Computational Parametric Study*. Proceedings of the 5-6th Thermal and Fluids Engineering Conference, TFEC, Virtual, TFEC-2020-32231.

Saja Al-Rifai, Cheng-Xian Lin, (2021). *Influence of Flue Gas Turbulence Intensity on the heat and Mass Transfer and Pressure Drop Inside a TMC Based Heat Exchanger.* Proceedings of the Heat Transfer Summer Conference, ASME, Virtual, HT2021-62552.

Saja H. Al-Rifai, Cheng-Xian Lin, Brian T. Bohan, Marc D. Polanka, (2021). *A Numerical Sensitivity Study of Modeling Parameters in the Combustion of a SWIRLER.* Proceedings of ASME Turbo Expo 2021, Virtual, GT2021-59392.

Cheng-Xian (Charlie) Lin, Saja Al-Rifai, Marc D. Polanka, Brian T. Bohan, (2022). *Lean Blowout Limit Prediction for Combustion in a Swirler by a New Indicator-Assisted RANS Approach*. proceedings of AIAA SciTech 2022 Forum, 2022, San Diego, CA & Virtual, 3608343.

Saja H. Al-Rifai, Cheng-Xian Lin, Brian T. Bohan, Kevin J. DeMarco, Marc D. Polanka. *A Study of the Effects of Containment Walls on the Combustion of a Swirl-Stabilized Flames.* Proceedings of AIAA SciTech 2023 Forum, 2023, National Harbor, MD & Virtual.

Bourhan Tashtoush, Aiman Alshare, Saja AL-Rifai, (2015). *Hourly Dynamic Simulation of Solar Ejector Cooling System using TRNSYS for Jordanian Climate*. Energy Conversion and Management, Vol. 100, pp. 300-310.

Bourhan Tashtoush, Aiman Alshare, Saja AL-Rifai, (2015). *Performance Study of Ejector Cooling Cycle at Critical Mode Under Superheated Primary Flow.* Energy Conversion and Management, Vol. 94, pp. 288-299.

Khaled M Bataineh, Saja Alrifai, (2015). *Recent Trends in Solar Thermal Sorption Cooling System Technology*. Advances in Mechanical Engineering, Vol. 5, 1-20.